Singularities and Turbulence in Hydrodynamical Models

DIPLOMARBEIT

VON
TOBIAS GRAFKE

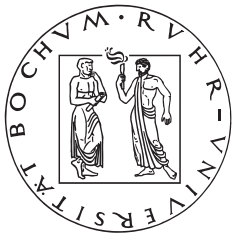

INSTITUT FÜR THEORETISCHE PHYSIK I
PLASMA-, LASER- UND ATOMPHYSIK
RUHR UNIVERSITÄT BOCHUM

BOCHUM, AUGUST 2008

Contents

Chapter 1

Introduction

When speaking of the unsolved problems in physics, dark matter comes to mind, the Higgs particle or the string theory. All these have in common that they reside in realms way outside of our everyday experience. Classical physics, especially phenomena in the scope of our own lenght-, time- and energy-scales, are widely believed to have been solved hundreds of years ago, long before relativity and quantum mechanics opened up new fertile grounds for challenging problems. Nevertheless one last stronghold of ignorance has withstood the times brave and intangible: The problem of turbulent fluid flows.

This is surprising due to several reasons. Fluids in motion naturally occur in a turbulent state under common conditions and turbulent flows are easily observable in nature itself. Their vague characteristics were always known to mankind from various scenarios, like water flow, clouds or smoke trails. The underlying model equation, the **Navier-Stokes equation**, was proposed more than 200 years ago. Due to its relevance in physics and mathematics, but also because of its significance for engineering, the problem has gained wide attention in several communities at once. Still all attempts to get a firm grip on the issue were in vain. The central question that evades all answers is quite simple: Is there a theoretical model, derived from the hydrodynamical model itself, to describe the statistics and internal structures of a turbulent flow? Is it possible to characterize the inherent laws and interactions of turbulence within a well-defined theory? The Navier-Stokes equation poses the real challenge here, but theoreticians soon discovered **Burgers' equation** as a promising playground, even if it is not as complex in comparison. By avoiding some of the main difficulties, interesting conclusions have been drawn that, even if not directly connected to the main problem, shed light on some of its aspects.

Closely related to the problem of turbulence is a more mathematical challenge: The proof of existence, uniqueness and regularity of solutions to the hydrodynamical model in question. For the Navier-Stokes equation this proof is recognized by the Clay Mathematics Institute as one of the Millennium Problems. It may seem that this answer is merely of theoretical interest, but its impact is wider than perceived at first glance. Existence for just a finite time would imply the evolution of finite time singularities, which would have a major influence on the development of turbulence. With the loss of uniqueness the equation could not be considered an adequate predictive model. The proofs of existence

and uniqueness, therefore, are at least as fundamental as the problem of turbulence.

Since both questions posed above are by far too complex to be adequately addressed here, I chose a different question as a new perspective: Is it possible to formulate a new hydrodynamical model that, while being mathematically simple enough for existence and uniqueness to be proven easily, still features manifold and diverse dynamics to stand up against the complexity of turbulent Navier-Stokes flows? And indeed such a model seems to have been found. As will be shown in the context of this thesis, the newfound model, placed somewhere between the Burgers' and the Navier-Stokes equation, is well-behaved concerning its mathematical properties. The turbulent flows evolving in this model are yet directly connected to Navier-Stokes turbulence, since the same theories and statistical predictions are successfully applied.

1.1 Goals and outline of this thesis

To introduce the new equation in chapter 2, I will begin with some general statements on hydrodynamical models, concerning basic preliminaries that all presented equations have in common. I will then briefly introduce the Navier-Stokes and Burgers' equation, covering general characteristics, conserved quantities and typical structures of the flow. In the course of this chapter, the new model equation will be motivated as natural interlink between the Burgers' and the Navier-Stokes equation and its general characteristics are examined in direct comparison.

In chapter 3, existence, uniqueness and regularity of the new equation are discussed. A brief introduction into function spaces and interpolation inequalities will be given, as preparation for the mathematical proof of the existence of solutions for all times. Using standard methods, regularity can be deduced fairly easily and with that the uniqueness of the solutions will be proved. At that point, the new model is shown to fulfill the assumption of mathematical simplicity.

Since the analysis of turbulence and singularities will mainly be carried out using numerical simulations, chapter 4 will deal with the numerical implementation of the given hydrodynamical models. Two different formulations will be presented, one to fulfil the special requirements posed by the need to simulate turbulent flows, the other to analyze singularities for the Navier-Stokes equation. As a central aspect of both formulations, the implemented Poisson solver is used (see Appendix B).

The results of the numerical simulations will be presented in the following two chapters. Chapter 5 deals with the direct comparison of all three hydrodynamical models regarding turbulent flows. First, the theoretical background on turbulence is given and generalized to fit the requirements of the newly introduced model. After this, the predictions by the theory are tested against the simulation data. It is shown that the new model equation features "true" turbulence and can be analyzed using the same statistical tools and theories.

In chapter 6 I will finally discuss possible finite time singularities for the Navier-Stokes/Euler equation. An overview will be given for the mathematical conclusions achieved so far, the criteria for a finite time blow-up known today, as well as a brief

summary of the numerical simulations conducted in the past up until now. In conclusion, the results obtained from a numerical simulation of colliding vortex tubes will be presented, without a definite result concerning a finite time singularity, but highlighting the need for higher grid resolutions.

In the last chapter, all results will be briefly summarized and evaluated.

Chapter 2

Model equations

When describing nature in terms of mathematical expressions, it is indispensable to first discuss the premises and applicability of the considered models.

Fluid dynamics, as defined in Bachelor [1974], deals with the characteristics of both liquids and gases in motion. The term **hydrodynamics** sometimes only refers to the motion of liquids, excluding the description of gases. As in theory the difference just lies in the numerical values of the fluid density ρ, I will not make this distinction and use the terms fluid- and hydrodynamics interchangeably.

Hydrodynamical models in general attempt to describe the motion of fluids in space and time. While from an experimental point of view models should describe observations and obey or predict the results of experiments, the theoretical claims to a hydrodynamical model are more subtle: Models that have no counterpart in reality can, as usual, still give insight into processes on an abstract level. Exactly this is tried in this thesis with the introduction of a new model equation, which avoids certain difficulties posed by the **Navier-Stokes equation**, the supposedly correct equation for describing fluids in motion.

In this chapter, three model equations will be discussed and compared. Section 2.1 defines general assumptions and aims that all model equations have in common. The following sections 2.2 - 2.4 each are dedicated to a specific model equation, namely the **Navier-Stokes equation**, the **Burgers' equation** and a third model, the **Euler-Burgers' equation**, which lies in a sense in between the first two. As this is just an introductory chapter to present the different hydrodynamical models, all three models are later reviewed and compared under the aspects of the existence of solutions (chapter 3), turbulence (chapter 5) and singularities (chapter 6).

2.1 The common ground

Continuum hypothesis

Every fluid is composed of molecules that each have their very own velocity and momentum, react to forces and influence surrounding molecules by collisions. All these effects take place on scales below the viscous range. As long as we want to describe fluid behavior

at larger scales, there is neither need for nor use in considering every fluid particle on its own.

Physical quantities, such as the velocity $\mathbf{u}$, the mass density ρ or the pressure p are, therefore, defined as a local average over a small fluid volume. This approach is usually referred to as *continuum hypothesis*. Of course, as soon as the size of structures in the flow become small, such as in singularities, the continuum assumption no longer holds and predictions of the model may fail.

Equations of fluid dynamics

Common to all model equations is the significance of *conservation laws*. Certain physical properties, such as mass, energy and momentum, can be conserved in a sense that the overall integral of a quantity is constant in time. The conservation of quantity φ with its associated flux $\mathbf{f}$ can be expressed in a *continuity equation*:

$$\partial_t \varphi + \nabla \cdot \mathbf{f} = 0. \tag{2.1}$$

For the special case of mass density ρ and its associated flux, the momentum density $\rho\mathbf{u}$, the continuity equation yields

$$\partial_t \rho + \mathbf{u} \cdot \nabla \rho + \rho \nabla \cdot \mathbf{u} = 0 \tag{2.2}$$

or

$$\frac{D}{Dt}\rho + \rho(\nabla \cdot \mathbf{u}) = 0, \tag{2.3}$$

where $\frac{D}{Dt} = \partial_t + \mathbf{u} \cdot \nabla$ is the *convective derivative* that describes the change of a quantity along a path of motion in a fluid with velocity field $\mathbf{u}(\mathbf{x}, t)$. A fluid is called *incompressible*, if its density ρ is constant following a fluid element

$$\frac{D}{Dt}\rho = 0, \tag{2.4}$$

which results in the important fact that a flow is incompressible if and only if its velocity field $\mathbf{u}$ is solenoidal and, thus, obeys $\nabla \cdot \mathbf{u} = 0$.

The conversion of kinetic energy at small scales into heat is modeled via the *dissipative term*

$$\nu \Delta \mathbf{u} \tag{2.5}$$

consisting of the Laplace of the velocity field and a scalar factor ν, the (kinematic) *viscosity*. Fluids with large viscosity offer strong resistance against stress and structures such as shocks or vortices are damped at larger scales. Hydrodynamical models without viscosity are called *inviscid*.

Singularities and the existence of solutions

As a physical argument, classical determinism and the principle of cause and effect would lead to the conclusion that, with complete knowledge of the initial and boundary conditions, the development of the system can be exactly predicted for all times. From a

mathematical point of view, the answer to the question whether the solution to the model equations with given initial and boundary conditions exists for all times is not so obvious or even simply not true. Additionally, solutions only seem reasonable in the strict sense mentioned below if they are unique and continuously differentiable for all times.

The typical breakdown of these properties is caused by singularities in structures that evolve. The three model equations discussed in this thesis, even if they are fairly related to each other, show significant differences in the formation of singularities. For the **inviscid Burgers' equation** (Hopf equation), even if the initial conditions are sufficiently smooth, shocks of infinite slope may develop, which destroy both smoothness and uniqueness of the solution. For the incompressible **Euler equation**, the development of singularities is a highly debated topic (see e.g. Gibbon [2007] for an overview). Rapid accumulation of vorticity from certain initial conditions is observed numerically, but the question of finite time singularities in these flows is still under dispute.

While this at first may strike as a mathematical subtlety, uniqueness and smoothness are not at all without consequence for physics. A non-unique evolution would render the hydrodynamical model in question worthless as a predictive model. Thus, uniqueness is indispensable for a successful model equation. On the other hand, a hydrodynamical model allowing the formation of finite time singularities or discontinuities, which means a macroscopic change of values over infinitesimal intervals, would violate the prerequisites of the continuum hypothesis, the very foundation the model was derived from.

The question of existence, uniqueness and finite time singularities for Euler-Burgers' equation is discussed in detail in chapter 3 while for the unsettled case of Navier-Stokes/Euler equation a presentation of the current results is given in chapter 6.

2.2 Navier-Stokes equation

The history of hydrodynamical models goes back a quarter of a millennium, when Euler stated a set of partial differential equations,

$$\frac{D}{Dt}\mathbf{u} = -\nabla p, \tag{2.6}$$

$\mathbf{u}(\mathbf{x}, t)$ being a velocity vector field, $p(\mathbf{x}, t)$ the pressure, accompanied by the incompressibility condition $\nabla \cdot \mathbf{u} = 0$. These equations are today known as the **incompressible Euler equations**, since the fluid density ρ is constant and not considered here. Just modified by a dissipative term and an external force term,

$$\frac{D}{Dt}\mathbf{u} = -\nabla p + \nu\Delta\mathbf{u} + \mathbf{f}(\mathbf{x}, t) \tag{2.7a}$$

$$\nabla \cdot \mathbf{u} = 0, \tag{2.7b}$$

these equations, which are then called **Navier-Stokes equations**, supposedly describe correctly the various aspects of fluid flows under common conditions (sufficiently high density to fulfill the continuum hypothesis, velocities low in comparison to the speed of light and the fluid does not contain ionized species).

2.2.1 General characteristics and scaling properties

The equations are defined on a domain $\Omega \in \mathbb{R}^d$, where d denotes the dimension and is commonly set to $d = 3$, when not explicitly stated otherwise. For the velocity $\mathbf{u}(\mathbf{x}, t)$ and the pressure $p(\mathbf{x}, t)$, $(\mathbf{x}, t) \in \Omega \times \mathbb{R}^+$ denote position and time. The equations are supplemented by boundary conditions. I will only consider the case of periodic boundary conditions,

$$\mathbf{u}(\mathbf{x}, t) = \mathbf{u}(\mathbf{x} + L\mathbf{e}_i, t) \tag{2.8}$$

with $L > 0$, $\mathbf{e}_i$ being the canonical basis of $\mathbb{R}^d$.

The Navier-Stokes equation exhibits important scaling properties. Consider the functions $\mathbf{u}(\mathbf{x}, t)$, $p(\mathbf{x}, t)$ that solve the Navier-Stokes equations (2.7a) and (2.7b). Then for $L > 0$, $T > 0$ the functions

$$\mathbf{v}(\mathbf{y}, s) = \frac{L}{T}\mathbf{u}(\frac{\mathbf{x}}{L}, \frac{t}{T})$$
$$q(\mathbf{y}, s) = \frac{L^2}{T^2}p(\frac{\mathbf{x}}{L}, \frac{t}{T})$$

solve the equations

$$\partial_s \mathbf{v} + (\mathbf{v} \cdot \nabla_{\mathbf{y}})\,\mathbf{v} = -\nabla_{\mathbf{y}} q + \mu \Delta_{\mathbf{y}} \mathbf{v} + \mathbf{g}$$
$$\nabla_{\mathbf{y}} \cdot \mathbf{v} = 0$$

for $(\mathbf{y}, s) \in D \times \mathbb{R}^+$, $D = L\Omega \in \mathbb{R}^d$, with

$$\mathbf{g}(\mathbf{y}, s) = \frac{L}{T^2}\mathbf{f}(\frac{\mathbf{x}}{L}, \frac{t}{T})$$
$$\mu = \frac{L^2}{T}\nu.$$

Hence one can assign dimensions to the rescaled quantities: The velocity $\mathbf{v}$ has the dimension $\frac{L}{T} = U$, the pressure q has the dimension $\frac{L^2}{T^2}$, the force $\mathbf{g}$ has the dimension $\frac{L}{T^2}$ and the kinetic viscosity μ has the dimension $\frac{L^2}{T}$. In the form of equation (2.7a), the Navier-Stokes equation is dimensionless, containing the Reynolds number

$$R = \frac{1}{\nu} = \frac{L^2}{T\mu} = \frac{UL}{\mu} \tag{2.9}$$

as the only parameter of physical significance. Because of this, flows with the same Reynolds number show the same behavior, regardless of the size of the experimental setup in reality.

To get a glimpse of the characteristics of a turbulent Navier-Stokes flow, data of numerical simulations is helpful. Figure 2.1 features a volume rendering of the vorticity $|\boldsymbol{\omega}| = |\nabla \times \mathbf{u}|$, which highlights the structures that evolve from initially large-scale perturbations. Numerous so called *vortex filaments*, tiny tubular regions of increased vorticity,

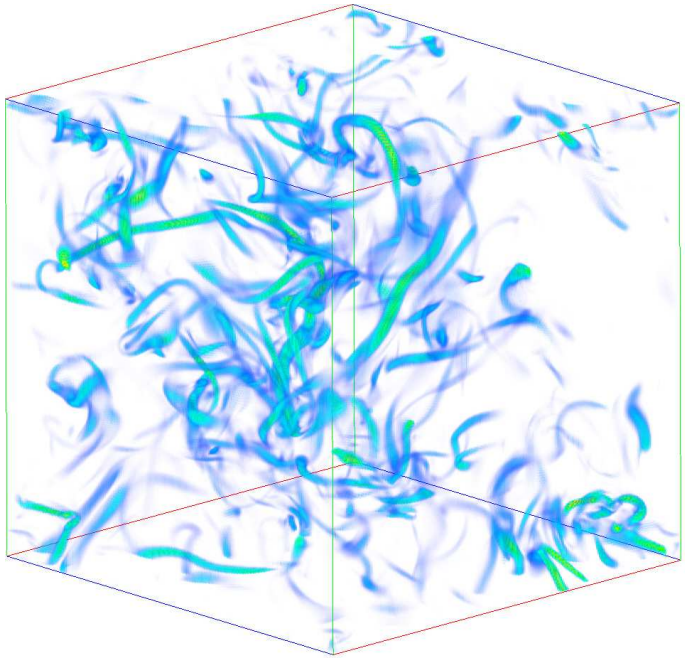

Figure 2.1: Volume rendering of the vorticity $|\boldsymbol{\omega}|$ for the Navier-Stokes equation obtained from run `NS2` (see section 5.2). The whole domain is filled with tubular *vortex filaments*.

are identified as the most dissipative structures. They are believed to govern the statistical behavior of Navier-Stokes turbulence. This just gives a first impression of the variety and complexity of the developing flows; quantitative results will be presented later in chapters 5 and 6.

2.2.2 Eliminating the pressure term

The pressure term of the Navier-Stokes equation is responsible for meeting the incompressibility condition (2.7b). As the interaction between the velocity field $\mathbf{u}(\mathbf{x}, t)$ and the pressure is instantaneous and acts on large ranges, the pressure is considered as the "bad guy" in the Navier-Stokes equation. For solving the Navier-Stokes equation, it is, therefore, advisable to avoid the pressure term to make it a closed equation for just the three components of velocity.

Projection operator

To eliminate the pressure term from the Navier-Stokes equation (2.7a), one can take a closer look at its divergence (without the force term):

$$\partial_t \nabla \cdot \mathbf{u} + \nabla \cdot ((\mathbf{u} \cdot \nabla)\mathbf{u}) = -\Delta p + \nu \Delta \nabla \cdot \mathbf{u}$$

or with the use of the incompressibility condition (2.7b):

$$\nabla \cdot ((\mathbf{u} \cdot \nabla)\mathbf{u}) = -\Delta p. \tag{2.10}$$

This Poisson equation is solvable, its solution can be formally written as

$$p = -\Delta^{-1}\big(\nabla \cdot ((\mathbf{u} \cdot \nabla)\mathbf{u})\big), \tag{2.11}$$

where Δ^{-1} denotes the inverse Laplace operator. It is noteworthy that Δ^{-1}, and thus the pressure term, is non-local in position space, while the opposite is true for the nonlinear term $(\mathbf{u} \cdot \nabla)\,\mathbf{u}$. After a transformation into Fourier space, as done in Frisch [1995], the pressure term is local, but the nonlinearity is not. This dilemma amongst others causes the problems that the Navier-Stokes equation raises both numerically and mathematically.

Inserting the just acquired solution for the pressure (2.11) back into (2.7a) one obtains

$$\partial_t \mathbf{u} + \underbrace{\big(1 - \nabla\Delta^{-1}\nabla\cdot\big)}_{\mathrm{P}}(\mathbf{u} \cdot \nabla)\,\mathbf{u} = \nu\Delta\mathbf{u} + f, \tag{2.12}$$

where the operator P is introduced. Since $\mathrm{P}^2 = \mathrm{P}$, the operator is a projection. It actually projects a vector field $\mathbf{A}$ onto its solenoidal part:

$$\begin{aligned}\nabla \cdot \mathrm{P}\mathbf{A} &= \nabla \cdot \mathbf{A} - \nabla \cdot \big(\nabla\Delta^{-1}\nabla \cdot \mathbf{A}\big)\\ &= \nabla \cdot \mathbf{A} - \Delta\,\Delta^{-1}\nabla \cdot \mathbf{A}\\ &= 0.\end{aligned}$$

This also means that due to the Hodge decomposition, every vector field $\mathbf{A}$ on Ω can be written as

$$\mathbf{A} = \mathrm{P}\mathbf{A} + \nabla\varphi, \tag{2.13}$$

where φ is an appropriate scalar field. Equation (2.12) intrinsically ensures incompressibility, as the velocity field $\mathbf{u}$, when starting solenoidal at $t = 0$, stays that way for all times. Thus, the role of keeping $\mathbf{u}$ solenoidal is transfered from the pressure term to the projection operator by solving the Poisson equation (2.10) for the pressure.

Relation (2.13) introduces another way apart from (2.12) to eliminate the pressure with the help of the projection operator P. Consider a compressible velocity field $\mathbf{u} = \mathrm{P}\mathbf{u} + \nabla\varphi$. The equation

$$\partial_t \mathbf{u} + (\mathrm{P}\mathbf{u} \cdot \nabla)\,\mathrm{P}\mathbf{u} = \nu\Delta\mathbf{u} + \mathbf{f} \tag{2.14}$$

is equivalent to the Navier-Stokes equation (2.7a), where $\mathrm{P}\mathbf{u}$ corresponds to the physical velocity field and $\partial_t\varphi - \nu\Delta\varphi$ corresponds to the physical pressure. The compressible field $\mathbf{u}$ has no counterpart in reality.

Further mathematical treatment of the projection operator P can be found in Constantin and Foias [1988] (where it is called “Leray projector”).

Vorticity formulation

The *vorticity* $\boldsymbol{\omega} = \nabla \times \mathbf{u}$ provides yet another possibility to eliminate the pressure. By taking the curl of the Navier-Stokes equation (2.7a)

$$\partial_t \boldsymbol{\omega} + \nabla \times ((\mathbf{u} \cdot \nabla)\,\mathbf{u}) = \nu \Delta \boldsymbol{\omega} \tag{2.15}$$

and using the vector identity $\nabla \mathbf{u}^2 = 2\,(\mathbf{u} \cdot \nabla)\,\mathbf{u} + 2\mathbf{u} \times (\nabla \times \mathbf{u})$ as in Frisch [1995], the resulting equation is

$$\partial_t \boldsymbol{\omega} = \nabla \times (\mathbf{u} \times \boldsymbol{\omega}) + \nu \Delta \boldsymbol{\omega}. \tag{2.16}$$

Of course, for solving equation (2.16), one needs to obtain the velocity $\mathbf{u}$ from the vorticity $\boldsymbol{\omega}$. Since

$$\begin{aligned} \nabla \times \boldsymbol{\omega} &= \nabla \times \nabla \times \mathbf{u} \\ &= \nabla \underbrace{(\nabla \cdot \mathbf{u})}_{=0} - \Delta \mathbf{u} \\ &= -\Delta \mathbf{u} \end{aligned}$$

one has to again solve the Poisson equation; the non-local operator Δ^{-1} reappears.

2.2.3 Conserved quantities and energy dissipation

In the limit of vanishing viscosity, the Navier-Stokes equation features several conserved quantities. The most important of these is the *kinetic energy*,

$$E = \frac{1}{2} \int_\Omega \mathbf{u}^2 \mathrm{d}\mathbf{x}. \tag{2.17}$$

With finite viscosity, the kinetic energy no longer stays constant but decreases via

$$\varepsilon = -\partial_t E = \nu \int_\Omega |\nabla \mathbf{u}|^2 \mathrm{d}\mathbf{x} \tag{2.18}$$

where the quantity ε is the *energy dissipation rate*. Without external forces, the energy dissipation rate obviously is a positive quantity; the kinetic energy will not grow for undriven Navier-Stokes flows. The energy dissipation rate is of central importance to the analysis of turbulent flows.

2.2.4 Global solutions and singularities

The question whether solutions to the Navier-Stokes equation exist for all times and are unique and regular has not yet been answered definitely. Since it is known that a finite-time singularity comes along with a blow-up of the vorticity (see Beale et al. [1984]) and the deformation tensor (see Ponce [1985]), current work often focuses on numerical simulations of vortex tubes and studying the behavior of the peak vorticity. Details for simulations of this kind and their history and mathematical background are discussed in the chapter about singularities (chapter 6).

2.3 Burgers' equation

Burgers' equation (first systematically studied by Burgers [1974]), being the second hydrodynamical model to be considered in this thesis, has less physical relevance to classical hydrodynamics than the Navier-Stokes equation. Though sometimes considered as equation for e.g. traffic flow, no applications are discussed here. Instead I will take Burgers' equation merely as a mathematical counterpart to Navier-Stokes, work out differences and similarities in the numerical and mathematical treatment.

The (viscid) **Burgers' equation** reads

$$\frac{D}{Dt}\mathbf{u} = \nu\Delta\mathbf{u}, \tag{2.19}$$

with $\mathbf{u}(\mathbf{x}, t)$ being a velocity vector field on a domain $\Omega \in \mathbb{R}^d$ and ν the viscosity. As obvious difference to Navier-Stokes, the Burgers' equation features neither a pressure, nor an incompressibility condition. Therefore, it is a *compressible* hydrodynamical model, allowing the formation of shocks. The absence of a global constraint, like a pressure term, makes the whole equation local in position space, which simplifies both numerical and mathematical treatment.

In the limit of vanishing viscosity, the Burgers' equation becomes

$$\frac{D}{Dt}\mathbf{u} = 0, \tag{2.20}$$

which is then called inviscid Burgers' equation or **Hopf equation**.

2.3.1 Structures and statistics

For Burgers' equation, the most dissipative structures are shocks traveling through the domain. They may arise even starting from smooth initial conditions. For vanishing viscosity, true discontinuities may build up; the strong solution is no longer continuous. For the viscous case, steeper gradients occur for smaller viscosity.

To get an impression of the characteristics of a Burgers' flow, figure 2.2 pictures an isosurface rendering of the vorticity $|\boldsymbol{\omega}|$. This allows a direct comparison to the Navier-Stokes equation, presented above. The shocks are easily observed as two-dimensional surfaces, as opposed to the one-dimensional vortex filaments of Navier-Stokes. Furthermore, the structures are larger, not as detailed and less homogeneously distributed. This fact will have an influence on the statistics of turbulent Burgers' flows, as shown in chapter 5.

2.3.2 Global solutions and singularities

Numerous results are known for the case of one-dimensional Burgers' equation. For the viscid Burgers' equation, solutions can be found by means of a *Hopf-Cole transformation* that reformulates the problem as a diffusion equation and, thus, both existence and uniqueness are easy to show. In the inviscid case, singularities arise due to the lack of dissipation. As soon as discontinuities have build up, the solution no longer exists and

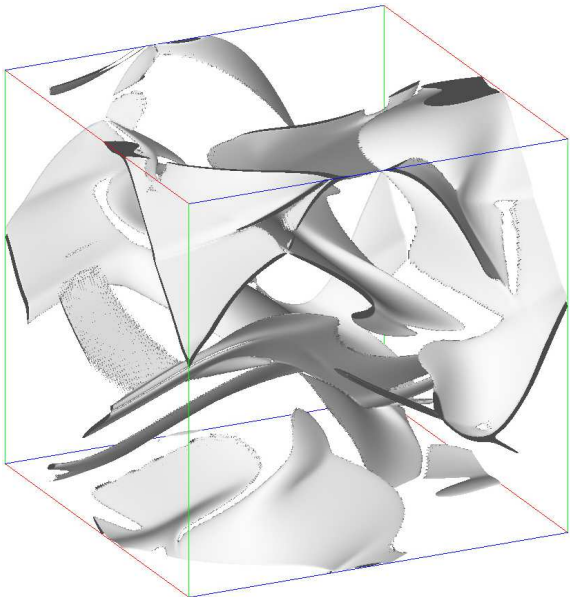

Figure 2.2: Isosurface rendering of the vorticity $|\boldsymbol{\omega}|$ for Burgers' Equation using 256^3 grid points. Two-dimensional shocks are observed as the most dissipative structures in the flow.

weak solutions are no longer unique. The physically most reasonable of the resulting weak solutions for this situation is identified as the *entropy solution* (see e.g. De Lellis et al. [2004]).

Shocks and discontinuities are observed in the three-dimensional case, too. Yet, existence and uniqueness turn out to be a more difficult matter to show and are still an open problem. Since this topic does not have much in common with the methods used in this thesis, I will not go into further detail.

2.4 Euler-Burgers' equations

To motivate the third hydrodynamical model in question, let us consider the following: For the Navier-Stokes equation, there exists neither a complete theory of turbulence, nor a proof for the existence of solutions. In contrast, Burgers' equation is much easier to handle mathematically, as all of its terms are local in position space, but is not nearly as interesting and manifold in its dynamics and in terms of turbulence. Therefore, it seems reasonable to propose a new hydrodynamical model in between those two, simpler than Navier-Stokes equation in mathematical terms, but still similar to it in most of its dynamical properties.

As a reminder, the Navier-Stokes equation, written by means of the *projection operator* P, reads

$$\partial_t \mathbf{u} + (\mathrm{P}\mathbf{u} \cdot \nabla)\, \mathrm{P}\mathbf{u} = \nu \Delta \mathbf{u} + \mathbf{f}. \tag{2.21}$$

The solenoidal part P$\mathbf{u}$ of the compressible velocity field $\mathbf{u}$ is convected by itself. For Burgers' equation, the situation looks like

$$\partial_t \mathbf{u} + (\mathbf{u} \cdot \nabla)\, \mathbf{u} = \nu \Delta \mathbf{u} + \mathbf{f}, \tag{2.22}$$

where the compressible velocity field $\mathbf{u}$ convects itself. The composition of these two equations is to consider a compressible velocity field $\mathbf{u}$ that is convected by its solenoidal part P$\mathbf{u}$:

$$\partial_t \mathbf{u} + (\mathrm{P}\mathbf{u} \cdot \nabla)\mathbf{u} = \nu \Delta \mathbf{u} + \mathbf{f}. \tag{2.23}$$

More accurately this means: The convection of the velocity field $\mathbf{u}$ is local in position space, but the projection operation is local in Fourier space. For the lack of a better name this equation will be called (viscid, driven) **Euler-Burgers' equation** to point out the close relation to both Navier-Stokes/Euler and Burgers' equation. In the following, some properties of this new set of equations are deduced.

2.4.1 General characteristics and structure of the flow

It was the aim to keep the Euler-Burgers' equation as close to Navier-Stokes as possible. The first item to study is the evolution of the kinetic energy $E(t) = \frac{1}{2}\int_\Omega \mathbf{u}^2 \mathrm{d}\mathbf{x}$ in time. For any viscid hydrodynamical model, when no external force is applied, $\mathbf{f} = 0$, the kinetic energy should slowly decay. To figure out whether Euler-Burgers' equation is a feasible model in this manner, consider the i$^{\text{th}}$ component of equation (2.23),

$$\underbrace{\partial_t u_i}_{\text{(i)}} + \underbrace{\mathrm{P}u_j \partial_j u_i}_{\text{(ii)}} = \underbrace{\nu \partial_j \partial_j u_i}_{\text{(iii)}} \qquad\qquad | \cdot u_i \int_\Omega \tag{2.24}$$

scalar multiply it by u_i under summation convention over the i$^{\text{th}}$ component and integrate over the domain Ω. For the different terms one obtains:

(i) The time derivative provides the evolution of the kinetic energy:

$$\begin{aligned}\int_\Omega u_i \partial_t u_i \,\mathrm{d}\mathbf{x} &= \frac{1}{2}\int_\Omega \partial_t u_i^2 \mathrm{d}\mathbf{x} \\ &= \frac{1}{2}\int_\Omega \partial_t u^2 \mathrm{d}\mathbf{x} = \partial_t E(t).\end{aligned}$$

(ii) The nonlinearity vanishes,

$$\begin{aligned}\int_\Omega u_i \mathrm{P}u_j \partial_j u_i \,\mathrm{d}\mathbf{x} &= \frac{1}{2}\int_\Omega \mathrm{P}u_j \partial_j u^2 \mathrm{d}\mathbf{x} \\ &= -\frac{1}{2}\int_\Omega \underbrace{\partial_j \mathrm{P}u_j}_{=0}\, u^2 \mathrm{d}\mathbf{x} \\ &= 0,\end{aligned}$$

where I make use of the periodicity of the domain Ω and the solenoidality of $\mathrm{P}\mathbf{u}$.

(iii) The dissipative term provides

$$\begin{aligned}\nu \int_\Omega u_i \partial_j \partial_j u_i \,\mathrm{d}\mathbf{x} &= -\nu \int_\Omega \partial_j u_i \partial_j u_i \,\mathrm{d}\mathbf{x} \\ &= -\nu \int_\Omega (\partial_j u_i)^2 \mathrm{d}\mathbf{x} \leq 0,\end{aligned}$$

which is always less or equal zero.

This allows to deduce

$$\varepsilon = -\partial_t E(t) = \nu \int_\Omega |\nabla \mathbf{u}|^2 \mathrm{d}\mathbf{x}, \tag{2.25}$$

which resembles the energy dissipation of the Navier-Stokes equation (2.18). The dissipative term alone is responsible for the depletion of energy. Like in Navier-Stokes equation, the nonlinearity just transports the velocity field, without damping it.

As a difference to the Navier-Stokes equation, there is no scalar field for Euler-Burgers' that resembles the pressure. When written in the same form as equation (2.21), the additional forcing term on the right hand side cannot be formulated as a gradient (in fact one obtains $\nabla p + \mathrm{P}\mathbf{u} \cdot \nabla (\nabla \varphi)$ instead of ∇p).

Regarding the structures of a turbulent Euler-Burgers' flow, one notices obvious differences. Instead of vortex filaments or shocks, the dissipative structures of the flow, indicated by the vorticity in figure 2.3 (left), seem to be two dimensional folded sheets. This is significantly different from the vortex filaments observed in a turbulent Navier-Stokes flow and has critical impact on the scaling behavior, as shown in chapter 5. Regions of compression and expansion are observable in the volume rendering of figure 2.3 (right). Quite in contrast to Burgers' equation, these objects ore not flat and only on large scales, but more detailed and evenly distributed throughout the domain. Regions of high compressibility seem to be located on the edges of the above mentioned vortex sheets.

2.4.2 Global solutions and singularities

When the Euler-Burgers' equation was motivated, mathematical simplicity was demanded. Questions regarding finite-time singularities, the existence, uniqueness and regularity of the flow, should be answerable.

As it turns out, these questions in fact can be answered for Euler-Burgers' equation. This is done in the next chapter (chapter 3), where the existence and uniqueness of the solutions are mathematically shown.

2.4.3 Turbulence

To probe the connection of the Euler-Burgers' model to the Navier-Stokes equation, turbulent flows are studied. Primary goal is to examine how "natural" a turbulent Euler-Burgers' flow behaves. Figure 2.3 gives a first impression of Euler-Burgers' turbulence,

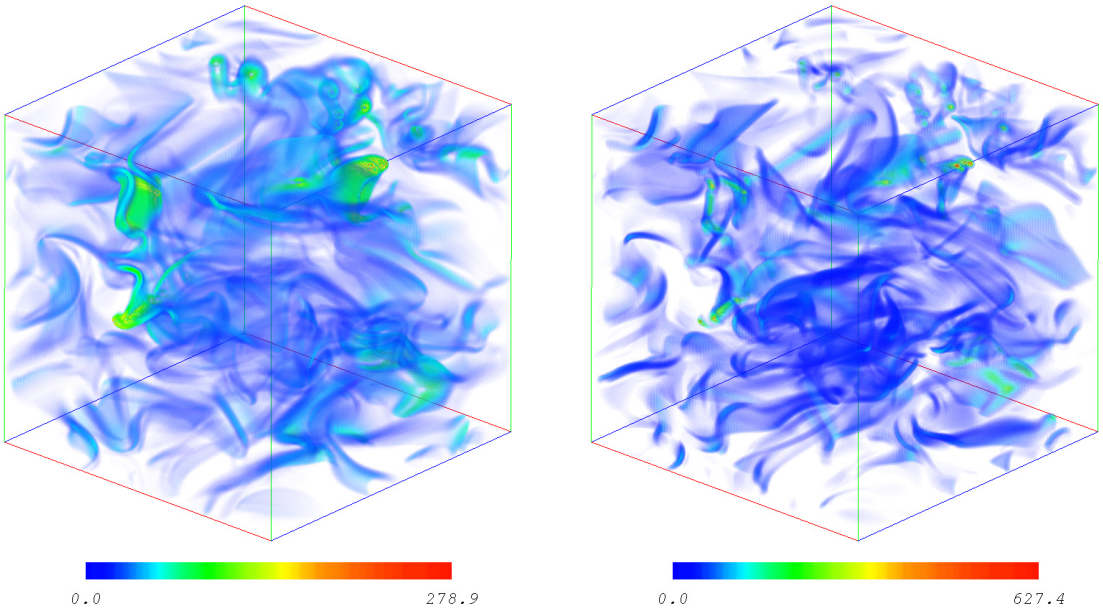

Figure 2.3: The most dissipative structures in a turbulent Euler-Burgers' flow. **Left:** Volume rendering of the vorticity $|\boldsymbol{\omega}|$. **Right:** Volume rendering of $|\nabla \cdot \mathbf{u}|$. Data taken from run `EB2` (see section 5.2 for details).

which is truly chaotic and evolves distinct dissipative structures. In chapter 5 a more quantitative approach is made to analyze the statistics and connect Euler-Burgers' turbulence to Navier-Stokes turbulence.

Chapter 3

Global solutions

The main focus of this chapter is to give mathematical proof to the existence, uniqueness and smoothness of solutions to the equation

$$\partial_t \mathbf{u} + (\mathrm{P}\mathbf{u} \cdot \nabla)\mathbf{u} = \nu \Delta \mathbf{u} + \mathbf{f}, \tag{3.1}$$

which was in the previous chapter unimaginatively called "viscid, driven Euler-Burgers' equation". As the close relation to both Burgers' and Navier-Stokes equation was pointed out, it seems interesting that this proof is relatively simple, especially if compared to the hassle that Navier-Stokes raises. The hope is to get a better feeling for the latter and to identify the terms that pose such difficulties in proving the same for Navier-Stokes equation. This proof shows that the Euler-Burgers' equation, while still being relatively similar to Navier-Stokes, has that crucial bit to it that makes the existence, uniqueness and smoothness a so much more obvious matter to show. This again provides motivation for the following chapters, where the impact of this essential difference on physical and statistical behavior in turbulence and colliding vortices is examined.

This topic is closer to mathematics than the rest of this thesis, and for this chapter I will stick to common mathematical procedure of definition, theorem and proof for the reason of clarity. As this also creates the anticipation of mathematical accuracy, I feel obliged to point out that though I try to define everything as thoroughly as reasonable, I still use the sometimes sloppy notations of physics and will not discuss every detail that would be necessary for a complete mathematically exact treatment, but point to literature instead, as soon as it gets too fussy.

3.1 Function spaces and inequalities

In the course of this chapter, a periodic domain $\Omega = [0, L]^d \in \mathbb{R}^d$ of dimension d is assumed, as this resembles the numerics and there is no need to care about special boundary conditions. For statements regarding more general domains, some regularity properties for Ω are needed, which are defined in detail in chapter II of Temam [1988] and are not presented here. For Ω we will in the following define L^p spaces and Sobolev spaces, because they contain solutions to partial differential equations even if they are no longer

continuous or continuously differentiable functions. As additional constraint, the average of the considered functions f should vanish, $\int_\Omega f \, \mathrm{d}\mathbf{x} = 0$.

Furthermore, several inequalities and embeddings are presented that are necessary for the estimates used in proving boundedness and, thus, the existence of the solution. The mathematical preliminaries in Ladyzenskaja [1964], the appendix of Doering and Gibbon [1995], or the introductory chapters of Constantin and Foias [1988] or Agmon [1965] give a more precise and complete overview of the various inequalities that are of importance.

Definition 3.1. *For $1 \leq p < \infty$, $L^p(\Omega)$ is the space of (classes of) real functions $f : \Omega \mapsto \mathbb{R}$ such that*

$$\|f\|_{L^p(\Omega)} := \left(\int_\Omega |f(\mathbf{x})|^p \, \mathrm{d}\mathbf{x} \right)^{\frac{1}{p}} < \infty$$

is finite.

$L^p(\Omega)$ is a Banach space for the norm $\|f\|_{L^p(\Omega)}$. For $p = 2$, $L^2(\Omega)$ is a Hilbert space with the scalar product

$$\langle f, g \rangle = \left(\int_\Omega f(\mathbf{x}) g(\mathbf{x}) \, \mathrm{d}\mathbf{x} \right)^{\frac{1}{2}}.$$

For convenience, the L^p-norm will be denoted as $|f|_p$ and the L^2-norm as $|f| = \langle f, f \rangle^{\frac{1}{2}}$. For functions $\mathbf{f} : \Omega \mapsto \mathbb{R}^d$ with more than one component, the above defintion may also be applied. The corresponding notation for the norm is carried over, $|\mathbf{f}|_p$ for the $L^p(\Omega)^d$-norm and $|\mathbf{f}|$ for the $L^2(\Omega)^d$-norm.

Another notation simplifies the definition of Sobolev spaces: Let $\alpha = \{\alpha_1, ..., \alpha_n\} \in \mathbb{N}^n$ be a multi-index and $[\alpha] = \alpha_1 + ... + \alpha_n$. For $f : \Omega \mapsto \mathbb{R}$ the partial derivatives in multiple directions are written as

$$D^\alpha f := \frac{\partial^{\alpha_1 + ... + \alpha_n} f}{\partial x_1^{\alpha_1} ... \partial x_n^{\alpha_n}} = D_1^{\alpha_1} ... D_n^{\alpha_n} f$$

for $D_i u = \frac{\partial u}{\partial x_i}$. With this we define:

Definition 3.2. *For $m \in \mathbb{N}$, $1 \leq p \leq \infty$, the Sobolev space $W^{m,p}(\Omega)$ is the space of functions f in $L^p(\Omega)$ (or $L^p(\Omega)^d$) whose (distribution) derivatives of order $\leq m$ are also in $L^p(\Omega)$.*

With the norm

$$\|f\|_{W^{m,p}(\Omega)} := \sum_{[\alpha]=m} |D^\alpha f|_p$$

$W^{m,p}(\Omega)$ forms a Banach space. Again, in the special case for $p = 2$, the Sobolev space $W^{m,2}(\Omega) = H^m(\Omega)$ is a Hilbert space with the scalar product

$$\langle f, g \rangle_{H^m(\Omega)} = \sum_{[\alpha]=m} \langle D^\alpha f, D^\alpha g \rangle .$$

For the often used case $m = 1$, the Hilbert space $H^1(\Omega)$ with the scalar product

$$\langle\langle f, g \rangle\rangle = \sum_{i=1}^{n} \langle D_i f, D_i g \rangle$$

and the norm $\|f\| = \left(\langle\langle f, f \rangle\rangle \right)^{\frac{1}{2}}$ fulfills the *Poincaré inequality.*

Theorem 3.1 (Poincaré inequality)**.** *There exists a constant C depending only on Ω, such that*

$$|f| \leq C(\Omega)\|f\|$$

holds for all $f \in H^1(\Omega)$.

Further relations between the different function spaces are given in the *Sobolev embedding theorem.* It implies inequalities for elements of the spaces, permitting estimates that are used later on.

Theorem 3.2 (Sobolev Embedding)**.** *Let $W^{m,p}(\Omega)$ be the Sobolev space of $\Omega \subset \mathbb{R}^d$ and $m, l, p, q \in \mathbb{N}$, $m \geq l$ and $m - \frac{d}{p} \geq l - \frac{d}{q}$ then*

$$W^{m,p}(\Omega) \subseteq W^{l,q}(\Omega)$$

The actual use of this theorem lies its application as inequality: For all $f \in W^{m,p}(\Omega)$, if $\frac{1}{p} - \frac{m}{d} = \frac{1}{q} > 0$ then $\|f\|_q \leq C\|f\|_{W^{m,p}(\Omega)}$, where C only depends on m, d, p and Ω. Inequalities of this type are called *Sobolev inequalities.* For a more detailed description of these inequalities, their exact conditions and their application to Navier-Stokes equation, see Temam [1984] and Temam [1988]. A more general inequality of this type is the *Gagliardo-Nirenberg inequality* that can be found in Doering and Gibbon [1995]:

Theorem 3.3 (Gagliardo-Nirenberg inequality)**.** *Let f be a smooth, square integrable, mean zero periodic function on Ω. Then for $1 \leq q,\ r \leq \infty$ and j and m integers satisfying $0 \leq j < m$,*

$$\|f\|_{W^{j,p}(\Omega)} \leq C\|f\|^a_{W^{m,r}(\Omega)}|f|^{1-a}_q$$

where

$$\frac{1}{p} = \frac{j}{d} + a\left(\frac{1}{r} - \frac{m}{d}\right) + \frac{1-a}{q},$$

for a in the interval

$$\frac{j}{m} \leq a < 1$$

with the exception that if $m - j - \frac{d}{r}$ is a nonnegative integer, then a is restricted to $\frac{j}{m}$.

The proof of this inequality for various domains is given in Nirenberg [1959].

3.2 Existence of global solutions

In this section, the existence of global solutions for the Euler-Burgers' equation is proven. For the three-dimensional domain $\Omega \subset \mathbb{R}^3$ finite periodic boundary conditions are assumed. P again projects $\mathbf{u}$ on its solenoidal part such that $D_i(\mathrm{P}u)_i = 0$. Initial conditions $\mathbf{u}(0, \mathbf{x}) = \mathbf{u}_0(\mathbf{x})$ and the force $\mathbf{f}$ are assumed to be as smooth as we please, since we are only interested in the results of the dynamic evolution. The aim is to show the boundedness of the solution in $H^1(\Omega)$, which implies its existence with standard arguments like e.g. Temam [1988].

3.2.1 Useful inequalities

In order to prove the existence and uniqueness of the solution, I first recall a few useful inequalities:

Lemma 3.1 (Scaled Young's inequality)**.** *Let a, b be two nonnegative real numbers, p, q positive real numbers that satisfy*

$$\frac{1}{p} + \frac{1}{q} = 1,$$

and ε a positive real number, then

$$ab \leq \frac{\varepsilon a^p}{p} + \frac{\varepsilon^{-\frac{q}{p}} a^q}{q}.$$

Lemma 3.2 (Gronwall's Lemma)**.** *Let g, h, y be three locally integrable functions on $(t_0, +\infty)$ that satisfy*

$$\frac{\mathrm{d}y}{\mathrm{d}t} \leq gy + h \qquad \text{for} \qquad t \geq t_0,$$

the function $\mathrm{d}y/\mathrm{d}t$ being also locally integrable. Then

$$y(t) \leq y(t_0) \exp\left(\int_{t_0}^{t} g(\tau)\,\mathrm{d}\tau\right) + \int_{t_0}^{t} h(s) \exp\left(-\int_{t}^{s} g(\tau)\,\mathrm{d}\tau\right) \mathrm{d}s \quad \forall \quad t \geq t_0$$

Lemma 3.3. *For $\mathbf{u} \in L^2(\Omega)^d$ and $\mathrm{P}\mathbf{u}$ being its solenoidal part, it holds that*

$$|D^\alpha \mathrm{P}\mathbf{u}| \leq |D^\alpha \mathbf{u}|$$

where $\alpha \in \mathbb{N}^n$ for $n \in \mathbb{N}$ or $D^\alpha = \mathrm{id}$.

Proof of Lemma 3.3. Let $\mathbf{u} = \mathrm{P}\mathbf{u} + \nabla\varphi$. It follows from orthogonality that

$$\langle D^\alpha \mathrm{P}\mathbf{u}, D^\alpha \nabla\varphi \rangle = 0$$

because

$$\begin{aligned}
\langle D^\alpha \mathrm{P}\mathbf{u}, D^\alpha \nabla\varphi \rangle &= \int_\Omega D^\alpha \mathrm{P}\mathbf{u} \cdot D^\alpha \nabla\varphi \,\mathrm{d}\mathbf{x} \\
&= -\int_\Omega D^\alpha \underbrace{(\nabla \cdot \mathrm{P}\mathbf{u})}_{=0} D^\alpha \varphi \,\mathrm{d}\mathbf{x} \\
&= 0.
\end{aligned}$$

This implies

$$\begin{aligned}
|D^\alpha \mathbf{u}| &= |D^\alpha \mathrm{P}\mathbf{u} + D^\alpha \nabla\varphi| \\
&= \langle D^\alpha \mathrm{P}\mathbf{u} + D^\alpha \nabla\varphi, D^\alpha \mathrm{P}\mathbf{u} + D^\alpha \nabla\varphi\rangle^{\frac{1}{2}} \\
&= (\langle D^\alpha \mathrm{P}\mathbf{u}, D^\alpha \mathrm{P}\mathbf{u}\rangle + 2\underbrace{\langle D^\alpha \mathrm{P}\mathbf{u}, D^\alpha \nabla\varphi\rangle}_{=0} + \langle D^\alpha \nabla\varphi, D^\alpha \nabla\varphi\rangle)^{\frac{1}{2}} \\
&= (\langle D^\alpha \mathrm{P}\mathbf{u}, D^\alpha \mathrm{P}\mathbf{u}\rangle + \underbrace{\langle D^\alpha \nabla\varphi, D^\alpha \nabla\varphi\rangle}_{>0})^{\frac{1}{2}} \\
&\geq \langle D^\alpha \mathrm{P}\mathbf{u}, D^\alpha \mathrm{P}\mathbf{u}\rangle^{\frac{1}{2}} = |D^\alpha \mathrm{P}\mathbf{u}|.
\end{aligned}$$

□

3.2.2 Boundedness of $|u^n|$

Let in the following be $d = 3$ and, furthermore, be u_i the i$^{\text{th}}$ component of $\mathbf{u}$, such that $\mathbf{u} = \sum u_i \mathbf{e}_i$. Let $u = \sqrt{\sum u_i^2}$ be the $\mathbb{R}^d$-norm of $\mathbf{u}$.

Theorem 3.4. *For the Euler-Burgers' equation (3.1) on the three-dimensional domain $\Omega \subset \mathbb{R}^3$ with periodic boundary conditions and finite and smooth initial conditions $\mathbf{u}(0) = \mathbf{u}_0$, there exists a constant ρ_0 depending only on Ω, n, the force $\mathbf{f}$ and on the $L^2(\Omega)$-norm of the initial conditions $|\mathbf{u}_0|$, such that*

$$|u(t)^n| < \rho_0 \tag{3.2}$$

for all $t \in (0, \infty)$, $n \in \mathbb{N}$.

Remark: This of course is equivalent to the boundedness of the $L^n(\Omega)$-norm of $u(t)$ for all times, i.e.

$$|u(t)|_n \leq \text{const.} \qquad \forall\, t \in (0, \infty).$$

Proof of Theorem 3.4. First it is helpful to point out two relations that will be of use later.

(a) Regarding the components of $\mathbf{u}$ it of course holds that

$$\sum_i u_i (D_j u_i) = \sum_i \frac{1}{2}(D_j u_i^2) = \frac{1}{2}(D_j u^2) = u(D_j u).$$

(b) For $n, m \in \mathbb{N}$ one easily obtains

$$u^n D_i u^m = \frac{m}{n+m} D_i u^{m+n}$$

The i$^{\text{th}}$ component of the Euler-Burgers' equation (3.1) in summation convention reads

$$\underbrace{\partial_t u_i}_{\text{(i)}} + \underbrace{(\mathrm{P}u)_j D_j u_i}_{\text{(ii)}} = \underbrace{\nu D_j D_j u_i}_{\text{(iii)}} + \underbrace{f_i}_{\text{(iv)}} \qquad | \cdot u_i \cdot u^{2n-2} \int_\Omega \tag{3.3}$$

The whole equation (3.3) is scalar multiplied by u_i, multiplied by u^{2n-2} and then integrated over the domain Ω. For the four terms we get

(i) Time derivative:

$$\begin{aligned}\int_\Omega u_i u^{2n-2}(\partial_t u_i)\,\mathrm{d}\mathbf{x} &\overset{(a)}{=} \frac{1}{2}\int_\Omega u^{2n-2}(\partial_t u^2)\,\mathrm{d}\mathbf{x} \\ &\overset{(b)}{=} \frac{1}{2n}\int_\Omega \partial_t u^{2n}\,\mathrm{d}\mathbf{x} \\ &= \frac{1}{2n}\partial_t |u^n|^2\end{aligned}$$

(ii) The Nonlinear term equals zero, because

$$\begin{aligned}\int_\Omega u_i u^{2n-2}(\mathrm{P}u)_j(D_j u_i)\,\mathrm{d}\mathbf{x} &= \frac{1}{2n}\int_\Omega (\mathrm{P}u)_j(D_j u^{2n})\,\mathrm{d}\mathbf{x} \\ &= -\frac{1}{2n}\int_\Omega \underbrace{D_j(\mathrm{P}u)_j}_{=0} u^{2n}\,\mathrm{d}\mathbf{x} \\ &= 0\end{aligned}$$

where one uses the periodic boundary conditions and the solenoidality of $\mathrm{P}\mathbf{u}$.

(iii) The dissipative term provides:

$$\begin{aligned}\int_\Omega u_i u^{2n-2}\nu D_j D_j u_i\,\mathrm{d}\mathbf{x} &= -\nu\int_\Omega (D_j u^{2n-2}u_i)(D_j u_i)\,\mathrm{d}\mathbf{x} \\ &= -2\nu\int_\Omega u^{n-1}u_i(D_j u^{n-1})(D_j u_i)\,\mathrm{d}\mathbf{x} - \underbrace{\int_\Omega u^{2n-2}(D_j u_i)^2\,\mathrm{d}\mathbf{x}}_{>0} \\ &\overset{(a)}{\leq} -2\nu\int_\Omega u^{n-1}(D_j u^{n-1})u(D_j u)\,\mathrm{d}\mathbf{x} \\ &\overset{(b)}{=} -2\nu\int_\Omega \frac{1}{n}(D_j u^n)\frac{n-1}{n}(D_j u^n)\,\mathrm{d}\mathbf{x} \\ &\leq -\frac{2(n-1)\nu}{n^2}\int_\Omega (D_j u^n)^2\,\mathrm{d}\mathbf{x} = -\frac{2(n-1)\nu}{n^2}\|u^n\|^2\end{aligned}$$

(iv) For $f = \sqrt{\sum f_i^2}$, the forcing term can be estimated:

$$\int_\Omega u_i u^{2n-2} f_i \,\mathrm{d}\mathbf{x} \leq \int_\Omega u^{2n-1} f \,\mathrm{d}\mathbf{x}$$

At this point, the scaled Young's inequality (Lemma 3.1), with

$$p = \frac{2n}{2n-1}, \qquad q = 2n \quad \text{and} \quad \varepsilon = \frac{3n-4}{n(2n-1)}\frac{\nu}{C},$$

comes into play, where C is the Poincaré constant for the Poincaré inequality $|u^n|^2 \leq C\|u^n\|^2$ (Theorem 3.1), depending only on the domain Ω. This provides

$$\begin{aligned}\int_\Omega u_i u^{2n-2} f_i \,\mathrm{d}\mathbf{x} &\leq \int_\Omega \left(\frac{3n-4}{2n^2}\frac{\nu}{C}u^{2n}\right)\mathrm{d}\mathbf{x} + \int_\Omega f^{2n}\frac{1}{2n}\left(\frac{C}{\nu}\frac{n(2n-1)}{3n-4}\right)^{2n-1}\mathrm{d}\mathbf{x} \\ &\leq \frac{\nu}{C}\frac{3n-4}{2n^2}|u^n|^2 + \frac{1}{2n}\underbrace{\left(\frac{C}{\nu}\frac{n(2n-1)}{3n-4}\right)^{2n-1}}_{F}|f^n|^2,\end{aligned}$$

F being a positive real constant that depends only on Ω, n and the force $\mathbf{f}$ itself. With the Poincaré inequality applied, we finally get the following estimate for the driving term:

$$\int_\Omega u_i u^{2n-2} f_i \,\mathrm{d}\mathbf{x} \leq \nu\frac{3n-4}{2n^2}\|u^n\|^2 + \frac{1}{2n}F$$

Gathering all remaining parts of equation (3.3) one obtains

$$\frac{1}{2n}\partial_t|u^n|^2 + \nu\left(\frac{2(n-1)}{n^2} - \frac{3n-4}{2n^2}\right)\|u^n\|^2 \leq \frac{1}{2n}F$$

or

$$\partial_t|u^n|^2 + C\lambda\|u^n\|^2 \leq F$$

with $\lambda = \frac{\nu}{C}$ being a positive constant for all $n \in \mathbb{N}$, and depending only on n and Ω. At this point the Poincaré inequality can be applied again, which leads to

$$\partial_t|u^n|^2 \leq -\lambda|u^n|^2 + F$$

The last step involves the use of Gronwall's lemma (Lemma 3.2). For $y = |u^n|^2$, $g = -\lambda$ and $h = F$ one obtains

$$|u(t)^n|^2 \leq |u_0^n|^2 e^{-\lambda t} + \frac{F}{\lambda}\left(1 - e^{-\lambda t}\right),$$

with the initial conditions $u_0 = u(0)$. Thus, with the triangle inequality, we get the final result, which was to be proven,

$$|u(t)^n| \leq \rho_0 \qquad \forall \quad t \in (0, \infty),$$

where $\rho_0 = |u_0^n| + \sqrt{\frac{F}{\lambda}}$ is a constant depending only on n, Ω, the force $\mathbf{f}$ and the initial condition u_0. □

3.2.3 Boundedness of $\|\mathbf{u}\|$

Theorem 3.5. *For the Euler-Burgers' equation (3.1) on the three-dimensional domain $\Omega \subset \mathbb{R}^3$ with periodic boundary conditions and finite and smooth initial conditions $\mathbf{u}(0) = \mathbf{u}_0$, there exists a constant ξ_0 depending only on Ω, the force $\mathbf{f}$ and the initial conditions $\mathbf{u}_0$, such that the $H^1(\Omega)^d$-norm of $\mathbf{u}(t)$*

$$\|\mathbf{u}(t)\| < \xi_0 \tag{3.4}$$

is bounded by ξ_0 for all $t \in (0, \infty)$.

Proof of Theorem 3.5. Both this theorem and its proof resemble Theorem 3.4 in many ways. After scalar multiplication and integration over the domain Ω, a part of the nonlinearity of Euler-Burgers' equation vanishes. What is left can easily be proven to be finite using the Gagliardo-Nirenberg inequality (Theorem 3.3) and Theorem 3.4 from above.

Consider the gradient of the Euler-Burgers' equation:

$$\partial_t \nabla \mathbf{u} + \nabla \left[(\mathrm{P}\mathbf{u}) \cdot \nabla \mathbf{u} \right] = \nu \Delta \nabla \mathbf{u} + \nabla \mathbf{f} \qquad | \cdot \nabla \mathbf{u}, \int_\Omega \tag{3.5}$$

which is then multiplied by the gradient of $\mathbf{u}$:

$$\underbrace{\nabla \mathbf{u} \partial_t \nabla \mathbf{u}}_{\text{(i)}} + \underbrace{\nabla \mathbf{u} \nabla \left[(\mathrm{P}\mathbf{u}) \cdot \nabla \mathbf{u} \right]}_{\text{(ii)}} = \underbrace{\nabla \mathbf{u} \nu \Delta \nabla \mathbf{u}}_{\text{(iii)}} + \underbrace{\nabla \mathbf{u} \nabla \mathbf{f}}_{\text{(iv)}} \tag{3.6}$$

and integrated over Ω. The four parts can be estimated as follows:

(i) Time derivative:

$$\begin{aligned} \int_\Omega \nabla \mathbf{u} \partial_t \nabla \mathbf{u} \, \mathrm{d}\mathbf{x} &= \frac{1}{2} \partial_t \int_\Omega (\nabla \mathbf{u})^2 \, \mathrm{d}\mathbf{x} \\ &= \frac{1}{2} \partial_t \|\mathbf{u}\|^2 \end{aligned}$$

(ii) For the nonlinearity, just a part vanishes due to periodic boundary conditions and the solenoidality of P$\mathbf{u}$:

$$\begin{aligned}
-\int_\Omega \nabla\mathbf{u}\nabla\left(\mathrm{P}\mathbf{u}\cdot\nabla\mathbf{u}\right)\,\mathrm{d}\mathbf{x} &= -\int_\Omega \nabla\mathbf{u}\left(\nabla\mathrm{P}\mathbf{u}\right)\cdot\nabla\mathbf{u}\,\mathrm{d}\mathbf{x} \;-\; \int_\Omega \nabla\mathbf{u}\mathrm{P}\mathbf{u}\cdot\nabla\nabla\mathbf{u}\,\mathrm{d}\mathbf{x} \\
&= \int_\Omega \nabla^2\mathbf{u}\,\nabla\mathrm{P}\mathbf{u}\cdot\mathbf{u}\,\mathrm{d}\mathbf{x} \;-\; \frac{1}{2}\int_\Omega \mathrm{P}\mathbf{u}\cdot\nabla\left(\nabla\mathbf{u}\right)^2\mathrm{d}\mathbf{x} \\
&= \int_\Omega \nabla^2\mathbf{u}\,\nabla\mathrm{P}\mathbf{u}\cdot\mathbf{u}\,\mathrm{d}\mathbf{x} \;+\; \underbrace{\frac{1}{2}\int_\Omega \left(\nabla\cdot\mathrm{P}\mathbf{u}\right)\left(\nabla\mathbf{u}\right)^2\mathrm{d}\mathbf{x}}_{=0} \\
&\leq \int_\Omega |\nabla^2\mathbf{u}||\nabla\mathrm{P}\mathbf{u}||\mathbf{u}|\,\mathrm{d}\mathbf{x}.
\end{aligned}$$

The norm inside the integrals refers to the standard norm instead of the $L^2(\Omega)$-norm. We now make use of the Cauchy-Schwarz inequality ($\langle a,b\rangle^2 \leq \langle a,a\rangle\,\langle b,b\rangle$) twice:

$$\begin{aligned}
\int_\Omega |\nabla^2\mathbf{u}||\nabla\mathrm{P}\mathbf{u}||\mathbf{u}|\,\mathrm{d}\mathbf{x} &\leq \left(\int_\Omega |\nabla^2\mathbf{u}|^2\mathrm{d}\mathbf{x}\right)^{\frac{1}{2}}\left(\int_\Omega |\nabla\mathrm{P}\mathbf{u}|^2|\mathbf{u}|^2\mathrm{d}\mathbf{x}\right)^{\frac{1}{2}} \\
&\leq \left(\int_\Omega |\nabla^2\mathbf{u}|^2\mathrm{d}\mathbf{x}\right)^{\frac{1}{2}}\left(\int_\Omega |\nabla\mathrm{P}\mathbf{u}|^4\mathrm{d}\mathbf{x}\right)^{\frac{1}{4}}\left(\int_\Omega |\mathbf{u}|^4\mathrm{d}\mathbf{x}\right)^{\frac{1}{4}} \\
&= |\nabla^2\mathbf{u}|\;\|\mathrm{P}\mathbf{u}\|_{W^{1,4}(\Omega)}\;|\mathbf{u}|_4
\end{aligned}$$

While the first term will later be estimated by the Poincaré inequality (Theorem 3.1) and the last term is already taken care of by the boundedness of $|u|_n$ (Theorem 3.4), the middle term needs special treatment via the Gagliardo-Nirenberg inequality (Theorem 3.3). For $f = \mathrm{P}\mathbf{u}$ and

$$\begin{aligned}
j = 1, p = 4 \quad \text{and} \quad & m = 2, r = 2, q = 2 \\
\Rightarrow \qquad & a = \frac{7}{8}
\end{aligned}$$

to fulfill the necessary conditions, we get

$$\begin{aligned}
\left(\int_\Omega |\nabla\mathrm{P}\mathbf{u}|^4\mathrm{d}\mathbf{x}\right)^{\frac{1}{4}} &\leq C\left(\int_\Omega |\nabla^2\mathrm{P}\mathbf{u}|^2\mathrm{d}\mathbf{x}\right)^{\frac{7}{16}}\left(\int_\Omega |\mathrm{P}\mathbf{u}|^2\mathrm{d}\mathbf{x}\right)^{\frac{1}{16}} \\
&\leq C|\nabla^2\mathbf{u}|^{\frac{7}{8}}|\mathbf{u}|^{\frac{1}{8}}
\end{aligned}$$

where the last step involves the application of Lemma 3.3 twice to omit the projection operator. Inserted back into the nonlinearity this provides

$$C\|\mathbf{u}\|_4 \, |\nabla^2\mathbf{u}|^{\frac{15}{8}} \, |\mathbf{u}|^{\frac{1}{8}} = K|\nabla^2\mathbf{u}|^{\frac{15}{8}}.$$

Due to the boundedness of $|u|_n$ (Theorem 3.4), K is a constant depending only on Ω, the force $\mathbf{f}$ and the initial conditions $\mathbf{u}_0$. With scaled Young inequality (Lemma 3.1) and $p = \frac{16}{15}$, $q = 16$ and $\varepsilon = \frac{4\nu}{15}$ one obtains

$$\begin{aligned} K|\nabla^2\mathbf{u}|^{\frac{15}{8}} &\leq \frac{\nu}{4}|\nabla^2\mathbf{u}|^2 + \frac{1}{16}\left(\frac{15}{4\nu}\right)^{15} K^{16} \\ &\leq \frac{\nu}{4}|\nabla^2\mathbf{u}|^2 + F_1, \end{aligned}$$

F_1 being a constant again depending only on Ω, the force $\mathbf{f}$ and the initial conditions $\mathbf{u}_0$. We now finally have

$$\int_\Omega \nabla\mathbf{u}\nabla\left(\mathrm{P}\mathbf{u}\cdot\nabla\mathbf{u}\right)\,\mathrm{d}\mathbf{x} \geq -\frac{\nu}{4}|\nabla^2\mathbf{u}|^2 - F_1$$

as estimate for the nonlinearity.

(iii) The dissipative term is equivalent to:

$$\begin{aligned} \int_\Omega \nabla\mathbf{u}\nu\nabla\Delta\mathbf{u}\,\mathrm{d}\mathbf{x} &= -\nu\int_\Omega \left(\nabla^2\mathbf{u}\right)^2\mathrm{d}\mathbf{x} \\ &= -\nu|\nabla^2\mathbf{u}|^2 \end{aligned}$$

(iv) The absolute value of the force provides

$$\begin{aligned} -\int_\Omega \nabla\mathbf{u}\nabla\mathbf{f}\,\mathrm{d}\mathbf{x} &= \int_\Omega \nabla^2\mathbf{u}\mathbf{f}\,\mathrm{d}\mathbf{x} \\ &\leq \frac{\nu}{4}\int_\Omega \left(\nabla^2\mathbf{u}\right)^2\mathrm{d}\mathbf{x} \;+\; \frac{1}{\nu}\int_\Omega \mathbf{f}^2\mathrm{d}\mathbf{x} \\ &\leq \frac{\nu}{4}|\nabla^2\mathbf{u}|^2 + \underbrace{\frac{1}{\nu}|\mathbf{f}|^2}_{F_2} \end{aligned}$$

with the help of the scaled Young's inequality (Lemma 3.1) for the special case $p = q = 2$ and $\varepsilon = \frac{\nu}{2}$.

Now, as the estimates for all four parts (i) – (iv) are complete, we can rewrite equation (3.6) to

$$\frac{1}{2}\partial_t\|\mathbf{u}\|^2 - \frac{\nu}{4}|\nabla^2\mathbf{u}|^2 - F_1 \leq -\nu|\nabla^2\mathbf{u}|^2 + \frac{\nu}{4}|\nabla^2\mathbf{u}|^2 + F_2$$

or with $F_1 + F_2 = F$:

$$\partial_t\|\mathbf{u}\|^2 \leq -\nu|\nabla^2\mathbf{u}|^2 + F. \tag{3.7}$$

Since $\|\mathbf{u}\|^2 \leq C|\nabla^2\mathbf{u}|^2$ due to Poincaré inequality, we get

$$\partial_t\|\mathbf{u}\|^2 + \tau\|\mathbf{u}\|^2 \leq F$$

with $\tau = \frac{\nu}{C}$. Gronwall's Lemma (Lemma 3.2) with $y = \|\mathbf{u}\|^2$, $g = \tau$ and $h = F$, such that

$$\|\mathbf{u}(t)\|^2 \leq \|\mathbf{u}_0\|^2 e^{-\tau t} + \frac{G}{\tau}\left(1 - e^{-\tau t}\right),$$

proves the statement

$$\|\mathbf{u}(t)\| \leq \xi_0$$

for all $t \in [0, \infty]$, where ξ_0 is a constant depending only on Ω, the force $\mathbf{f}$ and the initial conditions $\mathbf{u}_0$. □

3.3 Uniqueness and regularity

As the question of existence of solutions is now positively answered, the remaining open problem is to establish uniqueness of these solutions. It will be shown in the following section that this question is inseparably connected to the regularity of the solutions.

3.3.1 Regularity

Since the boundedness of both $|u(t)|$ and $\|u(t)\|$ was proven, regularity is deduced by standard methods of Ladder theorems, presented e.g. in Doering and Gibbon [1995]. Without going into further details the following, thus, holds true:

Lemma 3.4 (Regularity of the Solutions)**.** *The $L^\infty(\Omega)$-norm of $\nabla\mathbf{u}$ is integrable in time*

$$\int_0^T |\nabla\mathbf{u}(\cdot, t)|_\infty \,\mathrm{d}t \leq C(T)$$

for all $T \in (0, \infty)$.

This is weaker than what could actually be proven, as here singularities, which are integrable in time, are still allowed to exist. However, the above lemma turns out to be sufficient to prove the uniqueness of the solution.

3.3.2 Uniqueness

The standard procedure to show uniqueness of a solution is to consider two different solutions $\mathbf{u}(\mathbf{x},t)$ and $\mathbf{u}'(\mathbf{x},t)$, which both have the same initial conditions $\mathbf{u}_0 = \mathbf{u}'_0$ and satisfy the Euler-Burgers' equation (3.1). It is then possible to infer another "energy"-type evolution equation from Euler-Burgers' equation for the difference of both solutions, $\mathbf{v} = \mathbf{u} - \mathbf{u}'$, to prove the uniqueness.

Theorem 3.6 (Uniqueness of Solutions)**.** *Let $\mathbf{u}(\mathbf{x},t)$ and $\mathbf{u}'(\mathbf{x},t)$ be two solutions to the Euler-Burgers' equation (3.1) on the three-dimensional domain $\Omega \in \mathbb{R}^3$ with periodic boundary conditions. If at $t = 0$ both solutions are equal,*

$$\mathbf{u}_0(\mathbf{x}) = \mathbf{u}'_0(\mathbf{x}) \qquad \forall\, \mathbf{x} \in \Omega,$$

then both solutions are equal for all times $t \in [0, \infty]$.

Proof of theorem 3.6. Let $\mathbf{u}(\mathbf{x},t)$ and $\mathbf{u}'(\mathbf{x},t)$ be two solutions of Euler-Burgers' equation (3.1) with identical initial conditions $\mathbf{u}(\cdot,0) = \mathbf{u}'(\cdot,0)$. For $\mathbf{v} = \mathbf{u} - \mathbf{u}'$ we get

$$\underbrace{\partial_t \mathbf{v}}_{\text{(i)}} + \underbrace{(\mathrm{P}\mathbf{v}\cdot\nabla)\,\mathbf{v}}_{\text{(ii)}} + \underbrace{(\mathrm{P}\mathbf{v}\cdot\nabla)\,\mathbf{u}}_{\text{(iii)}} + \underbrace{(\mathrm{P}\mathbf{u}\cdot\nabla)\,\mathbf{v}}_{\text{(iv)}} = \underbrace{\nu\Delta\mathbf{v}}_{\text{(v)}}, \tag{3.8}$$

by making use of the linearity of ∇ and P. After scalar multiplication by $\mathbf{v}$ and integrating over the domain, each part can be estimated.

(i) The time derivative is equal to

$$\int_\Omega \mathbf{v}\cdot\partial_t\mathbf{v}\,\mathrm{d}\mathbf{x} = \frac{1}{2}\partial_t|\mathbf{v}|^2$$

(ii) As the nonlinearity is split into three parts, I will treat them one by one. All but one will vanish due to solenoidality of the projected field.

$$\begin{aligned}\int_\Omega v_i \mathrm{P}v_j\partial_j v_i\,\mathrm{d}\mathbf{x} &= \frac{1}{2}\int_\Omega \mathrm{P}v_j\partial_j v_i^2\,\mathrm{d}\mathbf{x}\\ &= -\frac{1}{2}\int_\Omega \underbrace{\partial_j \mathrm{P}v_j}_{=0}\, v_i^2\,\mathrm{d}\mathbf{x}\\ &= 0\end{aligned}$$

(iii) The second part of the nonlinearity provides

$$\begin{aligned}\int_\Omega v_i \mathrm{P}v_j\partial_j u_i\,\mathrm{d}\mathbf{x} &\le |\partial_j u_i|_\infty \int_\Omega v_i \mathrm{P}v_j\,\mathrm{d}\mathbf{x}\\ &\le |\partial_j u_i|_\infty\, |v|\, |\mathrm{P}v|\\ &\le |\partial_j u_i|_\infty\, |v|^2,\end{aligned}$$

where the last step involves the application of lemma 3.3.

(iv) The third part of the nonlinearity is zero with exactly the same argument as in (ii), $\mathrm{P}v_j$ being replaced by $\mathrm{P}u_j$, both solenoidal.

(v) No surprise for the dissipative term,

$$\begin{aligned}\nu \int_\Omega \mathbf{v} \cdot \Delta \mathbf{v} \, \mathrm{d}\mathbf{x} &= -\nu \int_\Omega (\nabla \mathbf{v})^2 \, \mathrm{d}\mathbf{x} \\ &= -\nu \|v\|^2 \\ &\geq -\frac{\nu}{C} |v|^2,\end{aligned}$$

using the Poincaré inequality (Theorem 3.1) in the last step.

The estimate for the evolution equation (3.8) for $\mathbf{v}$ now looks like

$$\frac{1}{2} \partial_t |\mathbf{v}|^2 \leq -\frac{\nu}{C} |\mathbf{v}|^2 + |\nabla \mathbf{u}|_\infty \, |\mathbf{v}|^2.$$

Applying Gronwall's Lemma (Lemma 3.2) we deduce that

$$|\mathbf{v}(t)|^2 \leq |\mathbf{v}_0| \exp\left(-\frac{\nu}{C} t + \int_0^t |\nabla \mathbf{u}(\tau)|_\infty \, \mathrm{d}\tau \right)$$

for all $t \in (0, \infty)$. Because of $|\mathbf{v}_0| = 0$, since the initial conditions are the same ($\mathbf{u}_0 = \mathbf{u}'_0$), it holds $\mathbf{v}(t) = 0$ for all times and, thus, $\mathbf{u} = \mathbf{u}'$. Therefore, two solutions with identical initial conditions stay the same for all times. □

3.4 Summary

In the sections above we have proven that the solutions to the Euler-Burgers' equation

$$\partial_t \mathbf{u} + (\mathrm{P}\mathbf{u} \cdot \nabla)\mathbf{u} = \nu \Delta \mathbf{u} + \mathbf{f}$$

exist and are unique. By standard methods, which were not discussed above, it is possible to also deduce that $|\nabla \mathbf{u}|_\infty$ is not only square integrable in time, but also finite. The same actually holds for all higher derivatives of the velocity field. It is, therefore, impossible for singularities or discontinuities to build up in finite time. The solutions to Euler-Burgers' equation are sufficiently smooth or "well-behaved" for all times. The Euler-Burgers' model equation, thus, proves to be a potentially good predictive hydrodynamical model.

Chapter 4

Numerics

While the previous chapters focused upon theoretical questions regarding the global behavior of different hydrodynamical models, it is helpful to solve the differential equations with numerical integration in order to get a clearer picture of the structures that evolve. In the following sections I will first briefly summarize the equipment and numeric framework used to carry out the simulations (section 4.1), then describe my two approaches to solve the equations (in sections 4.2 and 4.3). Both need the solution of the Poisson equation, which I obtain using a parallelized multigrid method (see Appendix B for details). In the end of this chapter in section 4.4 I will present the two different initial conditions that will be used in all simulations of the following two chapters on turbulence (chapter 5) and singularities (chapter 6).

4.1 Simulation of hydrodynamical models

The simulation of the Navier-Stokes equation or Euler equation began as soon as computers became fast enough to solve the simplest problems. While most of these computations focused on particular (engineering) questions like the design of airfoils, theoretical physicists also began to make use of numerical simulations to support their theories and to complement experimental data. The study of turbulent flows has gained a lot from these simulations. In the case of Euler singularities, more recent mathematical theories further encourage numerical simulations as a tool to analyze the geometry of vortex lines.

4.1.1 Tools and equipment

The simulation of hydrodynamical models is affected by the need for higher resolutions. Independent of the problem in question, both the search for singularities and the analysis of turbulence lay their hope in a finer mesh to resolve the structures that evolve. Due to the amount of detail much memory obviously is needed. State-of-the-art simulations are, therefore, employing parallel computing, making use of many CPUs at the same time. As the days of shared memory architectures seem to be gone at least for high performance computing, architectures with distributed cores are nowadays preferred.

For the simulations in this thesis the Institute's Linux Opteron Cluster with 32 nodes (4 CPUs/8 GB RAM each) was used. Parts of the computation and scaling tests were carried out on the BlueGene/P (Jugene) in Forschungszentrum Jülich (`http://www.fz-juelich.de/jsc/`).

For the communication between different processes of the application, the Message Passing Interface (MPI) is used. It is a common standard among parallel programs and supports various operations needed for efficient data exchange on multiple communication layers. A complete overview of the MPI standard with many helpful examples can be found in the IBM Redbook on MPI Programming (Aoyama and Nakano [1999]). Several implementations of the standard exist, of which openMPI (see `http://www.open-mpi.org/`, OpenMPI [2006]) is actually used throughout my computations.

4.1.2 *racoon II*

To implement the simulation of all three hydrodynamical models, *racoon II* (refined adaptive computations with object-oriented numerics) is used. It supports adaptive, parallel integration of partial differential equations in both 2D and 3D. Several integration and reconstruction schemes can be applied and additional modules to solve elliptic problems or add Lagrangian particles are available. It was implemented in C++ by Jürgen Dreher (see Dreher and Grauer [2005] for more details).

Grid and blocks

The discretized computational domain equals a mesh in memory. The values at each mesh point represent the value of a physical field at the center, the edge or the corner of a cell, or the spatial average of this field across the cell (see figure 4.1). Data distribution across the processes is realized by using *blocks* of fixed size n (typically from 8 to 64 cells in each direction) arranged on different *levels* L, representing the degree of refinement. The 0^{th} level consists of only one block, stretching across the whole computational domain, while the subsequent levels bisect the parent blocks in each dimension, resulting in $2^{L \cdot d}$ blocks on level L (d being the dimension of the domain). This leads to a total resolution of $(n \cdot 2^L)^d$ mesh points.

Each block is surrounded with at least two *boundary cells* as pictured in figure 4.1, to ensure that each cell has two valid neighbors throughout the computation. This is necessary for numerous computation steps such as derivations via finite differences or error smoothing. These "ghost cells" overlap with the neighboring block and mirror its data. To synchronize after an integration step, all boundary cells are exchanged with their neighbors.

As *racoon II* is object-oriented, the implementation of the differential equation in question takes place when deriving a problem-specific class from the virtual `problem`-class. Several callback functions, invoked by the main loop on each node and the time-integration scheme, allow for data manipulation, output and diagnostics. Also, the problem class is the only place where the actual physical equations are located. It is, thus, easy to change the problem formulation without the need of rewriting code distributed over several files.

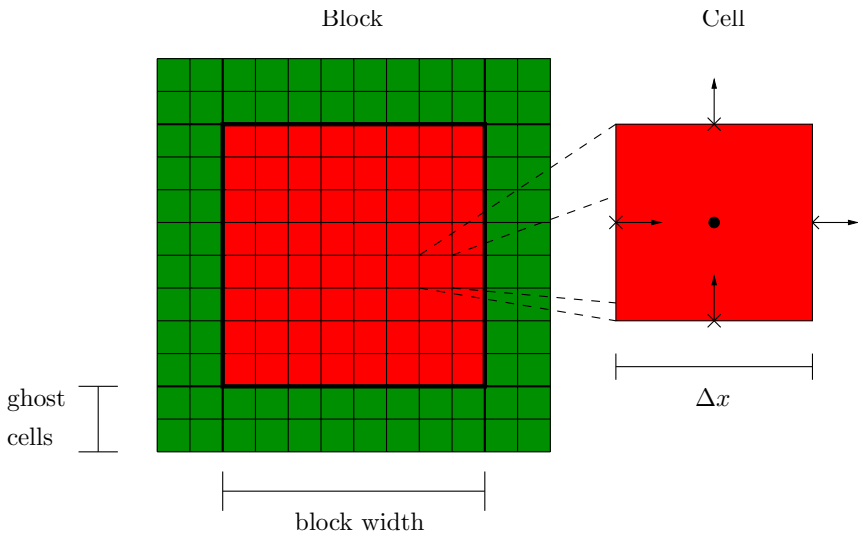

Figure 4.1: A **block** in *racoon II* has a fixed number of inner cells (red, here 8x8), surrounded by **boundary cells** (green) that hold copies of the data of neighboring cells. Every **cell** can store a value for each field, located either in the center, at the boundaries, at the edges or at the vertices of the cell.

Furthermore, the integration scheme, the interpolation method or other purely numeric modules can be replaced without altering the physical equations.

Adaptive mesh refinement and dynamic load balancing

A key feature of *racoon II* is its ability to refine the grid adaptively. Many problems in physics in general and particularly in hydrodynamics exhibit structures that are strongly localized in small areas needing high resolution, while the rest of the domain is virtually empty. With a fixed mesh one has the choice between under-resolving the whole problem or wasting computing-resources and time. For example, when simulating colliding vortex tubes as in the Kida-Pelz initial conditions (see section 4.4.2), the evolving fine structures have to be resolved as much as possible, while the trails do not require that much attention.

Adaptive mesh refinement (AMR) avoids this problem by allowing to adjust the resolution depending on the problem. In *racoon II*, a certain criterion is tested periodically and for each block. The criterion is defined in the problem and depends, for example, on the fields, its derivatives or a more complicated formula. If the block is flagged as being under-resolved, it is bisected into 2^d child blocks that are redistributed among the available nodes. The resolution of the parent block is thus effectively doubled. The same happens for blocks that are over-resolved: 2^d blocks are merged into one, the resolution at this location is halved. With this procedure, the grid is constantly changing and adapting to the simulation, allowing high resolution at critical locations but not wasting any resources for the rest.

Since communication between different nodes is the smallest bottleneck due to lim-

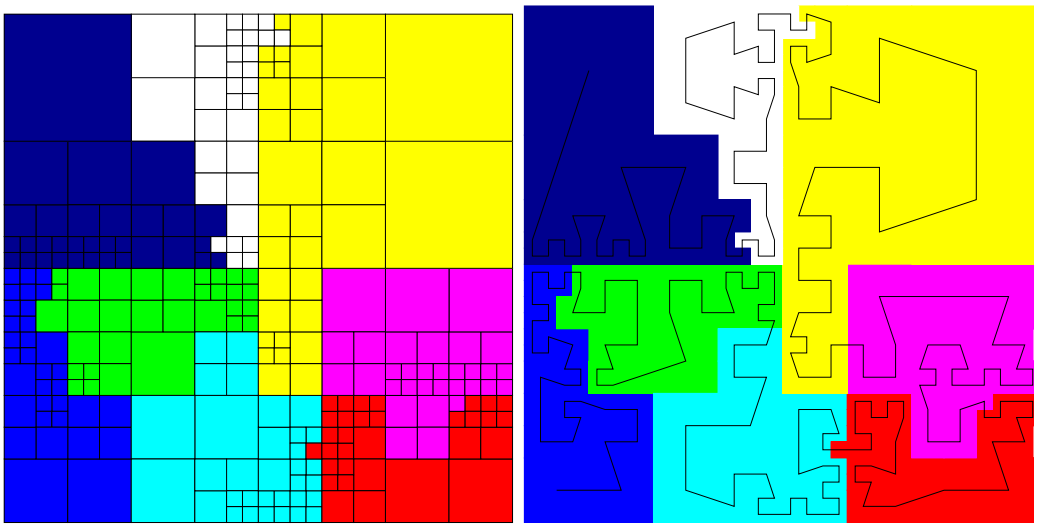

Figure 4.2: Adaptive mesh refinement and dynamic load balancing in *racoon II*. The workload is distributed among different processors (here 8 processors, denoted by colors) along a space-filling Hilbert curve.

ited bandwidth and high latency, it is advantageous to arrange the blocks in a way that physically close blocks are located on the same node. Even if this seems to be pretty straight-forward for normal grids, it poses a larger problem for adaptive grids with different resolutions. In *racoon II*, blocks are distributed along a space-filling Hilbert curve, as pictured in figure 4.2. This ensures that proximate blocks are located on the same node even if the grid is not fixed. Currently *racoon II* uses a slightly different approach, using independent Hilbert curves for each level, since inter-level communication is the most frequent type of communication for common problems. Every time the grid changes when adapting to the current situation, the Hilbert curve is recalculated, as is the workload for each node. If an imbalance is detected, the blocks are redistributed along the curve, each node getting the same amount of blocks (if possible).

AMR is an indispensable tool for many different problems, including the search for Euler singularities. As for hydrodynamical turbulence, which is believed to be isotropic and homogeneous, AMR seems to be less useful, because the flows do not feature distinguished locations of interest. Therefore, AMR is not used in any turbulence simulation in this thesis. A good examination of the use of AMR in combination with turbulence is given in Beetz [2006].

4.1.3 Integration scheme and time step

Consider a discretized partial differential equation of the form

$$\partial_t y(\mathbf{x}, t) = f(t, y), \tag{4.1}$$

where f is a differential operator, consisting of spatial derivatives. The simplest method of calculating the spatial derivatives is the method of finite differences, which resembles the discretized formulation of the difference quotient. Though *racoon II* utilizes the CWENO (central weighted essentially non-oscillatory) scheme of Kurganov and Levy [2000], all simulations featured in this thesis make use only of basic *finite difference* schemes, since the CWENO approach is just implemented for cell-centered grids. In this thesis, the method of *central differences* is used, for which the first derivative is defined as

$$D(y(x_0)) = \frac{y(x_0 + \Delta x) - y(x_0 - \Delta x)}{2\Delta x}.$$

This operation is exact up to second order. Higher derivatives subsequently follow from a Taylor-expansion.

To integrate a partial differential equation of form (4.1) in time, a third-order Runge-Kutta according to Shu and Osher [1988] is used. Written in its general form, the time integration in s steps is carried out via

$$y_{n+1} = y_n + \Delta t \sum_{i=1}^{s} b_i k_i,$$

where

$$k_i = f(t_n + c_i \Delta t, y_n + \sum_{j=1}^{i-1} a_{ij} \Delta t k_j).$$

The constants a_{ij}, b_i and c_i specify the particular method and order of the scheme. For *racoon II*, this method is implemented up to third order.

The time stepping Δt is estimated periodically and problem-depending by invoking a virtual method that calculates the maximal integration step for each block independently and takes the minimum for the next time steps, adhering the Courant-Friedrichs-Lewy (CFL) condition,

$$\Delta t \leq \mathrm{cfl} \frac{\Delta x}{v_{\max}},$$

where cfl is a real constant and $v_{\max}$ the maximum speed for the advancement of information. For reasons of simplicity grid-adaptive time stepping is no longer supported in *racoon II*, and Δx refers to the minimum grid spacing in AMR simulations.

4.2 Vorticity formulation

The Navier-Stokes equation, written in **vorticity formulation**, reads

$$\partial_t \boldsymbol{\omega} = \nu \Delta \boldsymbol{\omega} - \nabla \times ((\mathbf{u} \cdot \nabla)\, \mathbf{u}) \tag{4.2}$$

(compare with equation (2.15)). I used this expression as the basis for one of the two presented methods of numerically integrating the Navier-Stokes equation.

4.2.1 The basic idea

Using equation (4.2) as basic equation, the vorticity field $\boldsymbol{\omega}(\mathbf{x}, t)$ becomes the main field for time integration. To recalculate the velocity field $\mathbf{u}(\mathbf{x}, t)$, similar to electromagnetism, a vector potential $\mathbf{A}(\mathbf{x}, t)$ is used, which obeys $\nabla \times \mathbf{A} = \mathbf{u}$ for all times. As $\mathbf{u}$ now is the curl of the vector potential, its solenoidality is ensured. For $\boldsymbol{\omega}$ it holds

$$\begin{aligned}\boldsymbol{\omega} &= \nabla \times \nabla \times \mathbf{A} \\ &= \nabla (\nabla \cdot \mathbf{A}) - \Delta \mathbf{A} \\ &= -\Delta \mathbf{A},\end{aligned}$$

where the last step involves the solenoidality of the vector potential, $\nabla \cdot \mathbf{A} = 0$, which might not necessarily be true. It can easily be seen that this is without consequence for the method: Suppose $\tilde{\mathbf{A}} = \mathrm{P}\mathbf{A}$ is the solenoidal part of $\mathbf{A}$,

$$\mathbf{A} = \tilde{\mathbf{A}} + \nabla\varphi,$$

where φ is an appropriate scalar field. Then

$$\begin{aligned}\boldsymbol{\omega} &= \nabla(\nabla \cdot \nabla\varphi + \underbrace{\nabla \cdot \tilde{\mathbf{A}}}_{=0}) - \Delta \mathbf{A} \\ &= \nabla\Delta\varphi - \Delta \mathbf{A} \\ \Rightarrow \quad \mathbf{A} &= -\Delta^{-1}\boldsymbol{\omega} + \nabla\varphi \\ \Rightarrow \quad \tilde{\mathbf{A}} &= -\Delta^{-1}\boldsymbol{\omega}.\end{aligned}$$

Obviously, to derive the velocity $\mathbf{u}$ from $\boldsymbol{\omega}$, one has to solve the Poisson equation

$$\Delta \mathbf{A} = -\boldsymbol{\omega} \tag{4.3}$$

in three components.

4.2.2 Implementation

All permanently stored fields (the vorticity $\boldsymbol{\omega}$ and the vector potential A) reside in the center of each cell. Integrating a time step basically consists of a call to `RK::doStep()`, which loops through the Runge-Kutta substep, invoking the callback function `problem::singleStep(block, dt)` for each block. The function `RK::applyFraction` applies the results of the last substep to the previously stored values of the integrated fields, the weighting depending on the order of the scheme (see section 4.1.3). Finally, `problem::subStepComplete()` is called to prepare the fields for the next substep.

Figure 4.3 shows a simplified summary of a complete time step, some of the functions needing further explanation:

calcSpeed: For each Runge-Kutta substep and each block on the computational domain, the speed has to be calculated from the vector potential via

$$\mathbf{u} \leftarrow \nabla \times \mathbf{A}.$$

```
for each RK_Substep {
  for each local Block {
    singleStep {
      calcSpeed;
      calcNonlinearity;
      applyNonlinearity;
    }
  }
  applyFraction;
  subStepComplete {
    applyViscosity;
    solveA;
  }
}
```

Figure 4.3: Pseudocode for a simplified single time step in vorticity formulation with Runge-Kutta integration for the vorticity formulation.

The speed is just temporarily stored for each block to save memory (though it can be dumped as output-field if the associated flag is set)

calcNonlinearity: After the speed is calculated for a block, it is immediately used to compute the nonlinearity by setting

$$\mathbf{N} \leftarrow (\mathbf{u} \cdot \nabla)\,\mathbf{u}.$$

The nonlinearity is also stored block-wise due to memory issues.

applyNonlinearity: With the values for nonlinearity calculated for the current substep and block, time integration is applied by

$$\boldsymbol{\omega}^{n+1} \leftarrow \boldsymbol{\omega}^{n} - \mathrm{dt}\nabla \times \mathbf{N},$$

where dt is the time step for the current Runge-Kutta substep.

applyViscosity: Right after the integration of a substep, the whole field is damped by applying viscosity (or hyperviscosity):

$$\boldsymbol{\omega} \leftarrow \boldsymbol{\omega} + \begin{cases} \mathrm{dt}\ \nu\Delta\boldsymbol{\omega} \\ \mathrm{dt}\ \nu\Delta^2\boldsymbol{\omega} \end{cases}$$

The boundary cells have to be exchanged before this operation.

solveA: The last thing to do after each substep is to recalculate the vector potential $\mathbf{A}$,

$$\mathbf{A} \leftarrow \Delta^{-1}\boldsymbol{\omega},$$

where Δ^{-1} is computed via multigrid. A more detailed overview of the multigrid algorithm can be found in Appendix B. A boundary exchange in $\mathbf{A}$ afterwards ensures correct values in the ghost cells even for diagonal partners (which might not be done in the multigrid exchange itself).

Since now every field is updated and all boundaries are exchanged, the whole process can begin anew.

4.2.3 Advantages and disadvantages

Several advantages are direct consequences of the way the *vorticity formulation* is constructed:

- The time integrated field is $\boldsymbol{\omega}$, the critical field for finite time blow-up criteria. Every interpolation during boundary transfer and adaptive mesh refinement, therefore, operates on $\boldsymbol{\omega}$ and allows for a smoother transition between changing resolutions, effectively diminishing errors that would occur when differentiating an interpolated quantity.
- As all non-temporary fields are located on a cell-centered grid, the implementation of AMR is pretty straightforward. One can directly employ the methods provided by *racoon II*.
- The incompressibility condition is automatically met.

On the other hand, the specialized way the equation is solved results in two noteworthy disadvantages:

- The Poisson equation (4.3) for the vector potential $\mathbf{A}$ has to be solved in three components. Since the multigrid is the most time-intensive part of the computation, the vorticity formulation is nearly three times slower than the staggered grid formulation.
- The vorticity formulation is only available when considering the Navier-Stokes equation. The Burgers' or Euler-Burgers' equation have no vorticity-type equation counterpart.

Thus, the vorticity formulation is of no use when comparing the three models, but is the choice for highly resolved adaptive simulations, as needed in finite-time vorticity blowup scenarios.

4.3 Staggered grid formulation

The projection operator P, introduced in section 2.2.2, can be constructed numerically. It models the effect of the pressure term ∇p in keeping the velocity field solenoidal. The remaining equation for the case of undriven Navier-Stokes reads

$$\partial_t \mathbf{u} + (\mathrm{P}\mathbf{u} \cdot \nabla)\, \mathrm{P}\mathbf{u} = \nu \Delta \mathbf{u},$$

where P$\mathbf{u}$ corresponds to the physical velocity field, $\mathbf{u}$ being a compressible vector field without a physical counterpart in reality. The pressure $p = \partial_t \varphi - \nu \Delta \varphi$ is absorbed in $\partial_t \mathbf{u} = \partial_t \mathrm{P}\mathbf{u} + \nabla p$ and $\nu \Delta \mathbf{u} = \nu \Delta \mathrm{P}\mathbf{u} + \nu \Delta \nabla \varphi$.

4.3.1 The basic idea

When modeling the projection operator

$$\mathrm{P}\mathbf{u} = \mathbf{u} - \nabla \left(\Delta^{-1} \nabla \cdot \mathbf{u} \right),$$

one has to solve the non-local operator Δ^{-1}, which is implemented via a multigrid algorithm (details are given in Appendix B).

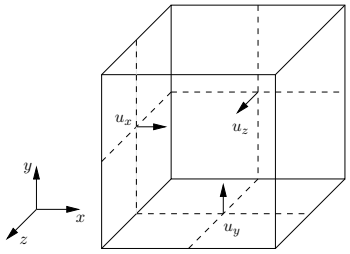

Figure 4.4: Alignment of the velocity field data for the staggered grid formulation. Each velocity component resides in the center of the lower limiting plane of a cell.

The velocity field $\mathbf{u}$ resides on a *staggered grid*. As pictured in figure 4.4 each component of the field is centered on the "lower" plane of the cell. When deriving the velocity via central differences, the stencil just spans over Δx instead of $2\Delta x$. This alignment was introduced by Harlow and Welch [1965].

4.3.2 Implementation

The simplified time step for the staggered grid method differs in some ways from the vorticity formulation. As time-integration scheme, a third-order Runge-Kutta is utilized again. In addition to the already mentioned callback functions `problem::singleStep` and `problem::subStepComplete`, invoked by the integration scheme during and after each substep, `problem::initSubStep` is called right before a substep. Here the projection of $\mathbf{u}$ onto its solenoidal part P$\mathbf{u}$ is carried out.

A summary of a complete time step is outlined in Figure 4.5, further explanations to some of the functions are given below.

```
for each RK_Substep {
  initSubstep {
    project;
  }
  for each local Block {
    singleStep {
      timeStep;
    }
  }
  applyFraction;
  subStepComplete {
    applyViscosity;
  }
}
```

Figure 4.5: Pseudocode for a simplified single time step in staggered grid formulation with Runge-Kutta integration for the vorticity formulation.

project: At the beginning of each substep, the projection operator is numerically executed. First, the Poisson equation

$$\varphi \leftarrow \Delta^{-1}(\nabla \cdot \mathbf{u})$$

is solved via multigrid. For a detailed explanation of the multigrid algorithm, see Appendix B. After that, the projection is carried out via

$$\mathrm{P}\mathbf{u} \leftarrow \mathbf{u} - \nabla\varphi.$$

$\mathrm{P}\mathbf{u}$ now contains the solenoidal part of $\mathbf{u}$. The accuracy of the solenoidality of $\mathrm{P}\mathbf{u}$ can exactly be tuned via the exit condition of the Poisson solver.

timeStep: For each block of the computational domain, an Euler-step is applied as time-integration,

$$\mathbf{u}^{n+1} \leftarrow \mathbf{u}^n - (\mathbf{L} \cdot \nabla)\,\mathbf{R},$$

Model equation	$\mathbf{L}$	$\mathbf{R}$
Burgers'	$\mathbf{u}$	$\mathbf{u}$
Euler-Burgers'	$\mathrm{P}\mathbf{u}$	$\mathbf{u}$
Navier-Stokes	$\mathrm{P}\mathbf{u}$	$\mathrm{P}\mathbf{u}$

Table 4.1: Choice of velocity fields of the nonlinear term for the three different hydrodynamical models in the staggered grid method.

where **L** and **R** mean left and right field respectively, which are chosen corresponding to table 4.1. This way, all three hydrodynamical models can be simulated with the same code, changing just the appropriate preprocessor flag.

applyViscosity: When the time integration is complete, the compressible velocity field **u** is damped by applying viscosity (or hyperviscosity):

$$\mathbf{u} \leftarrow \mathbf{u} + \begin{cases} \mathrm{dt}\ \nu\Delta\mathbf{u} \\ \mathrm{dt}\ \nu\Delta^2\mathbf{u} \end{cases}$$

The boundary cells of **u** have to be exchanged prior to this operation.

The Runge-Kutta substep is now complete and all fields are updated.

4.3.3 Advantages and disadvantages

The staggered grid formulation implies certain advantages:

- All three hydrodynamical models are naturally implemented. Just a flag needs to be set to switch between the models. This allows for a direct comparison of the results of the models without the danger of introducing differences due to different numerical implementations.
- The projection method as solution to the incompressibility condition, though still a Poisson equation, has to be solved just for a scalar field. This is a drastic speed-up in comparison to the vorticity formulation.

  The remaining divergence of the incompressible field can be smoothly adjusted via parameters of the multigrid solver, allowing for a continuous transition between performance and accuracy.

However, some disadvantages of this method are inevitable:

- As opposed to the vorticity method, the velocity **u** instead of the critical quantity $\boldsymbol{\omega}$ is the integrated field. Determining the vorticity from the velocity means a derivative, which decreases the order of accuracy.
- The exceptional grid alignment on the borders, edges or vortices of a cell is not naturally integrated into the computational framework (*racoon II*, see section 4.1.2). While this can be worked around for a fixed grid, AMR is impossible yet for the staggered grid formulation.

The staggered grid method is the optimal choice for the study of turbulence, where adaptive grids are of less importance and accuracy can be traded for performance. It allows the direct comparison of all three hydrodynamical models without much numerical effort. For the examination of singular structures, AMR is indispensable and the staggered grid formulation should not be used.

4.4 Initial conditions

For the integration of differential equations one has to define the initial- and boundary conditions. While the boundaries of the computational box are assumed as periodic and typically do not require further thought, the initial conditions of the physically relevant values have to be chosen in a way that the desired effects develop after short computational time. For simplicity and comparability both velocity and its solenoidal projection are set to equal values, thus the velocity field has itself to be divergence free. I decided to use two distinct initial conditions, one to focus on the behavior of the turbulent flow (see section 4.4.1) and another to study the development of singularities (see section 4.4.2). For turbulent flows, all three hydrodynamical models presented in chapter 2 are compared. For this I use the staggered grid formulation. For the study of Euler Singularities a high symmetry scenario of colliding vortex tubes is implemented. The results and conclusions for turbulence and Euler singularities are presented in chapters 5 and 6, respectively.

4.4.1 Orszag-Tang-like initial conditions

To get a picture of the development of structures in turbulent flows for all of the model equations I had to use initial conditions that evolve into chaotic behavior from initially large-scale perturbations, yet still are isotropic. They also should be smooth, periodic in each direction and divergence free. The straightforward initial conditions that comply with the requirements are a combination of sine and cosine functions, which obviously are smooth and periodic and can easily be chosen as solenoidal. The original Orszag-Tang initial conditions (see Orszag and Tang [1979]) were created for a solenoidal magnetic field in MHD. They also ascertained point symmetry about the origin, which the Euler/Navier-Stokes equations conserve. I used modifications to the Orszag-Tang-like initial conditions proposed by Beetz [2006] that break the point symmetry for a solenoidal velocity field

$$\begin{aligned} u_x &= A\left(-2\sin(2y) + \sin(z) + 2\cos(2y) + \cos(z)\right) \\ u_y &= A\left(-2\sin(x) + \sin(z) + 2\cos(x) + \cos(z)\right) \\ u_z &= A\left(\sin(x) + \sin(y) - 2\cos(2x) + \cos(y)\right). \end{aligned}$$

The domain stretches from $-\pi$ to π, the above defined conditions, thus, are both large-scale perturbations and periodic. All hydrodynamical models will be simulated in comparison, using these initial conditions.

4.4.2 Kida-Pelz initial conditions

In the search for numerical verification of finite time singularities in incompressible flows, several promising initial conditions have been thoroughly tested. As typical for small scale structures and rapid growth of physical quantities, the deciding aspect to distinguish between singular and just near-singular growth is the resolution of the simulation. An essential step in this direction was done by Kida [1985] and later Boratav and Pelz [1994], who elaborated a highly symmetric scenario of colliding vortex-tubes. The symmetry

allows for an easier numerical treatment, as only one eighth of the computational domain has to be simulated. Therefore, higher resolutions are achievable.

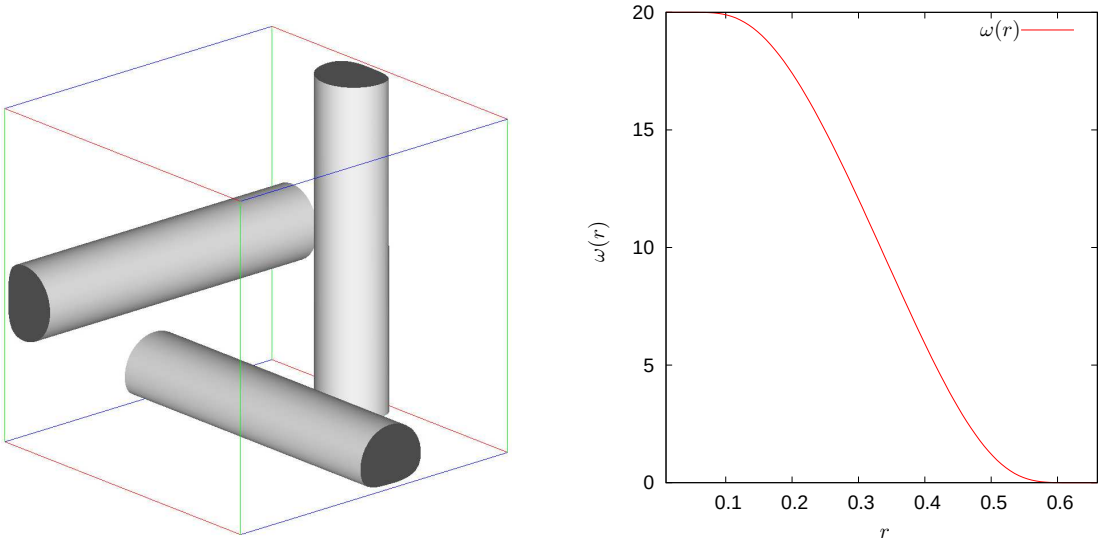

Figure 4.6: The Kida-Pelz initial conditions: **Left:** An octant of the initial vorticity field. Three vortex tubes are visible, one in each direction. **Right:** The profile of each vortex tube. The maximum vorticity at the centerline is 20 and decreases nearly smoothly to 0.

The computational domain is filled with twelve vortex tubes, four in each direction. The simulated octant contains three tubes, as pictured in figure 4.6 (left). The boundary conditions are symmetric for the normal component of the vorticity and antisymmetric for the tangential components. The vorticity profile for each of the tubes is given by

$$\omega(r) = \begin{cases} -20\left[1 - \exp\left(-e^2 \log(2) \frac{1}{3r} \exp\left(\frac{1}{\frac{3r}{2} - 1}\right)\right)\right] & \text{for } r < \frac{2}{3} \\ 0 & \text{for } r \geq \frac{2}{3} \end{cases}$$

where r denotes the distance to the vortex tube centerline. Even though each tube is cylinder symmetrical, due to superposition with neighboring tubes, the cross section is non-circular. The vorticity profile for a single tube is plotted in figure 4.6 (right). For $r \geq \frac{2}{3}$ the vorticity is set to zero.

Chapter 5

Turbulence

Turbulence is an omnipresent phenomenon, easily observable on various occasions. For everyday "fluids" like air or water it may well be regarded as the natural state of motion. Even if the generating processes of turbulent flows vary in both scale and nature, their characteristic features obviously resemble each other. Common to them is the chaotic, unpredictable behavior, the evolution of whirls on a large range of scales and the brisk variation of properties like pressure or velocity in space and time. However, the accurate modeling of turbulent flows is still an open problem (or even the last great problem of classical physics) and their universal and intrinsic properties are not yet completely understood.

Since the underlying equations are well known and are also believed to describe the phenomenon of turbulence accurately, it may seem strange to speak of the "problem of turbulence" in the first place. Even if the analytical solution is out of reach, numerically it should be possible to simulate any phenomenon with arbitrary precision. How futile this attempt would be can easily be realized: The *number of degrees of freedom* of a turbulent flow (see Frisch [1995] p. 107 for details), and hence the minimum number of grid points necessary to resolve every aspect of the flow, scales with the Reynolds number (as defined in equation (2.9)) like

$$N \propto R^{\frac{9}{4}}. \tag{5.1}$$

Even for supposedly simple problems like a car moving through air at the moderate speed of 30 $\frac{\text{km}}{\text{h}}$, the Reynolds number is about $R = 275000$. For a fully resolved simulation of this scenario this would mean a memory requirement of approximately 37.8 TB (not to mention a huge amount of computation time). This obstacle seems to have a simple solution: Let's just wait 50 years for the technology to catch up and then solve it on our high-tech mobile phones.

But instead of waiting on their lazy backs, physicists have taken a closer look at the characteristics of turbulence on a more abstract level, hoping to get a deeper understanding of the involved phenomena. Turbulent flows are not at all completely chaotic, but exhibit structures that develop and interact in a complex manner. The first scientific attempt to describe turbulence on a phenomenological level was made by Kolmogorov in 1941, which resulted in his now famous K41 theory (briefly presented in section 5.1.2). Advanced

and more refined theories followed and addressed K41's shortcomings, most notably the problem of *intermittency* (section 5.1.3). All these approaches gave insight through the study of statistical properties of turbulent flows and have helped to *understand* turbulence instead of *brute-forcing* solutions to single problems. Thus the "problem of turbulence" is reconstituted:

Even if one *could* simulate a turbulent flow at arbitrary precision, one would still not understand the processes, the interactions and structures that are characteristic for turbulence, on a deeper level. The problem of turbulence would be solved for the engineer, but not for the physicist (so, sadly, waiting 50 years is not an option).

5.1 Phenomenological description

Most of the theory of turbulence is more or less restricted to Navier-Stokes turbulence. Recently, encouraged by fusion research, instabilities and containment problems, but also motivated by astrophysical problems, turbulence for magnetohydrodynamics (MHD) is an actively research topic. Burger's turbulence is of less general interest, as it lacks the most prominent feature of turbulent flows: chaos. It may still be studied as academic problem or used as numerical and mathematical benchmark. Of course, no theoretical background is developed for Euler-Burgers' turbulence. Since the equation resembles Navier-Stokes in most aspects, many results may be carried over from the already known theories of Navier-Stokes turbulence. I will, therefore, concentrate on presenting models for Navier-Stokes turbulence, referencing to the Euler-Burgers' case whenever necessary.

Up to today, no complete theory of turbulence derived directly from the governing hydrodynamical model is known for the Navier-Stokes equation, which is quite impressive, considering the age of the equation. Nevertheless, advancement is made with phenomenological methods, i.e. heuristical arguments and the analysis of dimensions and dependencies. Most of the statistical conclusions concern a range of scales between the large scale of boundaries or forcing and the small scale where dissipation takes effect. This intermediate scale, the so called **inertial scale**, is of highest importance to turbulence.

Range of scales and the energy cascade

Considering any turbulent, driven flow, energy is inserted into the system by an external force $\mathbf{f}$. In every case of three-dimensional turbulence considered here, the forcing can be assumed to take place on a large scale l_0. This scale is called the **integral scale**. As already pointed out in sections 2.2.3 and 2.4.1, the viscous term of the model equation is responsible for energy dissipation for both Navier-Stokes and Euler-Burgers'. The scale η in which viscosity notably influences the flow is called the **dissipative scale** or *Kolmogorov scale*.

The **inertial range** lies in between those two limiting boundaries. No energy is inserted or depletes within this regime and all interaction is governed by the nonlinear term. As both information about the molecular-level dissipation and the large driving forces and geometry are without influence, this range exhibits universal statistics. This is why most results of turbulence research focus on the inertial range.

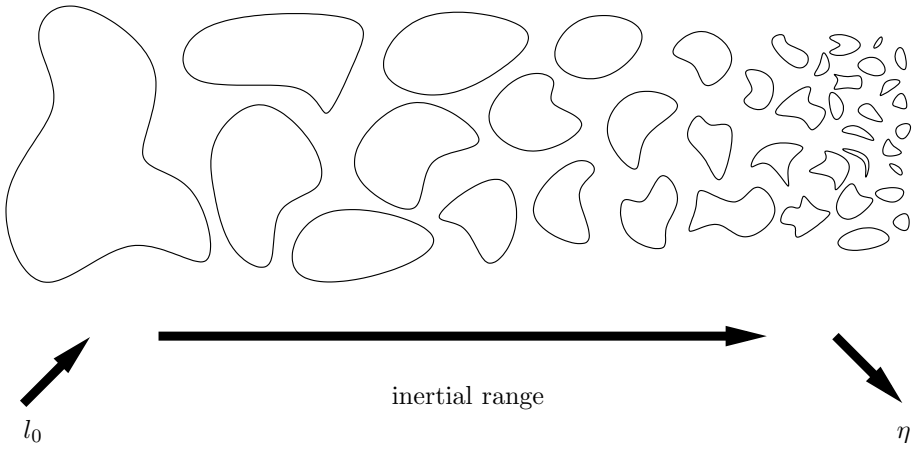

Figure 5.1: The Richardson cascade. Energy is inserted into the system at the integral scale l_0. Repeated breakup of the dissipative structures lead to their downsizing, until they reach the Kolmogorov scale η to be dissipated

Since the energy is created at the largest, but dissipates at very small scales, there has to be an effect of the nonlinearity that transports the energy down to smaller scales. For the Navier-Stokes equation, the model of this process is called the **Richardson cascade** (named after Richardson [1922]). Large eddies break up into smaller ones, which after some time meet the same fate and break up again, until they dissolve at the small scale of viscosity (sketched in figure 5.1).

In Euler-Burgers' equation the nonlinearity also leaves the total energy untouched, the scales and the energy cascade are the same, with the only difference that the governing structures that break up into ever smaller fractions are not vortices.

Free-falling turbulence

When speaking of **stationary turbulence**, one does not mean a flow with time independent velocity field, but instead a flow where the inserted energy equals the dissipated energy. For such situations, a quasi-steady and statistically time-independent flow evolves.

In contrast, when not applying any external forces, the total kinetic energy available with the initial conditions can not be exceeded at any later time. The transport process that leads to the Richardson cascade, nevertheless, affects the flow. This is called **free-falling turbulence**.

With initial conditions varying only over large scales l_0 (as the Orszag-Tang-like initial conditions presented in section 4.4.1) the large structures break apart and form smaller structures at different timescales. At a time t_E, when the first structures appear at the dissipation scale, one may speak of fully developed turbulence. This time t_E can be identified as the maximum of enstrophy

$$\Omega = \int (\nabla \times \mathbf{u}(\mathbf{x}))^2 \mathrm{d}\mathbf{x}. \tag{5.2}$$

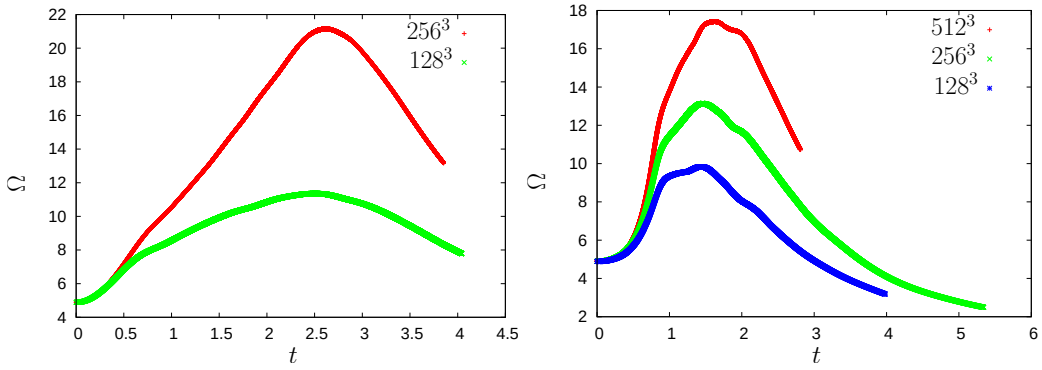

Figure 5.2: Plot of the enstrophy Ω against time for different hydrodynamical models at different resolutions. **Left:** Navier-Stokes equation, runs `NS1` and `NS2`. **Right:** Euler-Burgers' equation, runs `EB1`, `EB2` and `EB3` (see section 5.2 for details on the runs). All statistical evaluation is performed at the time of maximal enstrophy t_E. For Euler-Burgers' equation the dynamic evolution is notably faster.

Figure 5.2 shows the evolution of enstrophy against time for numerical simulations of the Navier-Stokes equation (left) and the Euler-Burgers' equation (right) at different resolutions starting with the Orszag-Tang-like initial conditions. The times t_E for Euler-Burgers' are decisively smaller in comparison, which hints at faster dynamics of this hydrodynamical model: The energy arrives at the smallest scales much earlier. It will be shown that the evolution of Burgers' equation is even faster. Thus the temporal development of the dissipative structures is another aspect in which Euler-Burgers' lies in between the other two hydrodynamical models.

5.1.1 Statistical tools and quantities

As already pointed out, studying turbulence is, in most cases, equivalent to studying the statistics of the flow. Several quantities are of importance and are briefly introduced here.

The statistics can be obtained in two complementary ways: In the Eulerian point of view all quantities are measured and compared at absolute positions in the laboratory frame of reference. Lately, the Lagrangian perspective of tracing statistical quantities while following the flow has gained more and more attention. This is realized by inserting tracer particles, which are advected by the flow. Although this possibility is already implemented in *racoon II* (see Schwarz [2007]), for reasons of simplicity I will restrict myself to the Eulerian view.

Energy spectra

The existence of the inertial range and the Richardson cascade give reasons to take a closer look at the scales that the kinetic energy is distributed on.

The fluid velocity at a point, $\mathbf{u}(\mathbf{x})$, with the Fourier series

$$\mathbf{u}(\mathbf{x}) = \sum_{\mathbf{k}} \hat{\mathbf{u}}_k e^{i\mathbf{k}\cdot\mathbf{x}}$$

can be divided at a scale $l = K^{-1}$ via

$$\mathbf{u}(\mathbf{x}) = \sum_{\mathbf{k}\leq K} \hat{\mathbf{u}}_{\mathbf{k}} e^{i\mathbf{k}\cdot\mathbf{x}} + \sum_{\mathbf{k}>K} \hat{\mathbf{u}}_{\mathbf{k}} e^{i\mathbf{k}\cdot\mathbf{x}} = \mathbf{u}_K^<(\mathbf{x}) + \mathbf{u}_K^>(\mathbf{x}).$$

The cumulative energy spectrum

$$\mathcal{E}(k) = \frac{1}{2} \int_\Omega \left(\mathbf{u}_k^<(\mathbf{x})\right)^2 \mathrm{d}\mathbf{x}$$

describes the kinetic energy at all scales larger or equal to $l = k^{-1}$. Now the **energy spectrum** is defined as

$$E(k) = \frac{\mathrm{d}}{\mathrm{d}k}\mathcal{E}(k)$$

and consequently contains the energy in the shell between k and $k + dk$.

As an example, consider Burgers' equation. The most prominent features are shocks, which may be approximated as discontinuities even for small viscosity . The Fourier transformation of discontinuities provides a k^{-2}-spectrum (as pointed out in Gotoh and Kraichnan [1992]):

$$E(k) \propto k^{-2}. \tag{5.3}$$

For the other hydrodynamical models, the according energy spectra are derived later in the course of Kolmogorov's theory of turbulence.

Structure functions

The spatial average of a velocity increment

$$\delta\mathbf{v}(\mathbf{x}, \mathbf{l}) = \mathbf{v}(\mathbf{x}) - \mathbf{v}(\mathbf{x} + \mathbf{l})$$

to the p$^{\text{th}}$ power is called **structure function** $S_p(\mathbf{l})$ of order p:

$$S_p(\mathbf{l}) = \langle(\delta\mathbf{v}(\mathbf{x}, \mathbf{l}))^p\rangle_{\mathbf{x}} = \int_\Omega (\delta\mathbf{v}(\mathbf{x}, \mathbf{l}))^p \,\mathrm{d}\mathbf{x}.$$

For the isotropic case, the dependence on $\mathbf{l}$ is replaced by its norm l. With increasing order p, the structure function pronounces more "extreme" features like shocks or discontinuities. Therefore, It is an indispensable tool in understanding the nature of turbulence.

As a more recent result by Benzi et al. [1993], further supported by Briscolini et al. [1994], the idea of **extended self-similarity** (ESS) even increases the applicability of structure functions, extending the inertial range significantly. For the details of applying ESS to my results, see the sections 5.2.1 for Burgers' equation and 5.2.2 for Euler-Burgers' equation.

5.1.2 K41

As mentioned in the introduction of this chapter, Kolmogorov (in Kolmogorov [1941a] and Kolmogorov [1941b]) was the first to approach the problem of turbulence quantitatively. I will in the following briefly outline his theory, a more detailed description can be found in Frisch [1995].

Three assumptions constitute the foundation of K41:

1) Hypothesis of local isotropy: *At scales l well below the integral scale, $l \ll l_0$, a turbulent flow is statistically isotropic for sufficiently high Reynolds numbers.*

Forcing or boundaries typically introduce flow anisotropy. At scales small enough compared to the integral scale all information about these large dynamics is lost. The small-scale motions of the fluid can, therefore, be considered *universal*. Another way to express this hypothesis is to say that the (rotational and translational) symmetries of the underlying equation are restored in a statistical sense.

2) First hypothesis of similarity: *At sufficiently small scales $l \ll l_0$ and high Reynolds numbers, the statistics of the flow are universal and determined solely by the viscosity ν and the energy dissipation rate ε.*

The *universality* of the flow can be translated into a *self-similarity* at scales below the integral length. This can be expressed in terms when considering spatial averages of velocity increments $\delta_l \mathbf{u} = \mathbf{u}(\mathbf{x}) - \mathbf{u}(\mathbf{x} + \mathbf{l})$. For a self-similar flow, they should obey

$$\delta_{\lambda l}\mathbf{u} = \lambda^h \delta_l \mathbf{u}, \tag{5.4}$$

with $\lambda \in \mathbb{R}$ and $h \in \mathbb{R}$ being independent of l. When rescaling $l \to \lambda l$ and $\delta_l \mathbf{u} \to \lambda^h \delta_l \mathbf{u}$, the time has to scale like $t \to \lambda^{1-h} t$ and the energy dissipation rate like $\varepsilon \to \lambda^{3h-1}$. On the other hand, the energy dissipation rate should no depend on the scale l. This provides

$$h = \frac{1}{3}, \tag{5.5}$$

which is of fundamental importance to results later on. This result surprisingly is also deducible in a more stringent way starting from the Navier-Stokes equation and applying the Kármán-Howarth-Monin relation (see Frisch [1995]). The assumption of self-similarity itself is, nevertheless, under dispute. This topic will be re-addressed in the section about intermittency (section 5.1.3).

The independence of any other quantity than ν and ε allows an estimate of the *dissipative scale* η via dimensional arguments. As a small scale property of the flow it should hold that $\eta = \eta(\nu, \varepsilon)$, and also η should be of dimension L. The only combination to achieve this is

$$\eta = \left(\frac{\nu^3}{\varepsilon}\right)^{\frac{1}{4}}. \tag{5.6}$$

3) Second hypothesis of similarity: *In the inertial range $l \ll l_0$ and at high Reynolds numbers, the statistics of the flow have an universal form and depend only on the energy dissipation rate ε.*

This hypothesis basically states the existence of the inertial range and further defines its independence of all quantities besides ε. Kolmogorov postulates that even for vanishing viscosity the energy dissipation should stay finite (non-zero). As a side note, possible singularities in the flow could explain energy dissipation in inviscid flows. Inviscid Burgers' equation is a good example of how discontinuities can act as dissipative structures even without viscosity.

Structure functions prove to be a reliable benchmark for testing the K41 theory. The prediction of the scaling exponent h in (5.5) directly influences the scaling properties of the structure functions of order p:

$$S_p(l) \propto l^{\zeta_p} \qquad \text{with} \qquad \zeta_p = \frac{p}{3} \tag{5.7}$$

The scaling properties of the second-order structure function $S_2(l)$ has consequences for the energy spectrum. In detail, as pointed out by Frisch [1995], it holds that

$$E(k) \propto k^{-n} \qquad \text{for} \qquad S_2(l) \propto l^{n-1}, \tag{5.8}$$

and with that, K41 predicts

$$E(k) \propto k^{-\frac{5}{3}} \tag{5.9}$$

within the inertial range. Experimental as well as numerical data supports this prediction for Navier-Stokes equation (see, for example, Homann [2006]) and as shown in section 5.2.2, numerical simulation weakly verifies this result for the Euler-Burgers equation, too.

The only exact result of the K41 theory, derived directly from Navier-Stokes equation, is the $\frac{4}{5}$-*law*. Applying the Kármán-Howarth-Monin relation, after some calculation one obtains (see Frisch [1995]) that

$$S_3(l) = \frac{4}{5}\varepsilon l \tag{5.10}$$

is fulfilled by the third-order structure function. As this result is strictly deducible, it can be used as a benchmark for turbulence theories. Obviously with $\zeta_p = \frac{p}{3}$, K41 complies with this result. But the linear dependence of ζ_p on p proves to be wrong for higher orders, as both numerical and experimental data indicate. This discrepancy is attributed to the phenomenon of *intermittency*.

5.1.3 Intermittency

Kolmogorov assumes linear scaling behavior of the velocity structure functions as well as the scale independence of the energy dissipation rate ε. Quite to the contrary, simulations reveal a strong locality and show its dependence of the scale l. In his *refined self-similarity*

hypothesis (see Kolmogorov [1962]) Kolmogorov introduced scale-dependent energy dissipation rates ε_l. Velocity fluctuations may only depend on the scale l and the energy dissipation rate. This allows to deduce

$$\langle \delta_l \mathbf{u} \rangle \propto (\varepsilon_l l)^{\frac{1}{3}} \tag{5.11}$$

via dimensional analysis.

Central to the theory of Kolmogorov was the assumption of space filling self-similarity of the turbulent flow within the inertial range. Experimental data seems to indicate a violation of this assumption. The same is true for the time-domain: high amplitude events are not evenly distributed but occur at discrete and confined points in time.

Both these effects are clearly visible in the behavior of the high-order structure functions $S_p(l)$. To match the measurements it was necessary to derive other scaling laws

$$S_p(l) \propto l^{\zeta_p} \qquad \text{and} \qquad \langle \varepsilon_l^p \rangle \propto l^{\tau_p} \tag{5.12}$$

for the velocity increments and the energy dissipation rate that are both explicable and agree with the measured data. Several attempts have been made to account for intermittency, which I will mention very briefly. Details of the derivations can be found in Frisch [1995].

Models for intermittency

In 1962, Kolmogorov together with Obukhov presented the first model of intermittency. They allow different energy dissipation rates ε_l for different regions and for different scales and end up with

$$\zeta_p = \frac{p}{3} - \mu \frac{p(p-3)}{18} \tag{5.13}$$

for the scaling exponent, μ being the *intermittency parameter*, which can be estimated to $\mu \simeq 0.2$. The *Obukhov-Kolmogorov model* fails for orders larger than $p = 10$.

The *β-model* considers the violation of the space filling self-similarity assumption by introducing a parameter β, that describes the decreasing size of eddies between two generations. Further taking into account the dimension D of the dissipative structures, the β-model predicts

$$\zeta_p = \frac{p}{3} + (3 - D)\left(1 - \frac{p}{3}\right) \tag{5.14}$$

for the scaling exponents. As opposed to experimental results, the β-model still features linear scaling behavior.

Resorting to the fractal nature of intermittent flows, the *bifractal model* and later on the *multifractal model* consider two or multiple sets of fractal (Hausdorff) dimension with differing scaling exponents. A model in the spirit of the multifractal description is the model of She and Lévêque [1994]. Because of its success in describing the numerical data, it will be presented in more detail in the following section.

The She-Lévêque model

The basic assumptions of the *She-Lévêque model* emanate from the refined self-similarity hypothesis of Kolmogorov. Taking its scaling behavior for the velocity increments (5.11) in combination with l-dependence of the structure functions and the energy dissipation rate (5.12) provides

$$\zeta_p = \frac{p}{3} + \tau_{\frac{p}{3}}. \tag{5.15}$$

First they introduce the intensity of the p^{th} order dissipation structures

$$\varepsilon_l^{(p)} = \frac{\langle \varepsilon_l^{p+1} \rangle}{\langle \varepsilon_l^{p} \rangle}. \tag{5.16}$$

To handle all hydrodynamical models in parallel, I assume a scale dependent timescale of

$$t_l \propto l^k \tag{5.17}$$

in contrast to She and Lévêque (who set $k = \frac{2}{3}$ for Navier-Stokes). The most singular structures for a scale l are captured in the limit $p \to \infty$. They are responsible for the anomalous scaling law. One may imagine $\varepsilon_l^{(\infty)}$ as the most intermittent structures of the flow. Estimating

$$\varepsilon_l^{(\infty)} \propto \frac{\delta E^{\infty}}{t_l} \tag{5.18}$$

with the timescale introduced in (5.17), one obtains

$$\varepsilon_l^{(\infty)} \propto l^{-k}. \tag{5.19}$$

In the limit $p \to \infty$ this provides $\tau_{p+1} - \tau_p \propto -k$, which results in

$$\tau_p = -kp + C_0 + f(p) \qquad \text{with } f(\infty) = 0 \tag{5.20}$$

when regarding the difference above in its infinitesimal limit. Following the spirit of the above mentioned models of intermittency, She and Lévêque interpret the constant C_0 as the Co-dimension of the most dissipative structures.

For smaller p it is assumed that each $\varepsilon_l^{(p+1)}$ is an interpolation between $\varepsilon_l^{(p)}$ and the limiting case $\varepsilon_l^{(\infty)}$:

$$\varepsilon_l^{(p+1)} \propto \left(\varepsilon_l^{(p)}\right)^{\beta} \left(\varepsilon_l^{(\infty)}\right)^{1-\beta} \qquad \text{for } \beta \in (0,1). \tag{5.21}$$

Now, just inserting the definitions (5.16) and (5.20) into (5.21), after some computation, a relation for $f(p)$ is obtained, which can be solved to

$$f(p) = C_0 \left(\frac{C_0 - k}{C_0}\right)^p. \tag{5.22}$$

A detailed derivation of this step is included in the Appendix in section C. The final result is now easily obtained, when the above function $f(p)$ is inserted into (5.20) and combined with (5.15):

$$\zeta_p = \frac{(1-k)p}{3} + C_0 \left(1 - \left(\frac{C_0 - k}{C_0} \right)^{\frac{p}{3}} \right). \tag{5.23}$$

This formula will be addressed as the *generalized She-Lévêque model*.

In the following section, numerical data of all three hydrodynamical models is tested against the generalized predictions of She and Lévêque. The only thing left to do is insert the correct time-scaling exponent k and the Co-dimension of the most intermittent structures C_0.

5.2 Results for different hydrodynamical models

The aim of this section is to analyze and compare turbulent flows for Burgers', Euler-Burgers' and Navier-Stokes equation. The tools and theoretical background that will be used have been described in the previous section.

First, Burgers' turbulence will be treated very briefly in section 5.2.1. Here the expected behavior of the energy spectrum and the scaling exponents will be shown and useful tools and models like ESS or the generalized She-Lévêque model will be applied for the first time. This also affords the opportunity to validate the functionality of the numerical simulations and the diagnostics.

As there already exist numerous (elaborate and detailed) compositions for Navier-Stokes turbulence, I will put emphasis on the Euler-Burgers' equation instead and restrain myself to mere comparisons to Navier-Stokes. This will be done in section 5.2.2. Here the applicability of the theories presented above to the new equation will be shown. This may be interpreted as evidence for the close connection between the Euler-Burgers' equation and the Navier-Stokes equation.

5.2.1 Burgers' turbulence

The evolution of free-falling Burgers' turbulence is unique in several ways. Its tendency to form shocks in rather short time and the dissipative effect of these structures lead to the fastest dynamical behavior of all three considered hydrodynamical models. In the direct comparison of figure 5.3 (left), the L^2-norm of the kinetic energy decays twice as fast as for the turbulent Euler-Burgers' flow. This is caused by the higher viscosity that was needed to keep steeper gradients at the discontinuities under control.

As already mentioned, the optimal time to analyze the statistical properties of the flow is at $t = t_E$, when the enstrophy reaches its maximum. For Burgers' equation this is the moment when most of the shocks are developed and start to decay under the effect of viscosity. Figure 5.3 (right) compares t_E for different numerical resolution. As consequence to the decreased viscosity, the maximum enstrophy increases with the number of mesh points.

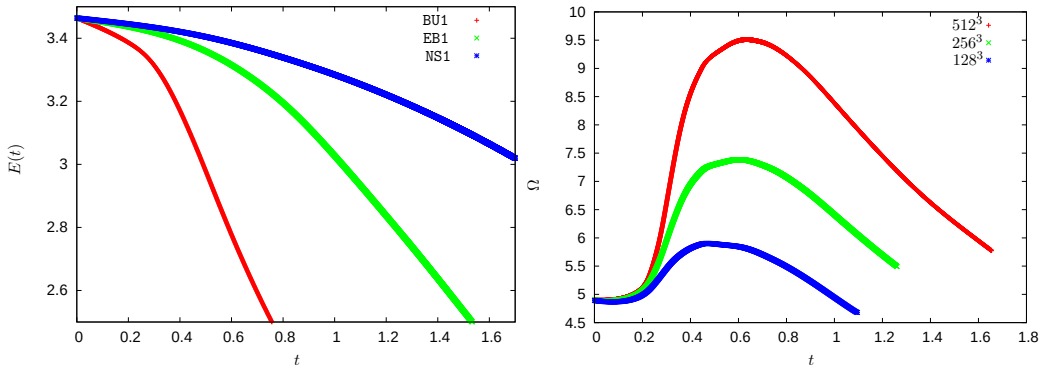

Figure 5.3: Left: Comparison of the L^2-norm of the kinetic energy for Navier-Stokes, Burgers' and Euler-Burgers' equation. The steep discontinuities of a Burgers' flow explain the fast energy dissipation. **Right:** Evolution of free-falling turbulence for Burgers' equation using different resolutions. The turbulent flow is fully developed at $t = t_E$, when the enstrophy Ω reaches its maximum.

The runs

Three final runs with resolutions up to 512^3 were performed for Burgers' equation. The initial velocity field $\mathbf{u}_0$ is given by the Orszag-Tang-like initial conditions (section 4.4.1). Since the turbulent flow is isotropic and homogeneous, the staggered grid formulation (section 4.3) is used. This also ensures the comparability to simulations of the other hydrodynamical models.

Run	N	ν	t_E	max($\|\Omega\|$)	max($\|\boldsymbol{\omega}\|$)
BU1	128^3	0.0241	0.461	5.76	100.4
BU2	256^3	0.015	0.603	7.38	195.4
BU3	512^3	0.009	0.634	9.51	349.9

Table 5.1: Overview of all three simulations of Burgers' equation. Listed are the resolution N, viscosity ν, time of fully developed turbulence t_E, the maximum enstrophy max($|\Omega|$) and the maximum vorticity max($|\boldsymbol{\omega}|$).

Table 5.1 lists all important parameters of the runs. Higher resolution allows for more pronounced singular structures, which can be achieved with lower viscosity. Let ν be the viscosity for a simulation, and $\nu' = \mu\nu$ be the viscosity for a similar simulation with doubled resolution. The factor μ can be obtained from K41 with the following consideration: Doubled resolution means the dissipation length η is halved. Since the energy dissipation rate ε is intended to stay constant, one obtains with the help of equation (5.6)

$$\mu = 2^{-\frac{4}{3}} \simeq 0.397. \tag{5.24}$$

For Burgers equation, a factor of about $\mu = 0.6$ was used, since the discontinuities of the velocity field turned out to be numerically unstable for smaller factors. For Navier-Stokes equation, where K41 fully applies, the theoretical factor of $\mu \simeq 0.4$ proved to be stable.

Energy spectrum

The strong shocks of Burgers equation have a large impact on the energy spectrum. As pointed out in equation (5.3), the dependence on k should behave like k^{-2}. Figure 5.4 indicates that the numerical simulation confirms this.

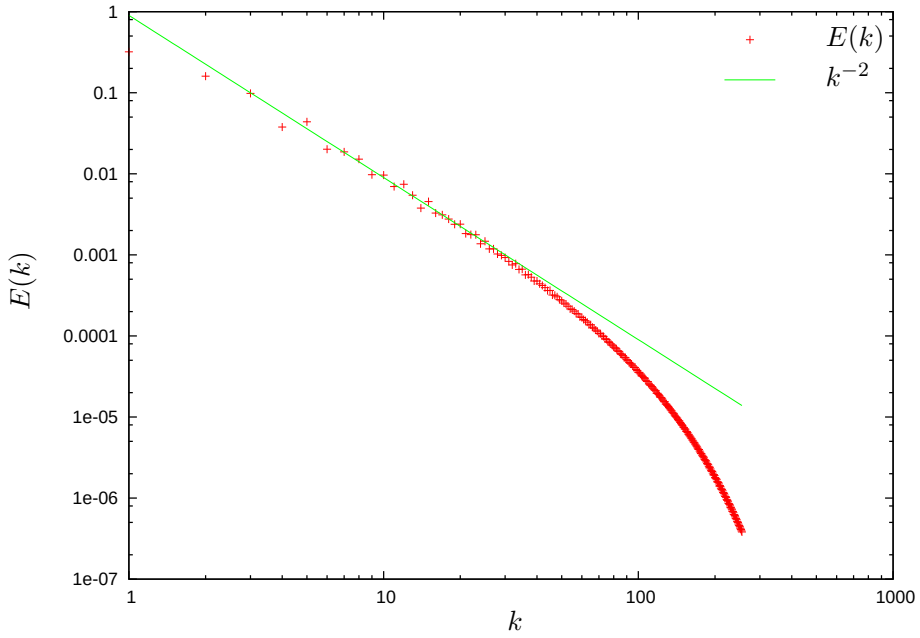

Figure 5.4: Log-log plot of the energy spectrum for Burgers' equation. In the inertial range, the theoretical slope of -2 is reached. Data is taken from run BU3

Due to the high viscosity the inertial range is small but still prominent for the highest resolution. For the scaling exponents of the structure functions, the small inertial range proves to be a problem that can be solved with the use of ESS.

Scaling exponents

Burgers' equation provides the first opportunity to demonstrate the validity of the generalized She-Lévêque model introduced in section 5.1.3. The typical time t_l for the evolution of discontinuities for turbulent Burgers' flows scales linear with l, which accounts for $k = 1$. As the shocks traveling through the domain are two-dimensional we furthermore obtain $C_0 = 1$. Inserting this into equation (5.23) leads to

$$\zeta_p = 1. \tag{5.25}$$

Since parts of the velocity field are continuous, for $p < 1$ the smoother regions of the velocity field are pronounced. This would equal a scaling exponent of $\zeta_p = p$ for these orders. Since this result is smaller than $\zeta_p = 1$, it is dominant for $p < 1$. This results in

an expected scaling behavior of

$$\zeta_p = \begin{cases} p & \text{for } p < 1 \\ 1 & \text{for } p \geq 1 \end{cases} \tag{5.26}$$

for Burgers' equation.

p	1	2	4	5	6	7
α_p	0.70	0.95	1.00	1.00	0.98	1.00
ζ_p	1.00	1.00	1.00	1.00	1.00	1.00

Table 5.2: Scaling exponents ζ_p for Burgers' equation. The α_p measured with ESS are compared to the ζ_p predicted by the generalized She-Lévêque model.

Theory predicts $S_3(l) \propto l$. For Navier-Stokes, this is a direct consequence of the exact $\frac{3}{5}$-law and a result of the generalized She-Lévêque model for Burgers equation, as just derived. Analysis of simulation data (see e.g. Benzi et al. [1993]) showed that the inertial range can be enlarged when plotting $S_p(l)$ against $S_3(l)$ (instead of $S_p(l)$ against l). It should hold that

$$S_p(l) \propto S_3(l)^{\alpha_p} \tag{5.27}$$

and ideally $\alpha_p = \zeta_p$. Obtaining the scaling exponents with this method is called *extended self-similarity* (ESS).

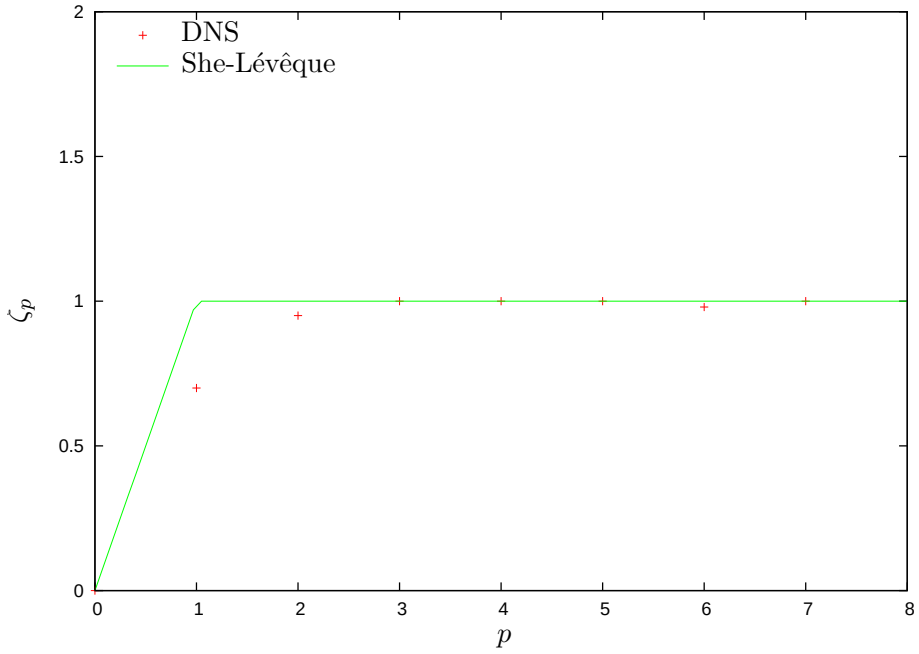

Figure 5.5: Scaling exponents ζ_p for Burgers equation. The line represents the predictions of the She-Lévêque model, crosses denote the measurements of the direct numerical simulation of run BU3 at $t = t_E$.

Table 5.2 shows the measurements of the run `BU3`. Here, α_p is the data obtained via ESS and ζ_p is the prediction of equation (5.26). The visualization of this result is shown in figure 5.5. The numerical simulation of Burgers' equation supports the generalized She-Lévêque model very well. Especially for high order of p ($p > 3$) the scaling exponent agrees with the prediction, yet smears out for smaller p.

5.2.2 Euler-Burgers' turbulence

The Euler-Burgers' model was introduced to analytically bridge the gap between Euler/Navier-Stokes equation and Burgers' equation. The following section will show that Euler-Burgers' equation lies in between the other two model also from the perspective of turbulence.

The equation allows for shocks to develop, since no incompressibility condition is stated. Nevertheless, as shown in section 2.4.1, energy decays solely via the dissipative term. Because of this, the hypotheses of Kolmogorov may be adapted to Euler-Burgers' equation. The Richardson cascade as well as the properties of the energy spectrum and the scaling behavior of structure functions should agree with the conclusions of Kolmogorov and the generalized She-Lévêque model. On the other hand, the structures that evolve seem to be significantly different from the vortex filaments known from Navier-Stokes.

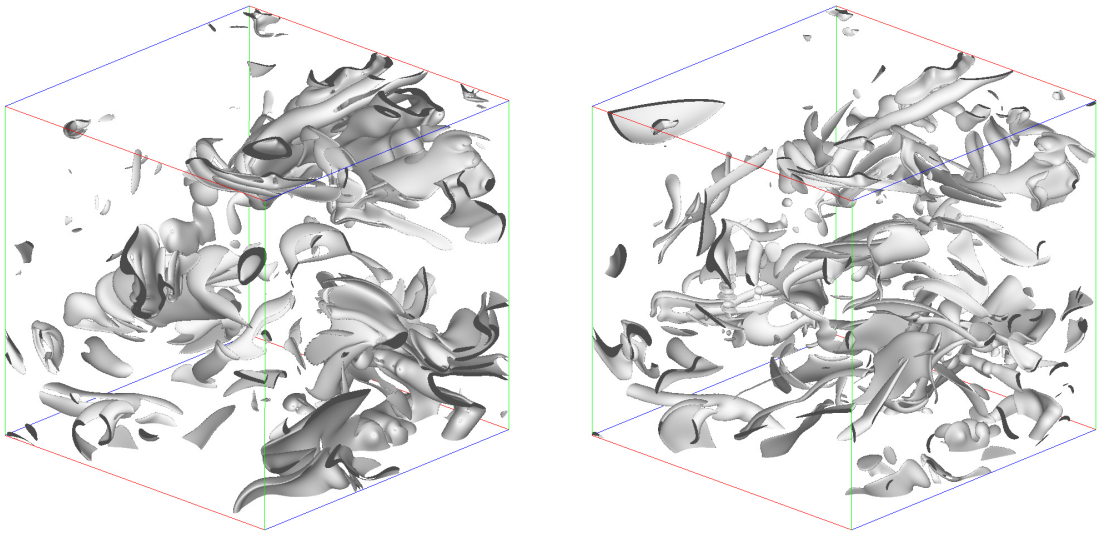

Figure 5.6: Isosurfaces of the dissipative structures for Euler-Burgers' equation. **Left:** Isosurface of $|\boldsymbol{\omega}|$. **Right:** Isosurface of $\nabla \cdot \mathbf{u}$. Data taken from run `EB3`.

Figure 5.6 shows the most dissipative structures of a turbulent Euler-Burgers' flow at $t = t_E$. On the left side, the norm of the vorticity visualizes the structures that correspond to the vortex tubes of Navier-Stokes. The isosurface pictures two-dimensional folded vortex sheets. The right side illustrates regions of compression and expansion in the flow. Areas of large divergence often seem to be located at the edge of the vortex

sheets even though some regions are compressed without exhibiting high vorticity. The typical two-dimensional discontinuities known from Burgers' equation are not observed.

The runs

For the numerical simulation again the staggered grid formulation was applied. The Orszag-Tang-like initial conditions for $\mathbf{u}_0$ are used and the turbulence is free-falling. Euler-Burgers' equation was simulated up to a resolution of 512^3 grid points. The reference simulations of Navier-Stokes equation were conducted just to a resolution of 256^3.

Run	N	ν	t_E	max($\|\Omega\|$)	max($\|\boldsymbol{\omega}\|$)
EB1	128^3	0.01	1.438	9.84	187.1
EB2	256^3	0.006	1.459	13.14	381.7
EB3	512^3	0.0036	1.624	17.42	768.6
NS1	128^3	0.007	2.502	11.36	116.2
NS2	256^3	0.00278	2.616	21.15	251.0

Table 5.3: Overview of all three simulations of Euler-Burgers' equation and the simulations of Navier-Stokes for comparison. Listed are the resolution N, viscosity ν, time of fully developed turbulence t_E, the maximum enstrophy max($|\Omega|$) and the maximum vorticity max($|\boldsymbol{\omega}|$).

Equal to Burgers' equation, the viscosity was scaled to higher resolutions with $\mu = 0.6$. For Navier-Stokes turbulence, the theoretical value of $\mu = 0.397$ proved to be stable. All parameters are listed in table 5.3.

Energy spectrum

K41 suggest an energy spectrum like $E(k) \propto k^{-\frac{5}{3}}$. As we have seen, the generalized She-Lévêque model corrects the scaling exponents and, thus, influences the energy spectrum as well. Since $S_2(l) \propto l^{0.74}$ an insignificant correction of

$$E(k) \propto k^{-\frac{5}{3}-0.08} \tag{5.28}$$

follows via (5.8). With the simulation, as shown in figure 5.7, this prediction is verified for the velocity field $\mathbf{u}$, even if the inertial range is very narrow. Despite being a compressible field, no discontinuities arise, as these would lead to the k^{-2}-spectrum known from Burgers' equation. This is the first concrete evidence that the traditional models for Navier-Stokes turbulence may be adopted to Euler-Burgers'. It also shows that Euler-Burgers' turbulence statistically lies close to Navier-Stokes turbulence.

Scaling exponents

The comparison between theory and measurements of scaling exponents ζ_p is a substantial test for the validity of the generalized She-Lévêque model. The timescale t_l for Euler-Burgers' equation is estimated according to K41 as $t_l \propto l^{\frac{2}{3}}$. As studied in section 2.4.1,

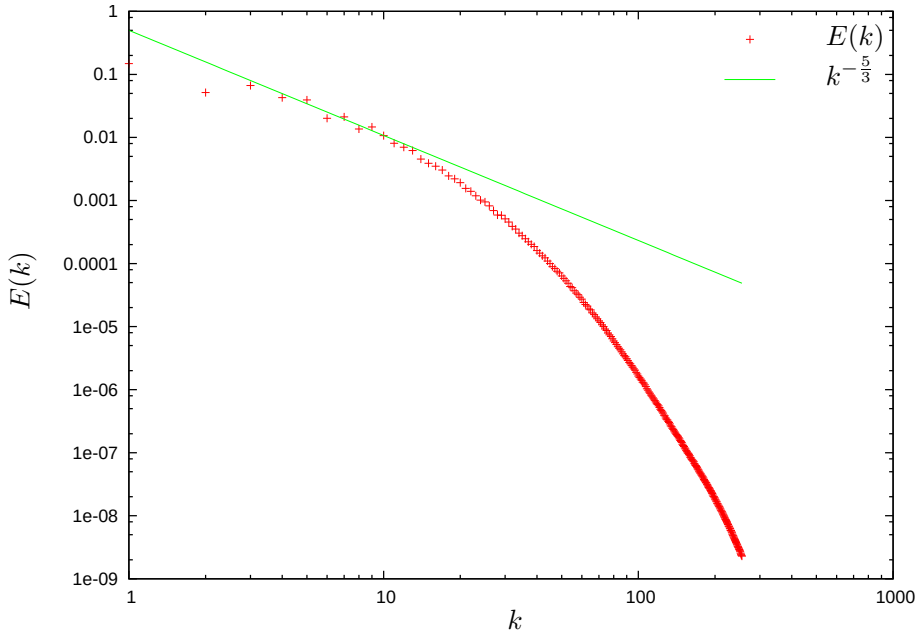

Figure 5.7: Energy spectrum of a turbulent Euler-Burgers' flow with 512^3 grid points. Free falling turbulence and the high viscosity shorten the inertial range, allowing just a weak verification of the $k^{-\frac{5}{3}}$ spectrum postulated by K41.

the structures of a turbulent flow are two-dimensional and suggest $C_0 = 1$. Thus,

$$\zeta_p = \frac{p}{9} + \left(1 - \left(\frac{1}{3}\right)^{\frac{p}{3}}\right) \tag{5.29}$$

is the prediction for the scaling exponents proposed by the generalized She-Lévêque model.

p	1	2	4	5	6	7
$\alpha_p(\mathbf{u})$	0.42	0.75	1.23	1.37	1.51	1.63
$\alpha_p(\mathrm{P}\mathbf{u})$	0.4	0.73	1.22	1.39	1.55	1.69
ζ_p	0.418	0.751	1.213	1.395	1.556	1.701

Table 5.4: Scaling exponents ζ_p for Euler-Burgers' equation. The α_p for $\mathbf{u}$ and $\mathrm{P}\mathbf{u}$ measured with ESS are compared to the ζ_p predicted by the generalized She-Lévêque model.

Table 5.4 features the results of the simulation `EB3` measured via ESS at $t = t_E$. The scaling exponents for both the compressible and the solenoidal velocity field have been determined.

As can be seen in figure 5.8 the numerical data agrees very well with the prediction of the generalized She-Lévêque model. The compressible field is slightly more intermittent, which is plausible since only here minor shocks may appear. As already deduced from

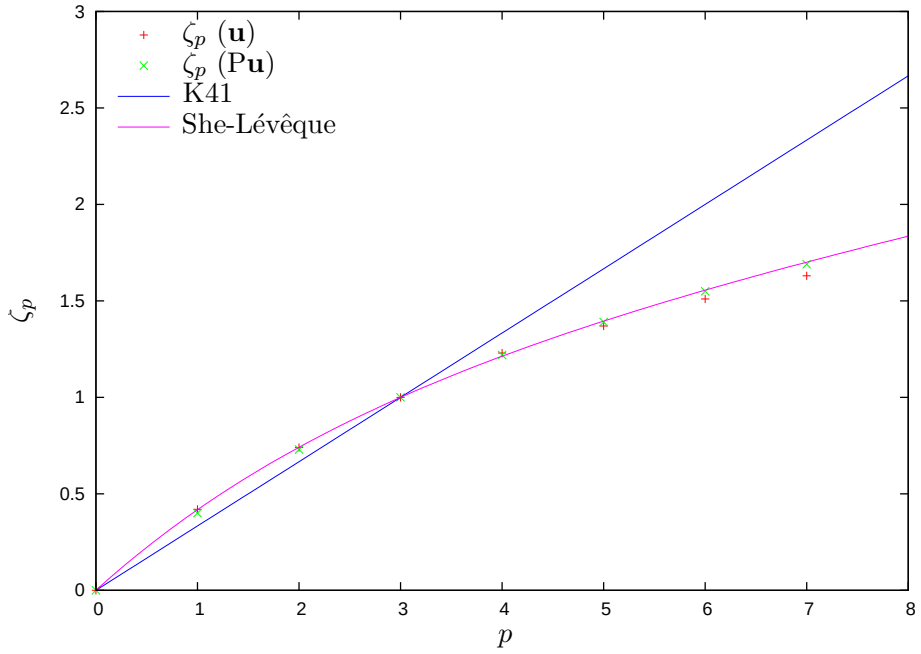

Figure 5.8: Scaling exponents ζ_p for Euler-Burgers' equation. The lines represents the predictions of K41 and the generalized She-Lévêque model, crosses denote the measurements of the direct numerical simulation of run EB3 at $t = t_E$ for the compressible velocity field $\mathbf{u}$ and its solenoidal projection $\mathrm{P}\mathbf{u}$. As expected, the compressible field is slightly more intermittent due to discontinuities.

the energy spectrum, these shocks cannot be very pronounced. The scaling exponents, therefore, do not differ much from the values suggested by theory. The solenoidal field is consistent with theory from low orders of p up to the highest order that was measured.

5.3 Conclusion

It was shown that Euler-Burgers' equation develops "true" turbulence in a sense that it exhibits quasi-chaotic behavior, an energy cascade from big to small scales and the formation of dissipative structures. The theory for Navier-Stokes, adjusted just in terms of the geometry of the flow, agrees very well with the results of the numerical simulation of Euler-Burgers' equation. Even though the dissipative structures look quite different, the same statistical models may be applied. Euler-Burgers' equation, therefore, proves to be an interesting hydrodynamical model in understanding turbulence in general.

Chapter 6

Singularities

While the problem of the existence, uniqueness and smoothness of the solutions was settled for Euler-Burgers' equation in chapter 3, as already mentioned no such results exist yet for the Navier-Stokes or Euler equation. This problem is recognized by the Clay Mathematics Institute as one of the six remaining unsolved Millennium Problems. It is believed that its solution will require new methods and tools in the theory of partial differential equations.

In the following section, I will briefly present the mathematical advancement made on this field, regarding both Navier-Stokes and Euler equation. As it turns out, numerical simulations can help focusing the view onto the right estimates or hint at new perspectives to solve the problem. An overview of the computational Euler/Navier-Stokes history is given in section 6.2.1. In the last section (section 6.2.2) I will present my results made using the vorticity formulation to probe the colliding vortices of the Kida-Pelz initial conditions. This state-of-the-art simulation goes up to an effective resolution of 4096^3 and gives helpful information about the influence of the resolution on the question of finite time singularities in Euler flows.

6.1 Mathematical preliminaries

For the two-dimensional Navier-Stokes equation, existence, uniqueness and smoothness of solutions is known for quite a long time (see e.g. Ladyzenskaja [1964]). The same holds for the even more difficult case of the Euler equation. Since the main difficulties of the three-dimensional case are absent in two dimensions, this gives no further hint for the problem at hand. At least some results where made for the three-dimensional case: For a finite interval $(0, T]$, $T \in \mathbb{R}$ depending on the initial conditions $\mathbf{u}_0$, existence and smoothness can be shown. The maximum time T for the solution to be finite is called the *blow-up time*. It is not known, whether the blow-up time for the Navier-Stokes or Euler equation for smooth initial conditions is always infinite or if there exists some smooth initial condition $\mathbf{u}_0$ with $T < \infty$ being finite. It is known though that for a finite blow-up time the velocity $\mathbf{u}(T)$ has to become unbounded,

$$|\mathbf{u}(t)|_\infty > C \qquad \forall\, C \in \mathbb{R}, \tag{6.1}$$

for a t near this time.

Even sooner, Leray [1934] proved the existence of *weak solutions* to the Navier-Stokes equation, which is defined as follows: For any smooth vector field $\theta(\mathbf{x}, t)$ and scalar field $\varphi(\mathbf{x}, t)$, both with compact support in space-time ($\mathbb{R}^3 \times (0, T]$), it holds that

$$\begin{aligned} \iint_{\mathbb{R}^3\times\mathbb{R}} \mathbf{u} \cdot \partial_t \theta \, \mathrm{d}\mathbf{x}\mathrm{d}t - \sum_{i,j} \iint_{\mathbb{R}^3\times\mathbb{R}} u_i u_j \partial_j \theta_i \, \mathrm{d}\mathbf{x}\mathrm{d}t = \\ \nu \iint_{\mathbb{R}^3\times\mathbb{R}} \mathbf{u} \cdot \Delta\theta \, \mathrm{d}\mathbf{x}\mathrm{d}t + \iint_{\mathbb{R}^3\times\mathbb{R}} \mathbf{f} \cdot \theta \, \mathrm{d}\mathbf{x}\mathrm{d}t - \iint_{\mathbb{R}^3\times\mathbb{R}} p(\nabla \cdot \theta) \, \mathrm{d}\mathbf{x}\mathrm{d}t \end{aligned} \tag{6.2a}$$

$$\iint_{\mathbb{R}^3\times\mathbb{R}} \mathbf{u} \cdot \nabla\varphi \, \mathrm{d}\mathbf{x}\mathrm{d}t = 0, \tag{6.2b}$$

where (6.2a) is the Navier-Stokes equation, scalar multiplied by θ and integrated over space-time and (6.2b) the same for the incompressibility condition. This is a weaker claim than for a classical solution of the equation: We just need $\mathbf{u}(\mathbf{x}, t) \in L^2$ instead of $\mathbf{u}(\mathbf{x}, t) \in C^2$. Of course, every classical solution also is a weak solution. A common practice for partial differential equations is to first construct a weak solution, then prove its smoothness. With this ansatz no success was achieved for both the Navier-Stokes equation and the Euler equation. Also the uniqueness of weak solutions is not known today for the Navier-Stokes equation and shown to be false for the Euler equation.

For Euler equation, some conditions have emerged, concerning the constraints of a finite time blow-up.

6.1.1 Criteria for a finite time blow-up

The first and most important result is the theorem by Beale et al. [1984], stating that a finite time blow-up may occur, if and only if the maximum of the vorticity blows up, too,

$$\int_0^T |\boldsymbol{\omega}(t)|_\infty \, \mathrm{d}t = \infty. \tag{6.3}$$

If the maximum vorticity remains bounded, there exists a global solution

$$\mathbf{u}(\mathbf{x}, t) \in C((0, \infty]; H^s) \cap C^1((0, \infty]; H^{s-1})$$

for $s \geq 3$. This conclusion is helpful in several ways. First it guarantees that a solution of the Euler equation cannot develop a singularity through one of the following processes alone:

- curvature singularities or kinks in vortex lines
- discontinuities in the vorticity, while $|\boldsymbol{\omega}|_\infty$ remains bounded ("vorticity shocks")
- a singular rate of strain matrix without a blow-up of the maximum of the vorticity.

If any of these events are observed in a simulation without a blow-up of vorticity, it has to be a numerical artifact.

Second this shows that one has to look at the maximum of the vorticity alone. A singularity in $|\boldsymbol{\omega}|_\infty$ and, thus, a finite time blow-up may occur, with e.g. $|\boldsymbol{\omega}|_2^2$ staying bounded for all times. The only quantity to be monitored is $|\boldsymbol{\omega}|_\infty$.

Ponce [1985] showed the same for the deformation tensor $T_{ij} = \partial_i u_j + \partial_j u_i$. A finite time breakdown of the smoothness may only occur, if and only if the maximum norm of the deformation tensor

$$\int_0^T |T_{ij}|_\infty \, \mathrm{d}t = \infty \tag{6.4}$$

grows out of bounds. If one assumes the growth of the vorticity as

$$|\boldsymbol{\omega}(t)|_\infty \propto \left(\frac{1}{T-t}\right)^\gamma, \tag{6.5}$$

the above statements ensure that $\gamma \geq 1$. Any observed blow-up with $\gamma < 1$, would be ruled out by (6.3) as a numerical artifact.

These results all center on global principles and maxima of certain quantities. More recently, a geometric view of the flow properties has gained attention.

Geometric arguments

Define the direction of the vorticity at a point in space-time as

$$\xi(\mathbf{x}, t) = \frac{\boldsymbol{\omega}(\mathbf{x}, t)}{|\boldsymbol{\omega}(\mathbf{x}, t)|}, \tag{6.6}$$

where the denominator describes the $\mathbb{R}^3$-norm of the vorticity. As Constantin et al. [1996] pointed out, as long as both the maximum norm of $\nabla\xi(\mathbf{x}, t)$ is smoothly directed, i.e. $|\nabla\xi(\mathbf{x}, t)|_2^2$ is integrable in time from 0 to T in an $O(1)$ region and the maximum norm of velocity is uniformly bounded, then no blow-up can occur up to time T.

Later, this result was even improved by Cordoba and Fefferman [2001]. For an arc on an integral curve of the vorticity $\boldsymbol{\omega}(\mathbf{x}, t)$, a so-called *vortex line*, the tubular neighborhood in $\mathbb{R}^3$ consisting of a union of vortex lines is called a *vortex tube*. Their theorem concerns the typical behavior of twisting and bending of these tubes that simultaneously grow due to *vortex stretching*. Vortex tubes that are in a sense "regular" cannot lead to a finite time blow-up at time T as long as the maximum velocity fulfills the mild assumption

$$\int_0^T |\mathbf{u}(\mathbf{x}, t)|_\infty \, \mathrm{d}t < \infty \tag{6.7}$$

in a region around this vortex tube.

Unfortunately, both statements above up to now have not been applied to a numerical simulation and turn out to be difficult to check. More recent results promise simpler

numerical examination, when Deng et al. [2004] stated theorems concerning vortex line segments, with further improvements in Deng et al. [2005]:

For a vortex line segment $[s_1, s_2]$ containing the point of maximum vorticity, as long as

$$\left| \int_{s_1}^{s_2} (\nabla \cdot \xi) \, \mathrm{d}s \right| \leq \mathrm{const}(T)$$

for all times $0 < t \leq T$, no point singularity is possible. If a blow-up of vorticity occurs at one point along the vortex line segment, it must blow up simultaneously on the entire line segment. This theorem may rule out some scenarios as improper for a finite time singularity.

Let further L_t be a family of vortex line segments with vorticity comparable to $|\boldsymbol{\omega}|_\infty$, $L(t)$ the arc length of L_t, $\xi = \frac{\boldsymbol{\omega}}{|\boldsymbol{\omega}|}$ as above its direction and κ the curvature of the vortex line. For $\mathbf{n}$ being a unit vector, define

$$\begin{aligned} U_\xi(t) &= \max_{\mathbf{x},\mathbf{y} \in L_t} |\mathbf{u} \cdot \xi(\mathbf{x}, t) - \mathbf{u} \cdot \xi(\mathbf{y}, t)|, \\ U_\mathbf{n} &= \max_{L_t} |\mathbf{u} \cdot \mathbf{n}| \quad \text{and} \\ M(t) &= \max_{L_t} (|\nabla \cdot \xi|_\infty, |\kappa|_\infty). \end{aligned}$$

Let $A < 1 - B$ for $A, B \in (0, 1)$ and let $C \in \mathbb{R}^+$ be a positive constant. If it holds that

(i) $U_\xi(t) + U_\mathbf{n}(t) M(t) L(t) \leq (T - t)^{-A}$,

(ii) $M(t) L(t) \leq C$ and

(iii) $L(t) \geq (T - t)^B$,

then no blow-up up to time T can occur. Simulations, like Kerr [1993], indicate a velocity blow-up of $(T - t)^{-1/2}$ and a length scaling of the vortex tube like $(T - t)^{1/2}$, which is just the critical case $A = B = \frac{1}{2}$ that is covered by the improved theorem by Deng et al. [2005].

6.2 Numerical simulations

The last section already indicated the mutual approach of mathematical and numerical results. In this section, I will first briefly present the progress of the last two decades of Euler simulations. Only selected publications are mentioned. A more complete overview of the numerical history was written by Kerr [2007]. Later in this chapter, results obtained by my own simulation are presented. Despite the fact that no definite conclusion could be drawn, whether the Kida-Pelz initial conditions lead to a finite time blow-up of vorticity, some statements could be deduced regarding the importance of resolution and the way of presentation.

6.2.1 History of Euler simulations and recent developments

The numerical hunt for singularities started with Morf et al. [1980] simulating the Taylor-Green vortex. They thought to have found a finite time singularity. Brachet et al. [1983] redid this simulation at higher order and concluded that the formation of vortex sheets suppressed any singularities.

With Pumir and Siggia [1990], the first AMR code to follow the evolution of vorticity with higher resolution was introduced. All following simulations observed higher amplitude for the maximum vorticity, but fitted against the growth of a finite time singularity, no definite result could be obtained (see Gibbon [2007] for a nice compilation of contradicting conclusions regarding the evidence for and against finite time Euler singularities).

The symmetric initial conditions introduced by Kida [1985], Boratav and Pelz [1994] and later Pelz [2001] helped to reach higher resolutions, and lead to simulations at effective resolutions up to 2048^3 mesh points in Grauer et al. [1997].

High accuracy can be achieved with pseudo-spectral methods. State-of-the-art simulations, as presented by Hou and Li [2006], reach resolutions up to $1536 \times 1024 \times 3072$. The method of choice for this thesis, nevertheless, is a finite difference formulation, as these allow for higher resolutions applying AMR. A comparison between pseudo-spectral and finite difference methods (see Grafke et al. [2007]) suggests that the lower order of finite difference methods can be compensated by resolving the critical regions a factor 1.3 higher.

The above overview also contains a warning: Results of numerical simulations are deceiving. Numerous claims have been stated in the past, confirming finite time singularities or disproving them. As will be pointed out in section 6.2.2, depending on the way of visualization a hasty judgement is quite seductive.

6.2.2 Results

The symmetric Kida-Pelz initial condition (section 4.4.2) is used as initial condition as scenario for a possible finite time blow-up. The simulation conducted here makes use of the vorticity formulation presented in section 4.2 to employ adaptive refinement. This is reasonable since the simulation of singular or near-singular growth requires high resolution at very restricted regions. As refinement criterion, the value of $|\nabla \mathbf{u}|$ is monitored. As soon as it exceeds a certain threshold, the associated block is flagged for refinement.

To simulate the Euler equation, the viscosity was set to zero. This is misleading, because the integration scheme exhibits numerical dissipation. As this cannot be prevented for finite difference schemes, no attempt was made at estimating the exact quantity. Comparisons to pseudo-spectral methods, which by nature are subject to less dissipation, shows that this has no measurable effect up to large times.

With this set of parameters, effective resolutions up to 4096^3 were reached. The total memory consumption was less than 80 GB, which is close to the maximum possible amount for our Linux cluster (due to memory usage fluctuations caused by the re-gridding process). Higher resolution could be achieved on BlueGene, even if the efficiency would be limited by the scaling behavior of the multigrid algorithm.

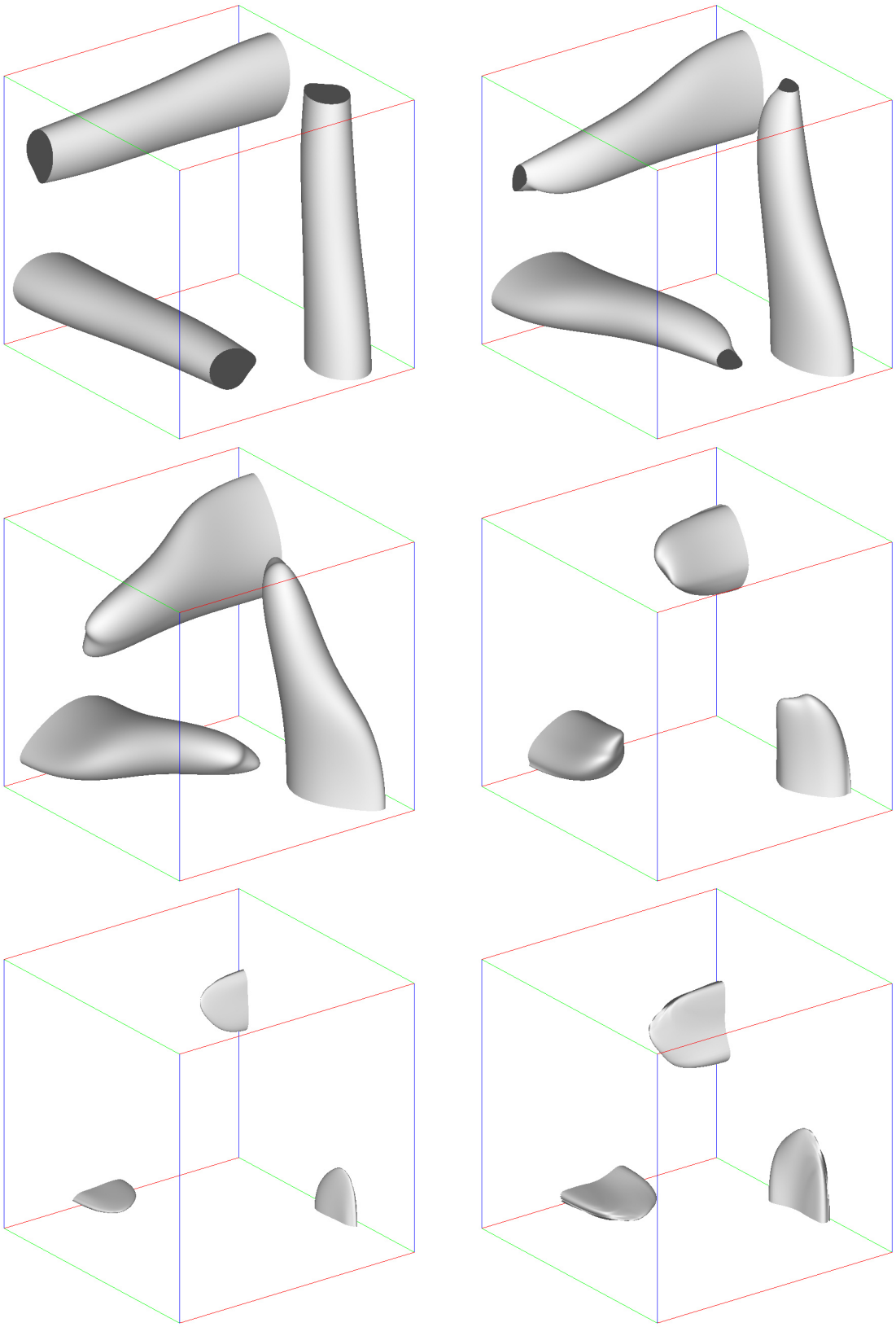

Figure 6.1: Time evolution of colliding vortex tubes at times $t = 0.1$, $t = 0.2$, $t = 0.3$, $t = 0.4$, $t = 0.45$, $t = 0.5$. Isosurfaces of $|\boldsymbol{\omega}|$ are pictured at $|\omega| = 18$ for the first three, $|\omega| = 30$ for the fourth and $|\omega| = 50$ for the last two frames, to display the form of the structures with maximum vorticity. In the final frames disk-like structures have evolved that further amplify each other.

Evolution of the flow

The initial vortex tubes approach each other and start to bend. Figure 6.1 shows details of this behavior, picturing isosurfaces of the rapidly growing vorticity $\mathbb{R}^3$-norm. In the final state, the structures of the peak vorticity resembles flat disks.

As expected, a rapid growth of the maximum of the vorticity is observed. Figure 6.2 (left) shows the time development of $|\boldsymbol{\omega}(t)|_\infty$. Using this graphical rendition it is difficult to distinguish between singular and just double-exponential growth. Figure 6.2 (right) pictures $1/|\boldsymbol{\omega}(t)|_\infty$, assuming $\gamma = 1$ in (6.5). A plot like this seems to suggest a finite time singularity at about $T = 0.55$.

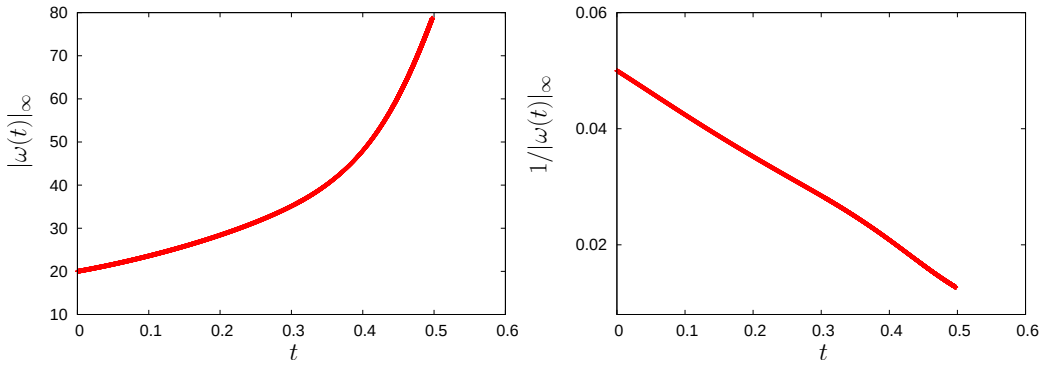

Figure 6.2: Left: Growth of the maximum of vorticity $|\boldsymbol{\omega}(t)|_\infty$ against time. A rapid accumulation of vorticity is observed. **Right:** Temporal evolution of $1/|\boldsymbol{\omega}(t)|_\infty$. The near-linear behavior suggests a finite time singularity at about $T = 0.55$. The data for both plots originates from a simulation using an effective resolution of 2048^3 grid points.

It appears that a more appropriate presentation is possible, when plotting $(T - t) \cdot |\boldsymbol{\omega}(t)|_\infty$. Assuming

$$|\boldsymbol{\omega}(t)|_\infty \propto \frac{1}{T - t} \tag{6.8}$$

as in (6.5) using $\gamma = 1$, the graph should converge to a horizontal line for a finite time singularity. In figure 6.3, this is shown for a blow-up time $T = 0.638$, chosen in a way that the final interval of the growth leads to an approximately horizontal graph. Different colors denoting the different levels of mesh refinement show significant discrepancies in the final growth. The high sensitivity on the numerical resolution indicates that conclusions drawn from this results must be handled with extreme caution. Even higher resolutions are the only possibility to rule out premature conclusions about singular behavior.

Conclusion

At this point, no definite answer about possible finite time singularities in the Kida-Pelz initial conditions can be given. While it is tempting to deduce a finite time blow-up from figure 6.2, the compensated plot reveals the critical dependence on the resolution.

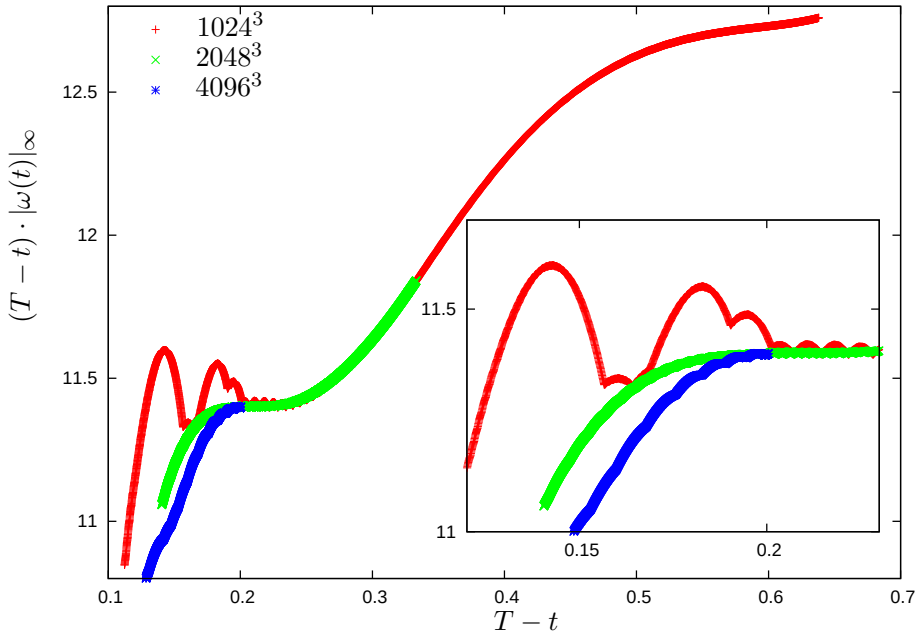

Figure 6.3: Improved presentation of the blow-up criterion for different numerical resolutions: Assuming (6.8), the scaling of the plotted quantity $(T-t)\cdot|\boldsymbol{\omega}(t)|_\infty$ should be horizontal. A critical dependence of the scaling behavior on the numerical resolution is observed.

Therefore, even higher resolutions of the simulation are indispensable and at reach when porting the problem efficiently to BlueGene.

Chapter 7

Summary

In this work, three hydrodynamical models were presented in direct comparison, the Navier-Stokes equation, the Burgers' equation and a new and intermediate model, the Euler-Burgers' equation. The ultimate ambition is to shed light on the Navier-Stokes/Euler equation regarding the problem of turbulence and the question of possible finite time singularities. Since these problems are unsolved despite enduring and intensive research, the introduction of the Euler-Burgers' equation can be considered as a new and different approach to the topic. While being entirely theoretical in nature and without any application in reality, the Euler-Burgers' equation was shown to be a prototype of a hydrodynamical model that circumvents the problems posed by the Navier-Stokes equation, without turning out to be overly simple in its structure and dynamical behavior.

All three models were compared analytically and numerically under the aspects of general characteristics, turbulence and possible singularities. The close connection of the structure of Navier-Stokes and Euler-Burgers' equation was pointed out for several aspects in chapter 2. Both are similar in terms of the procedure of energy dissipation, since the identical viscous term of both hydrodynamical models is solely responsible for the annihilation of kinetic energy. The nonlinearity was shown to leave the total energy untouched and rather change the scale the energy is distributed on, finally leading to the process that was introduced as the Richardson cascade. Furthermore, both equations feature a nonlinearity local in position space, accompanied by a nonlocal projection operation. While the projection for the Navier-Stokes equation is just a circumscription for the physical pressure and concurrently causes mathematical and numerical inconvenience due to its instantaneous nature, the same operation for Euler-Burgers' equation is mathematically treatable. It was shown in chapter 3 that global solutions of the Euler-Burgers equation exist for all times when sufficiently smooth external forcing and initial conditions. It was, furthermore, deduced that the solutions are smooth for all times and are unique. The Euler-Burgers' equation was, therefore, proved to be a full-fledged predictive hydrodynamical model that behaves well for all times.

For all further analysis and comparison of the model equations, numerical simulations were used. Two different implementations were added to the already existent framework *racoon II*. The first allows for accurate modeling of the maximum vorticity, maximiz-

ing the resolution by means of adaptive mesh refinement. While automatically ensuring solenoidality of the velocity field, the vorticity formulation, furthermore, provides reliable data for the most important finite time blow-up criterion, at the expense of execution speed. The second implementation focuses on the direct comparison of the three models. No adaptive refinement is employed but all model equations are implemented at once, allowing for an authentic comparison with improved execution speed. Both numerical formulations demand the solution of a Poisson-type equation that was obtained by implementing a Multigrid algorithm. It is capable of solving the Poisson equation parallel on an adaptive grid at arbitrary precision with adjustable error smoothing and interpolation methods. The simulations were mostly run on the local Linux Cluster, the obtained data was utilized to study general properties of the flows, to generate statistics and to analyze specific scenarios for possible finite time blow-ups.

No strict theory of turbulence is known today for the Navier-Stokes equation. During the last century, starting with the famous results of Kolmogorov, more and more refined phenomenological descriptions of turbulence based thereupon were developed. The most promising of these theories, regarding the successful description of numerical and experimental data, is the model of She and Lévêque. This model was modified to the generalized She-Lévêque model in chapter 5 to be applied to all three considered hydrodynamical models. For Burgers' equation, the energy spectrum and structure function were measured and the numerical data fits well on the theory. For the Euler-Burgers' equation, two-dimensional folded sheets were identified as the most dissipative structures. Inserting these into the generalized She-Lévêque model, predictions can be made for energy spectra and structure functions of turbulent Euler-Burgers' flows. The numerical data agrees very well with these predictions, showing that Euler-Burgers' turbulence is closely connected to Navier-Stokes turbulence.

Regarding the question of finite time singularities of the Euler equation, the mathematical criteria presented in chapter 6 hint to monitor the peak vorticity of the flow. Exactly this was carried out in an adaptive simulation to probe the Kida-Pelz initial conditions for a finite time singularity at a very high resolution, compared to simulations run so far. Though no definite conclusion could be drawn whether a finite time singularity is possible, the numerical data allows statements regarding the necessary grid resolution. Larger simulations will be able to finally settle the issue definitely.

7.1 Conclusion

The Euler-Burgers equation as a new hydrodynamical model was shown to combine several desired features at once. It was proved to be mathematically treatable when considering finite time singularities and the smoothness and uniqueness of solutions. On the other hand its turbulent behavior is still statistically very similar to Navier-Stokes turbulence, as it is treatable with the identical tools and shows comparable dynamical behavior of "true" turbulence. The new hydrodynamical model, therefore, proved to be based on an interesting equation enabling one to bridge the gap between phenomenology and strict theory.

Appendix A

Grid structure and notation

A numerical problem is defined on some spatial domain $\Omega \subset \mathbb{R}^d$ of dimension d with arbitrary form. The framework restricts us to $d \leq 3$ and rectangular domains only, but there is no need for anything fancier anyway. With $h \in \mathbb{R}^2$ being the *grid spacing vector* $h = (h_x, h_y)$ we define the *infinite grid*

$$G_h := \{(x_i, y_j) \in \mathbb{R}^2 | x = ih_x, y = jh_y; i, j \in \mathbb{Z}\}$$

and respectively for other dimensions d. With $\Omega_h := \Omega \cap G_h$ we denote our discrete computational domain or *grid*. For $h_x = h_y = h$ we call our grid a *square grid*.

Any **discrete function** $f : \Omega_h \mapsto \mathbb{R}$ can now easily be described by the simple notation

$$f_{i,j} := f_h(x_i, y_j) = f_h(ih_x, jh_y).$$

For **discrete operators** $L : \Omega_{h_1} \mapsto \Omega_{h_2}$ operating on a discrete function f_{h_1} on the grid Ω_{h_1} it is convenient to introduce the *stencil notation* by calling

$$[s_{i,j}] = \begin{bmatrix} & \vdots & \vdots & \vdots & \\ \cdots & s_{-1,1} & s_{0,1} & s_{1,1} & \cdots \\ \cdots & s_{-1,0} & s_{0,0} & s_{1,0} & \cdots \\ \cdots & s_{-1,-1} & s_{0,-1} & s_{1,-1} & \cdots \\ & \vdots & \vdots & \vdots & \end{bmatrix}$$

the *stencil* of L, if

$$Lf_{m,n} = \sum_{(i,j)} s_{i,j} f_{m+i,n+j}$$

for any $f : \Omega_{h_1} \mapsto \mathbb{R}$ and $m, n \in \mathbb{Z}$. All these notations are easily generalized to any dimension d (of course, stencils for $d > 2$ are hard to read).

Appendix B

Elliptic solver: Multigrid

Both schemes presented above need at some point the solution of the three-dimensional Poisson equation

$$\Delta\phi = \rho \tag{B.1}$$

on a domain Ω, with a potential ϕ and a source term ρ. This was accomplished with a *multigrid* method, which is regarded as the fastest numerical method for the solution of elliptic partial differential equations in general. Even if a wide range of problems can be solved efficiently with the multigrid approach, only the Poisson equation is of any relevance to the vorticity- and staggered grid formulation. Furthermore in the following explanations I will restrain myself to the two-dimensional Poisson equation (for simplicity and, not surprisingly, nicer pictures and readable stencils). The extension to three dimensions is straightforward. The implementation I wrote for *racoon II* is capable of solving the equation both in two and three dimensions. For a broader look on the topic see, for example, Trottenberg et al. [2001] or Briggs et al. [2000].

Despite the fact that just the Poisson equation will be treated here, it is convenient to introduce an abstract notation. Consider the system of linear equations

$$Lv = f, \tag{B.2}$$

with a linear operator L, the right-hand-side f and the exact and supposedly unique solution v. With u being an approximation of the solution, we define the difference to the exact solution, the (algebraic) *error*, by

$$e = v - u \tag{B.3}$$

and the *residual* or *defect* by

$$r = f - Lu. \tag{B.4}$$

From the uniqueness of the exact solution it follows directly that a vanishing error is equivalent to a residual equal to zero. Furthermore it is easy to see that the original problem $Lv = f$ is equivalent to the so called *defect equation* $Le = r$ (which only holds as

long as L is linear). As the numerical problem is discrete rather than continuous, the index h on each variable or Operator denotes the grid spacing, so the main equation becomes

$$L_h v_h = f_h \qquad \text{or} \qquad L_h e_h = r_h \tag{B.5}$$

on the discrete domain (*grid*) Ω_h. For details on the notation used in this section, see Appendix A.

The multigrid idea is based on combined error smoothing on multiple grids with different grid spacing. Thus, the main principles are *error smoothing* (relaxation) and *coarse grid correction*, which both will shortly be discussed in the following pages. Subsequently it is shown how both parts are interlinked to form a complete multigrid cycle. Finally, I add some remarks for the special treatment of multigrid on adaptively refined meshes and parallelization.

B.1 Smoothers

Consider a square grid Ω_h with grid spacing h. By $u^n_{i,j}$ we denote the current approximation u at $(x_i, y_j) \in \Omega_h$ at iteration step n. The discrete *finite difference* two-dimensional Poisson equation now looks like

$$\frac{1}{h^2}(u^n_{i-1,j} + u^n_{i+1,j} + u^n_{i,j-1} + u^n_{i,j+1} - 4u^n_{i,j}) = f_{i,j} \tag{B.6}$$

and can be solved for $u^n_{i,j}$ to be used iteratively:

$$u^{n+1}_{i,j} = \frac{1}{4}(u^n_{i-1,j} + u^n_{i+1,j} + u^n_{i,j-1} + u^n_{i,j+1} - h^2 f_{i,j}) \tag{B.7}$$

or, in stencil notation:

$$u^{n+1}_{i,j} = \frac{1}{4}\begin{bmatrix} & 1 & \\ 1 & 0 & 1 \\ & 1 & \end{bmatrix} u^n_{i,j} - \frac{h^2}{4} f_{i,j} \tag{B.8}$$

This type of iteration is called the *Jacobi iteration* (JAC). By damping the smoothing by a factor ω,

$$\begin{aligned} u^{n+1}_{i,j} &= \omega(\frac{1}{4}\begin{bmatrix} & 1 & \\ 1 & 0 & 1 \\ & 1 & \end{bmatrix} u^n_{i,j} - \frac{h^2}{4} f_{i,j}) + (1-\omega)u^n_{i,j} \\ &= \frac{\omega}{4}\begin{bmatrix} & 1 & \\ 1 & 4(\frac{1}{\omega} - 1) & 1 \\ & 1 & \end{bmatrix} + \frac{h^2\omega}{4} f_{i,j}, \end{aligned}$$

one obtains the ω-*Jacobi iteration* (ω-JAC). If applied several times, like shown in figure B.1, the error of the approximation becomes *smooth*. It takes quite a lot of steps for the error to become small, but after very few steps (just one or two) the high frequency noise of the error is already damped. It is helpful to keep this observation in mind for later.

Of course for the case $\omega = 1$ ω-JAC is equivalent to plain JAC-iteration. In practice, however, a choice of $\omega = 0.8$ yields the best results regarding convergence rates, slightly depending on the problem and initial conditions. A detailed mathematical analysis of the smoothing properties of ω-JAC can be found in Trottenberg et al. [2001][section 2.1.2].

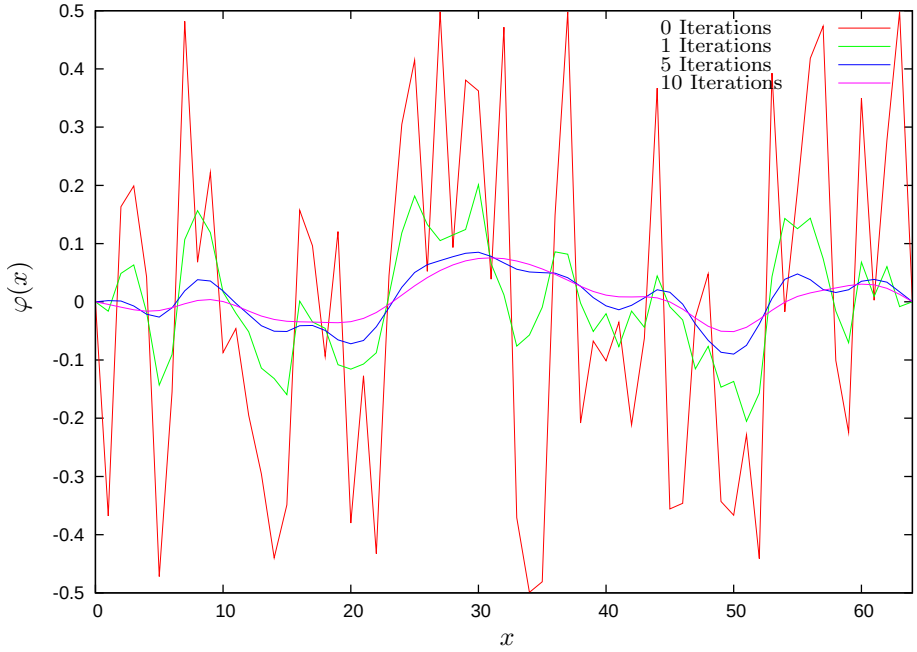

Figure B.1: Smoothing behavior for a random function with ω-JAC. High frequency modes are damped fast, large-scale fluctuations deplete very slow.

There are several smoothers, differing in properties like convergence rate, stability and scaling behavior. I will very briefly introduce three of them, all of which I have successfully implemented into the program.

Gauss-Seidel-type iterations

Easier to implement, superior in convergence rate (or more importantly *smoothing properties*) and memory usage, but more difficult to handle mathematically are the so called *Gauss-Seidel-type relaxation methods*. While in JAC-type iterations the whole field is updated at once, here the smoothing occurs in a determined ordering. Because of this, the already updated values are reused and there is no need to store the field twice. The most natural way to sweep through an array of values is lexicographic, which leads to the *Gauss-Seidel Lexicographic* smoother (GS-Lex):

$$u_{i,j}^{n+1} = \frac{1}{4}(u_{i-1,j}^{n+1} + u_{i+1,j}^{n} + u_{i,j-1}^{n+1} + u_{i,j+1}^{n} - h^2 f_{i,j}), \tag{B.9}$$

which is outlined in figure B.2 (left). GS-Lex in general shows higher convergence rates than any JAC-type iteration, but breaks the symmetry of the problem, as the lexicographic

sweep through the field is itself asymmetric.

The *Gauss-Seidel Red/Black* (GS-RB) smoother takes this idea one step further. The computational domain is divided into *odd* and *even* grid points, shown in figure B.2 (right) (which resemble the black and red fields of a checkerboard, hence the name) and each group of cells is updated as a whole. Thus all four grid points accessed in the black sweep have already been updated in the red sweep right before. In practice, GS-RB shows the highest convergence rate, but because of the double sweep, it also requires more computation time (in a massively parallel environment it requires twice as much communication, see section B.5).

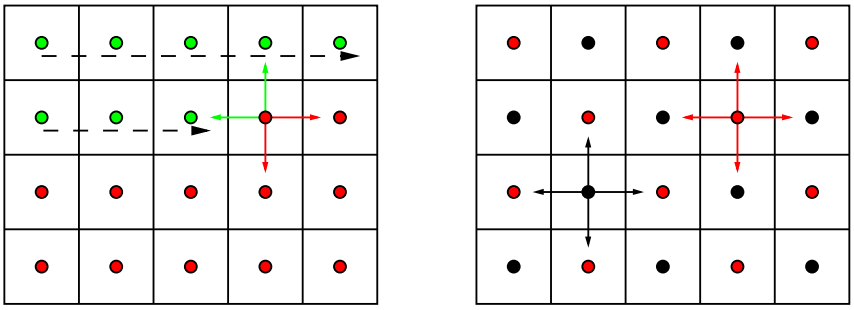

Figure B.2: Left: Lexicographic sweep through the fields with GS-Lex. Updated cells are colored green, old cells are red. **Right:** Grid distribution for Gauss-Seidel Red/Black. The black points are calculated after all red points have been updated.

Technically, equipped with just a smoother the Poisson equation could be solved in several hundred iteration steps. The problem obviously lies in the slow decay of large-scale errors. Because of this it seems plausible to take a closer look at the possible advantages in the use of different (coarser and finer) grids.

B.2 Multiple grids and intergrid communication

As already mentioned, one of the main ideas for multigrid is the use of several grids Ω_h with different grid spacing h. It is, therefore, inevitable to define a set of *transfer operators* $(I)_{h2}^{h1}$ to transmit information from the grid Ω_{h1} to the grid Ω_{h2}. While arbitrary grids could be chosen in theory, it is more practical both from a mathematical and numerical viewpoint to limit the choice to the so called *standard coarsening* Ω_{2h} with double mesh size in each direction as shown in figure B.3.

Most of the literature (e.g. Briggs et al. [2000] or Trottenberg et al. [2001]) mainly focus on vertex centered grids shown in figure B.3 (a), while *racoon II* utilizes cell centered grids (figure B.3 (b)) for both the potential and source term, even in the staggered grid formulation (section 4.3). This poses a problem, as the standard prolongation and restriction operators cannot be applied.

The choice of the transfer operators has radical influence on the overall performance of the multigrid method. As a detailed discussion of all these aspects exceeds the focus of

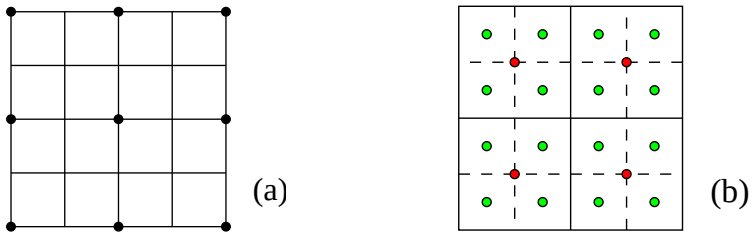

Figure B.3: The choice of the coarsened grid: **(a)** Standard coarsening for vertex centered grids. The coarse grid Ω_{2h} is denoted by black points, the fine grid Ω_h by intersections. **(b)** Standard coarsening for cell centered grid. Red points correspond to Ω_{2h}, green points to Ω_h.

this thesis, I will just summarize the implemented methods.

Prolongation

The *prolongation operator* for standard coarsening or *interpolation operator* $(I)_h^{2h} : \Omega_{2h} \mapsto \Omega_h$ maps coarse grid functions u_{2h} to fine grid functions u_h. I implemented two different prolongation operators, each with its own advantages and disadvantages.

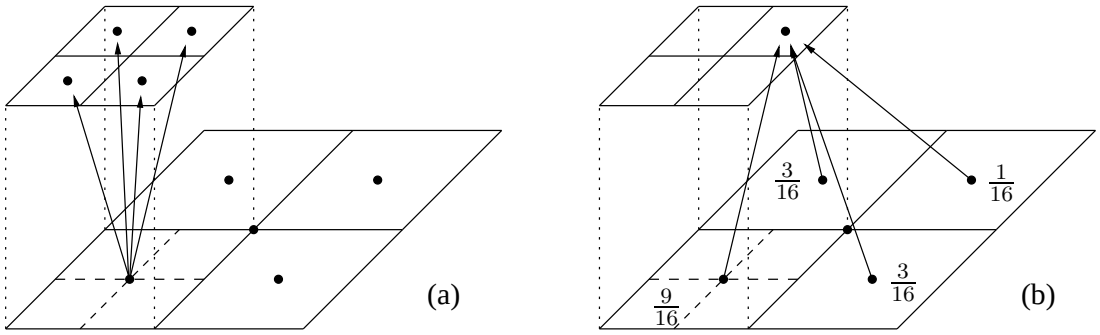

Figure B.4: Two different prolongation operators for cell-centered grids: **(a)** 1^{st} order copy of the coarse grid value. **(b)** Linear interpolation: All four surrounding coarse grid values have influence on the fine cell.

1^{st} order "interpolation": The easiest possible way to interpolate is just to copy the values from coarse to fine grid (see figure B.4 (a)). All four fine grid cells are set to the exact value of the corresponding coarse grid cell. This leads to the stencil:

$$(C)_h^{2h} = \begin{bmatrix} 0 & 0 \\ \boxed{1} & 0 \end{bmatrix}^{2h}_{h}$$

where the boxed field represents the $[s_{0,0}]$ position. While obviously this "interpolation" is of poor order (of 1^{st} order , it requires less computational time and, more importantly, no expensive boundary transfers in a parallel environment.

Linear interpolation: The second implemented stencil for prolongation reads

$$(L)_h^{2h} = \frac{1}{16} \begin{bmatrix} 3 & 1 \\ \boxed{9} & 3 \end{bmatrix} \begin{matrix} 2h \\ h \end{matrix} .$$

It weighs the four surrounding coarse grid cells with respect to their proximity to the fine grid point. While exact up to second order it also requires diagonal communication when parallelized, which has a noticeable impact on the wall-clock performance.

For multiple reasons it is wise to employ higher order prolongation, which require larger stencils and even more communication, but provide more precise results. Though implemented and tested, they are not discussed here.

Restriction

Restriction operators $(I)_{2h}^h$ map fine grid function u_h on Ω_h to the coarse grid Ω_{2h}. I will only commit myself to the straightforward choice of linear interpolation here. All surrounding fine grid values are weighed equally with $\frac{1}{4}$:

$$(F)_h^{2h} = \frac{1}{4} \begin{bmatrix} 1 & 1 \\ 1 & 1 \end{bmatrix} \begin{matrix} h \\ 2h \end{matrix} .$$

This is a second order interpolation. While higher orders are possible, they are neither implemented nor discussed here.

B.3 Complete multigrid cycle

Now, as the tools are thoroughly laid out, it is time to finally merge them all into the complete picture of the multigrid algorithm. The ultimate aim is to solve the discrete Poisson equation on some square grid Ω_h. The first step towards multigrid is the introduction of the *two grid cycle*:

- Choose an initial guess u_h on Ω_h. This choice is quite arbitrary and $u_h = 0$ works sufficiently well for Poisson-like problems. Preconditioning methods for finding better first approximations are not covered here.
- Relax ν_{pre} times on Ω_h (Pre-smoothing). Now, only large-scale components of the error should remain.
- Compute the residual $r_h = f_h - L_h u_h$ on Ω_h.
- Restrict the residual to Ω_{2h}: $r_{2h} = (I)_{2h}^h r_h$
- Solve the defect equation (B.5) on Ω_{2h}: $L_{2h} e_{2h} = r_{2h}$.
- Prolong the coarse grid error back to Ω_h: $e_h = (I)_h^{2h} e_{2h}$.
- Correct the approximation u_h on Ω_h with the error obtained above: $u_h^{n+1} = u_h^n + e_h$.

- Relax ν_{post} times on Ω_h (Post-smoothing).

All these points are well defined and outlined above, except one that may surprise: The original problem on Ω_h is reduced to a similar problem on Ω_{2h}. This may at first seem futile and inconveniently self-referring. Of course, a problem on Ω_{2h} is simpler in a sense that it consists of less unknowns and, if solved accurately, works very well for the fine grid, since the oscillatory components of the error are eliminated by the relaxation. The *complete multigrid cycle* is just one step ahead: As the coarse grid problem resembles the original problem, it can itself be solved by a two grid cycle. If this process is repeated on successively coarser grids Ω_{4h}, Ω_{8h}, etc., the whole problem reduces to a Poisson equation on a coarsest grid with ideally just one free grid point (or very few grid points, the amount depending on the grid structure and domain boundaries), where it can be solved exactly or by an adequate number of smoothing steps. This idea of recursively solving the original problem on successively coarser grids, interpolating the correction back to the fine grids and then smoothing the error is the whole gist of multigrid.

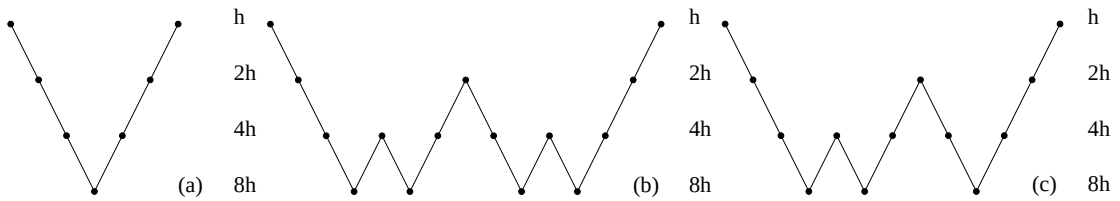

Figure B.5: Multigrid cycles: (a) V-Cycle, (b) W-Cycle, (c) F-Cycle

The multigrid cycle presented above, for reasons apparent in figure B.5, is called *V-Cycle*. More complicated paths through the multiple grids, like the *W-Cycle* or *F-Cycle*, are not only imaginable but also reasonable, because the accuracy of the coarse grid approximation has a large effect on the finer grids.

The final choice of all components (Smoother, Pre- and Post-smoothing, Relaxation, Prolongation, Cycle type) has to be balanced under aspects like convergence rate, stability, computational effort and communication overhead.

B.4 Full approximation scheme and adaptive multigrid

To be able to use the multigrid algorithm presented above for adaptively refined meshes, the *Full Approximation Scheme* (FAS) presented in section 5.3.4 of Trottenberg et al. [2001] was used. Originally designed for nonlinear equations its purpose in this context lies in the fact that the data held on all levels is the true potential ϕ instead of the defect r. Since for adaptively refined meshes the multigrid algorithm locally features coarser grids, the correct solution already is present for all different resolutions. With this technique implemented, *racoon II* is able to solve the Poisson equation on an adaptively refined grid.

B.5 Remarks on parallelization

Several aspects have to be taken in account when parallelizing the multigrid algorithm. Superior goal of parallel programming is to minimize communication while maximizing the amount of independent computation.

First, it should be noted that elliptic problems in general are more difficult to implement on distributed architectures, since information has to travel from every position to every other position instantaneously. In the multigrid algorithm, this travel of information is supported and accelerated by the coarsest grid that stretches over the whole domain with just very few grid points.

In a parallel environment, intergrid transfer may occur between different nodes. This implies huge amounts of data (entire block volumes) to be interchanged via the network. It is, therefore, advisable to minimize the blocksize in order to minimize the volume data. Also, the smaller the blocksize, the faster the coarsest grid can be solved. On the other hand, small but many blocks mean more memory usage, as ghost cells have to be stored for each block. For optimal performance on boundary exchanges, the ratio of surface to volume should be minimized. This discrepancy forms the main difficulty of the parallel multigrid algorithm and choosing the right blocksize.

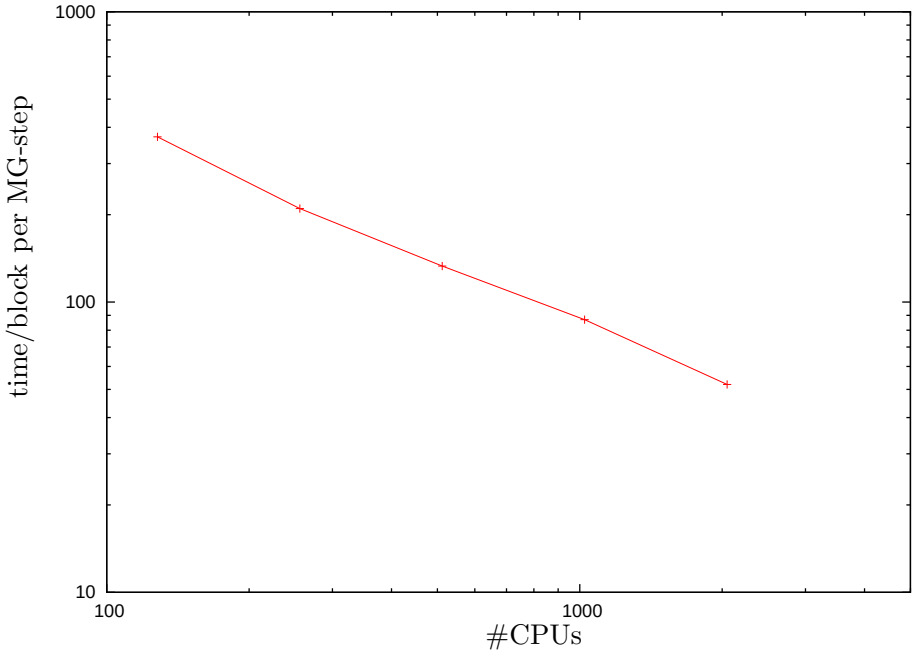

Figure B.6: Scaling behavior of *racoon II* with multigrid algorithm up to 4096 processors on BlueGene/P. The workload per processor is constant, the scaling is approximately linear.

Figure B.6 shows the scaling behavior of *racoon II* with multigrid algorithm, obtained with the IBM BlueGene/P of Forschungszentrum Jülich. Keeping the workload per node constant, up to 4096 processors were used (which resembles a resolution of 1024^3 grid

points). The scaling is approximately linear up to the maximum number of CPUs.

Appendix C

Generalization of the She-Lévêque model

In section 5.1.3 it is assumed that

$$\langle \varepsilon_l^p \rangle \propto l^{\tau_p}. \tag{C.1}$$

Furthermore, it was stated that

$$\varepsilon_l^{(\infty)} \propto l^{-k}, \tag{C.2}$$

where k is given via the time scaling of the considered hydrodynamical model and $\varepsilon_l^{(p)}$ is defined as

$$\varepsilon_l^{(p)} = \frac{\langle \varepsilon_l^{p+1} \rangle}{\langle \varepsilon_l^p \rangle}. \tag{C.3}$$

Starting from

$$\varepsilon_l^{(p+1)} \propto \left(\varepsilon_l^{(p)}\right)^{\beta} \left(\varepsilon_l^{(\infty)}\right)^{1-\beta} \tag{C.4}$$

one obtains, inserting (C.1), (C.2) and (C.3):

$$\langle \varepsilon_l^{p+2} \rangle \propto \langle \varepsilon_l^{p+1} \rangle \left(\frac{\langle \varepsilon_l^{p+1} \rangle}{\langle \varepsilon_l^p \rangle} \right)^{\beta} \left(l^{-k} \right)^{1-\beta} \tag{C.5}$$

$$\Leftrightarrow \qquad \tau_{p+2} = \tau_{p+1}(1+\beta) - \tau_p \beta - k(1-\beta). \tag{C.6}$$

$$\tag{C.7}$$

Inserting further the assumption that $\tau_p = -kp + C_0 + f(p)$ with $f(\infty) = 0$ one obtains

$$f(p+2) - (1+\beta) f(p+1) + \beta f(p) = 0 \tag{C.8}$$

with the only non-trivial solution $f(p) = \alpha \beta^p$. For τ_p, two boundary conditions must be satisfied: $\tau_0 = 0$ and $\tau_1 = 0$. This directly leads to $f(0) = \alpha = -C_0$ and $\beta = \frac{C_0 - k}{C_0}$ and finally

$$f(p) = C_0 \left(\frac{C_0 - k}{C_0} \right)^p. \tag{C.9}$$

Acknowledgements

In the following sentences I would like to thank all the people that have helped me throughout this thesis. In particular I express my gratitude to:

Prof. Rainer Grauer first, for the possibility to work at the *Institute for Theoretical Physics I*, for his support in theoretical and numerical questions and his advice. His optimism guided me through this work.

Dr. Jürgen Dreher for the numerous answers to any kind of questions and for all the guidance.

Jürgen Möllenhoff, who always ensured computing power and disk space.

the Institute TP I in general for the open doors, all the help and the constant flow of good ideas, and finally

my family for the unconditioned support.

List of Figures

List of Tables

Bibliography

S. Agmon. *Lectures on Elliptic Boundary Value Problems*. Prepared for publication by B. Frank Jones, Jr. with the assistance of George W. Batten, Jr. Van Nostrand Mathematical Studies, No. 2, D. Van Nostrand Co., Princeton, 1965.

Yukiya Aoyama and Jun Nakano. *RS/6000 SP: Practical MPI Programming*. IBM Corporation, International Technical Support Organization, Austin, Texas, 1999. URL `http://www.redbooks.ibm.com/redbooks/pdfs/sg245380.pdf`. IBM Redbook.

G. K. Bachelor. *An Introduction to Fluid Dynamics*. Cambridge University Press, London, 1974.

J. T. Beale, T. Kato, and A. Majda. Remarks on the breakdown of smooth solutions for the 3-D Euler equations. *Commun. Math. Phys.*, 94:61–66, 1984.

Christoph Beetz. Adaptive Simulationen kompressibler Turbulenz. Diplomarbeit, Ruhr Uni Bochum, September 2006.

R. Benzi, S. Ciliberto, R. Tripiccione, C. Baudet, F. Massaioli, and S. Succi. Extended self-similarity in turbulent flows. *Physical Review E*, 48(1):29–32, July 1993.

Olus N. Boratav and Richard B. Pelz. Direct numerical simulation of transition to turbulence from a high-symmetry initial condition. *Phys. Fluids*, 6(8):2757–2784, March 1994.

M. E. Brachet, D. I. Meiron, S. A. Orszag, B. G. Nickel, R. H. Morf, and U. Frisch. Small-scale structure of the taylor-green vortex. *J. Fluid Mech.*, 130:411–452, 1983.

William L. Briggs, Van Emden Henson, and Steve F. McCormick. *A Multigrid Tutorial, Second Edition*. Siam, 2000.

M. Briscolini, P. Santangelo, S. Succi, and R. Benzi. Extended self-similarity in the numerical simulation of three-dimensional homogeneous flows. *Physical Review E*, 50 (3):1745–1747, September 1994.

J. M. Burgers. *The Nonlinear Diffusion Equation. Asymptotic Solutions and Statistical Problems*. Reidel, Dordrecht, 1974.

P. Constantin, C. Fefferman, and A. Majda. Geometric constraints on potentially singular solutions for the 3D Euler equations. *Commun. Part. Diff. Eq.*, 21:559–571, 1996.

Peter Constantin and Ciprian Foias. *Navier-Stokes Equations*. The University of Chicago Press, Chicago and London, 1988.

Diego Cordoba and Charles Fefferman. On the collapse of tubes carried by 3D incompressible flows. *Commun. Math. Phys.*, 222:293–298, 2001.

Camillo De Lellis, Felix Otto, and Michael Westdickenberg. Minimal entropy conditions for burgers equation. *Quarterly of Applied Mathematics*, 62(4):687–700, 2004.

Jian Deng, Thomas Y. Hou, and Xinwei Yu. Geometric properties and nonblowup of 3D incompressible Euler flow. *Commun. Part. Diff. Eq.*, 30:225–243, 2004.

Jian Deng, Thomas Y. Hou, and Xinwei Yu. Improved geometric conditions for nonblowup of the 3D incompressible Euler equation. *Commun. Part. Diff. Eq.*, 31:293–306, 2005.

Charles R. Doering and J.D. Gibbon. *Applied Analysis of the Navier-Stokes Equations*. Cambridge Texts in applied mathematics, Cambridge, 1995.

Juergen Dreher and Rainer Grauer. Racoon: A parallel mesh-adaptive framework for hyperbolic conservation laws. *Parallel Computing*, pages 913–932, 2005.

Uriel Frisch. *Turbulence*. Cambridge University Press, Cambridge, 1995.

J. D. Gibbon. The three-dimensional Euler equations: Where do we stand? *Physica D: Nonlinear Phenomena*, 237:1894–1904, November 2007.

Toshiyuki Gotoh and Robert H. Kraichnan. Numerical calculation of time-dependent viscous incompressible flow of fluid with free surface. *Phys. Fluids A*, 5(2):445–457, 1992.

T. Grafke, H. Homann, J. Dreher, and R. Grauer. Numercial simulations of possible finite time singularities in the incompressible Euler equations: comparison of numerical methods. *Physica D: Nonlinear Phenomena*, 237:1932–1936, November 2007.

Rainer Grauer, Christiane Marliani, and Kai Germaschewski. Adaptive mesh refinement for singular solutions of the incompressible Euler equations. *Physical Review Letters*, 80 (19):4177–4180, May 1997.

Francis H. Harlow and J. Eddie Welch. Numerical calculation of time-dependent viscous incompressible flow of fluid with free surface. *The Physics of Fluids*, 8:2182–2189, 1965.

Holger Homann. *Lagrange Statistics of turbulent Flows in Fluids and Plasmas*. PhD thesis, Ruhr Uni Bochum, 2006.

Thomas Y. Hou and Ruo Li. Dynamic depletion of vortex stretching and non-blowup of the 3-D incompressible Euler equations. *J. Nonlinear Sci.*, 16:639–664, April 2006.

Robert M. Kerr. Evidence for a singularity of the three-dimensional, incompressible Euler equations. *Phys. Fluids A*, 5(7):1725–1746, July 1993.

Robert M. Kerr. Computational Euler history. *Journal of Computational Physics*, 209: 582–598, 2007.

S. Kida. Three-dimensional periodic flows with high-symmetry. *Journal of the Physical Society of Japan*, 54:2132–2136, June 1985.

A. N. Kolmogorov. Local structure of turbulence in an incompressible fluid at very high reynolds numbers. *Dokl. Akad. Nauk SSSR*, 30:299–303, 1941a.

A. N. Kolmogorov. Energy dissipation in locally isotropic turbulence. *Dokl. Akad. Nauk SSSR*, 32:19–21, 1941b.

A. N. Kolmogorov. A refinement of previous hypotheses concerning the local structure of turbulence in a viscous incompressible fluid at high reynolds numbers. *J. Fluid Mech.*, 13:82–85, 1962.

Alexander Kurganov and Doron Levy. A third-order semidiscrete central scheme for conservation laws and convection-diffusion equation. *Jour. Sci. Comp.*, 22(4):1461–1488, 2000.

O. Ladyzenskaja. *The mathematical theory of viscous incompressible flows*, volume 2. Gordon and Breach, New York, 1964.

J. Leray. Essai sur le mouvement d'un liquide visquex emplissant l'espace. *Acta Math.*, 63:193–248, 1934.

Rudolf H. Morf, Steven A. Orszag, and Uriel Frisch. Spontaneous singularity in three-dimensional, inviscid, incompressible flow. *Physical Review Letters*, 44(9):572–575, March 1980.

L. Nirenberg. On elliptic partial differential equations. *Annali della Scuola Norm. Sup.*, 13:115–162, 1959.

OpenMPI. Open MPI: Open source high performance computing. Project webpage, 2006. URL `http://www.open-mpi.org/`.

S. Orszag and C. M. Tang. Small-scale structure of two-dimensional magnetohydrodynamic turbulence. *J. Fluid Mech.*, 90:129, 1979.

Richard B. Pelz. Symmetry and the hydrodynamic blow-up problem. *J. Fluid Mech.*, 444: 299–320, January 2001.

Gustavo Ponce. Remarks on a paper by J. T. Beale, T. Kato and A. Majda. *Commun. Math. Phys.*, 98:349–353, 1985.

Alain Pumir and Eric Siggia. Collapsing solutions to the 3-D Euler equations. *Phys. Fluids A*, 2(2):220–241, February 1990.

L. F. Richardson. *Weather Prediction by Numerical Process*. Cambridge University Press, 1922.

Christian Schwarz. Lagrange-Statistik in kompressibler Turbulenz. Diplomarbeit, Ruhr Uni Bochum, March 2007.

Zhen-Su She and Emmanuel Lévêque. Universal scaling laws in fully developed turbulence. *Physical Review Letters*, 72(3):336–339, January 1994.

C. Shu and S. Osher. Efficient implementation of essentially non-oscillatory shock-capturing schemes. *Journal of Computational Physics*, 77:439–471, 1988.

Roger Temam. *Navier-Stokes Equations*, volume 2. Elseview Science Publishing Company, Amsterdam, 1984.

Roger Temam. *Infinite-Dimensional Dynamical Systems in Mechanics and Physics*. Springer Verlag, New York, 1988.

Ulrich Trottenberg, Corelis Oosterlee, and Anton Schueller. *Multigrid*. Academic Press, London, 2001.